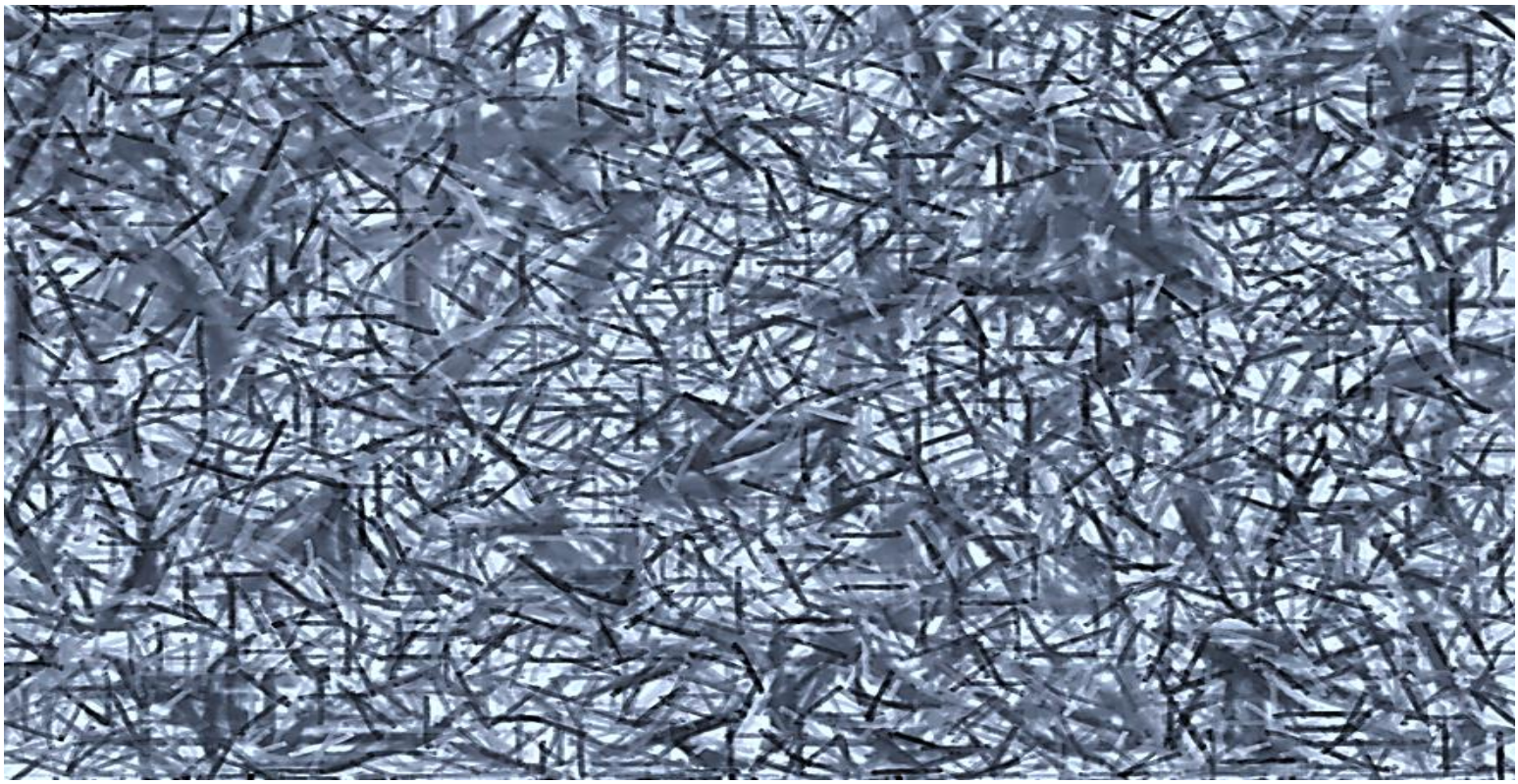

November 2023

EFFECT OF PRE-STRAIN ON HYDROGEN EMBRITTLEMENT OF HIGH STRENGTH STEELS

Master Thesis:

Material Science and Engineering

Elena Trigo Gallego (5631440)

Supervisors:

Dr. Vera Popovich

Ir. Tim Boot

TU Delft

ABSTRACT

To mitigate global warming, society must reduce greenhouse gas emissions. The transportation sector is one of the largest energy consumers and greenhouse gas emitters. One way to mitigate the emissions of this sector is to reduce the weight of vehicles using Advanced High Strength Steels (AHSS), particularly dual phase steels (DP). However, these steels are subject to hydrogen embrittlement which hinders their full potential and application inside the automotive industry.

The effect of pre-strain level and in-situ pre-straining on hydrogen embrittlement was investigated for DP1000. Therefore, in-situ tensile test was performed at 0.5% and 2% plastic pre-strain to study hydrogen embrittlement by measuring strain at fracture. This test was done under ex-situ and in-situ pre-strain conditions. In addition, sample charging time was varied from 15 to 60 minutes for 2 % plastic pre-strain. Thermal Desorption spectroscopy was performed to measure hydrogen uptake. Fracture surface was studied by scanning electron microscopy. Results showed that pre-strain plays an important role in hydrogen embrittlement, namely 0.5 % and 2 % plastic pre-strain reduced the final strain to fracture by almost 50 % for both in-situ and ex-situ charging cases. However, no significant increase in hydrogen embrittlement occurs for the increment from 0.5% to 2% pre-straining, except for the 0.1 wppm increase in hydrogen content. Differences in results for in-situ and ex-situ testing were only observed for 2% pre-strain at 60 minutes charging. Increase in charging time resulted in increased hydrogen uptake, however, no severe effects were observed in hydrogen embrittlement. For future work it is recommended to study different extra pre-strain levels, further increase the charging time and investigate the effect of various DP1000 microstructures, such as ferrite, martensite and retained austenite ratios.

ACKNOWLEDGEMENTS

I have to thank, first of all, my supervisor, Dr. Vera Popovich for her availability throughout this time spent searching for answers in my master's thesis. I've always could count on her knowledge, dedication and clarity of ideas.

Likewise, I must thank Ir. Tim Boot, who has assisted in the achievement of objectives and in the realization of different ideas for the investigation development. I am grateful for his commitment and support during this thesis.

To the people of the mechanical laboratory, in particular to Dr. Ir. Ton Riemslag, who with his experience have helped me solve the practical problems that arose seeking together solutions for the progress of my research. I would also like to thank Elise Reinton, Sean Scott, Raymond Dekker and Aswin Suresh who helped me and contributed as well as to create a great working environment.

To my colleagues and friends Aditya, Rita, Paul, Laura, Alice, Marloes for having shared with me those hours of study, effort, and memories.

Contents

LIST OF FIGURES

LIST OF TABLES

1. INTRODUCTION

Climate change is an urgent and demanding issue of nowadays society. Global warming is accelerating due to all the emissions of damaging greenhouse gases such as NOx, SO_2, CO_2, CO, etc. liberated into the atmosphere [1]. In 2013 a record was broken, surpassing safety levels of 350 parts per million of CO_2. In 2019 levels reached 415.39 parts per million. CO_2 emission have been rising since 1940 as can be seen in Figure 1 with the exception of 2020 due to the lockdown, and other historical events [1] [2]. Agreements have been proposed to meet zero emission by 2050.

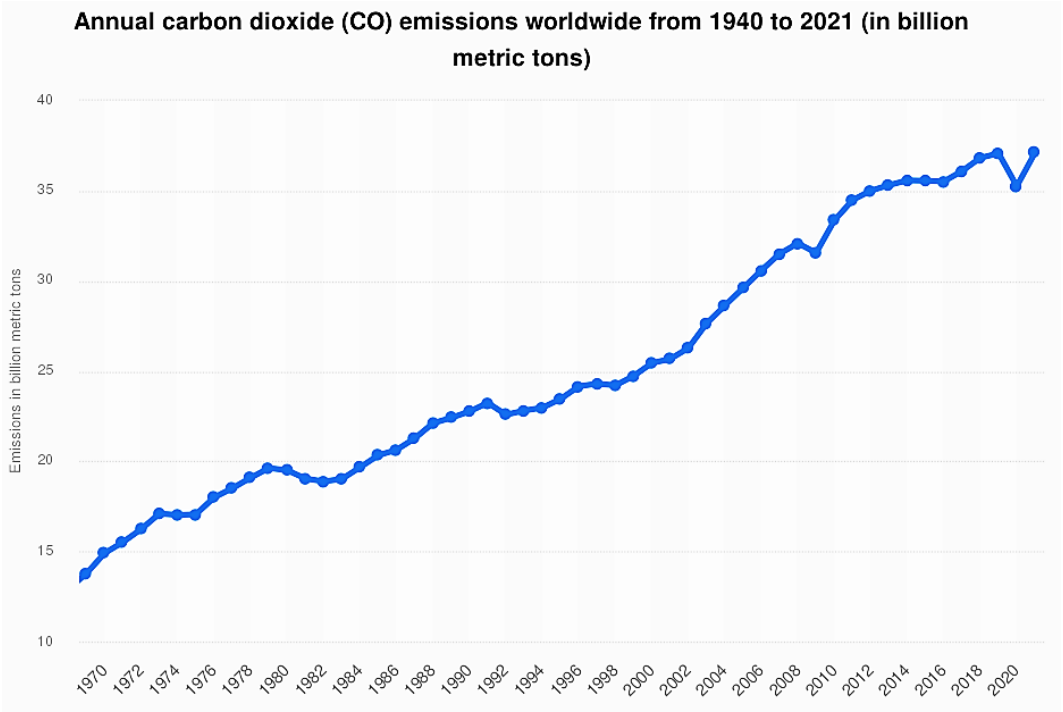

Figure 1 Annual carbon dioxide emissions worldwide from 1940 to 2021 [1].

Inarguably the transportation sector, and in particular automotive sector, plays a key role in emissions released and energy consumption. The transport sector is direct responsible for 30 % of world's total energy spending, that can be distributed in: 16 % raw materials production, 70% dedicated to use, 9% vehicles manufacturing and 1% to recycling [3] . Emissions caused by the transport sector should be reduced by a 60%, and at least a 34% to limit the increase of global temperature to 2ºC by 2050 to conquer goals proposed [4].

One of the possible solutions that is resonating within the industry is the weight reduction in automobiles. Many investigations support this idea as a good solution to decrease greenhouse emissions, energy and material consumption, and to improve efficiency. Cabrera Serrenho et.al stated that weight reduction could diminish a great part of emissions when compared with electric solutions since they will require a massive decarbonization in the electricity grid [4]. In contrast, reduction in the weight will have an immediate impact in the decarbonization.

Furthermore, many greenhouse emission goals don't take into account the decrease in material and electricity production that can be achieved by diminishing cars' weight. Data suggest that approximately a 75% of the fuel used by automobiles is directly correlated with their weight [2]. Due to a reduction in tractive forces acting on the vehicle, reducing its weight by 10% can be translated into a 6% or 8% fuel consumption reduction. Regarding CO_2 emissions 9 g/km can be reduced per 100 kg loss in a vehicle. However, this might increase the risk by 3-4.5% in case of an accident [5]. This is why a balance between safety and reduction of weight must be achieved [6]. This can be accomplished with material substitution. Advanced High Strength Steel (AHSS) portray themselves as a great candidate. Other lightweight materials such as aluminum or magnesium alloys present higher price and lower volume production, poor machinability, and incompatibility with traditional well known manufacturing technologies.

AHSS present a better combination of ductility and strength than common carbon steels, allowing a reduction of thickness without compromising the safety since required properties are maintained [3]. In addition, a 5.7%, equivalent to 8 Kg, decrease in greenhouse gas emissions over the life cycle of the automobile is achievable per 1 kg AHSS substitution in a five-passenger family car [5]. For 2040 it is expected that energy consumption for the transportation sector to diminish 25.5 quadrillion Btu if weight is reduced. It is also estimated that for 2020 up to 28%-36% of the vehicle will be replaced by AHSS steels. Nevertheless, advance high strength steels suffer from the effects of a mechanism known as hydrogen embrittlement. This constitutes the main disadvantage for their application. Comprehending and tackling this problem is fundamental for assuring Advance High Strength Steels' implementation and benefit from their technical and environmental advantages.

The motivation of this literature study is to establish the necessary conceptual pillars for the understanding of hydrogen embrittlement and the correct development and analysis of the thesis project. This literature review aims to find and explore research gaps and consolidate an objective to develop the later investigation. In the present work, chapter 2 deals with hydrogen embrittlement processes from hydrogen uptake and charging, hydrogen diffusion and trapping to different hydrogen embrittlement mechanisms. Chapter 3 discusses Advance high strength steels in general and dual phase in a more specific manner since the material of study will be indeed of this type. Chapter 4 introduces possible methods to investigate hydrogen susceptibility from the point of view of hydrogen concentration measurement techniques or mechanical testing. Chapter 5 describes some of the main external and internal factors that influence hydrogen embrittlement. In both, Chapter 4 and chapter 5 a selection of the techniques and factors was made based on their relevance with the later experimental part since both topics are very broad. From all these chapters, conclusions are derived and exposed in Chapter 6 as well as the research objectives in Chapter 7. In addition, in this last chapter some future investigation topics are recommended since diverse research gaps were found as well in the literature.

2. LITERATURE REVIEW

2.1 ADVANCED HIGH STRENGTH STEELS: dual phase steels

As it was mentioned before, Advanced High Strength Steels (AHSS) are high performance steels that possess a good combination of ductility and strength that are usually characterized by having in general a multiphase microstructure [3]. It is indeed its high specific strength that characterized them, that allows for employing less material to fulfill the same requirements in the automotive sector. In addition, they permit a high amount of energy absorption being used in crash boxes A and B pillars, roof rails and sill reinforcements and front-end structures inside the cars (Figure 2).

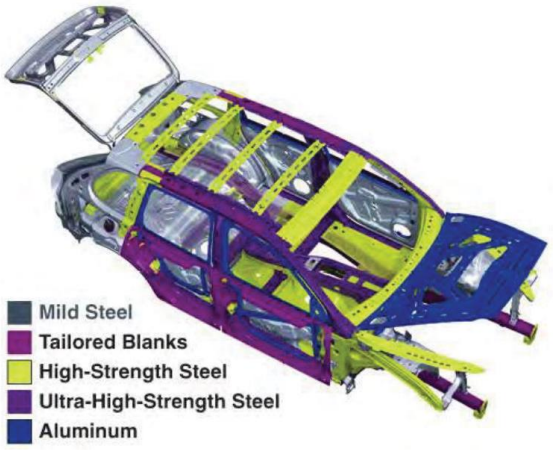

Figure 2 The different materials used in the different parts of the car [3].

AHSS have evolved since they were first developed [3]. Automobile industry introduced them for the first time in 1980's. This has led to the formation of different generations of products in which AHSS can be classified. The precursor these steels were High strength steels (HSS) that reached a strength from 210 to 550 MPa while AHSS reach a strength from 500-1200 MPa [5] . The main difference between both lies in the multiphase microstructure of AHSS.

The first generation of AHSS is based on the combination of ferrite with other types of microstructures [7]. A reduction in ductility can be appreciated in exchange of gaining higher strength [5] [7] [8]. This property makes them suitable for load bearing applications, maintaining an accessible price. However, low formability reduces the possibility of intricate geometries. Dual-Phase (DP), Complex Phase (CP), Transformation Induced plasticity (TRIP) and Martensitic (MS) steels are included in this category. DP steels are compound of a ferritic matrix with martensitic island embedded in it where CP steels present a high-volume fraction of bainite and martensite in a fine ferrite matrix [7]. DP steels were the first AHSS to be used in the automobile sector in the 80'. CP was only introduced in the late 90's [3] (Figure 3). TRIP steels are defined by martensitic transformation from retained austenite when deformed, adding itself to a microstructure formed by ferrite, bainite and retained austenite phases [5] [7] [8]. They were

used in the automobile sector for the first time 1990's [3]. Martensitic steels are the only AHSS of the first generation that consist of a single phase. Martensite is displayed in the shape of needles [7]. In Figure 4, a scheme of the microstructure of the different types of steel can be seen.

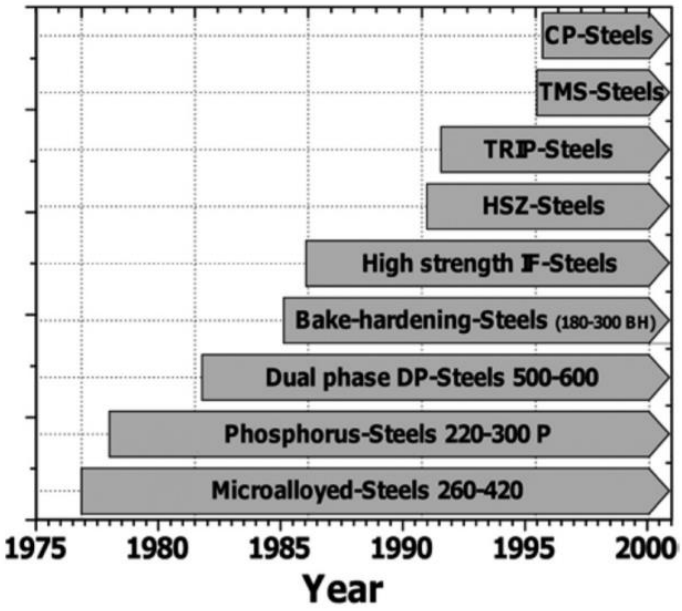

Figure 3 Scheme of when some first generation AHSS were introduced in the automotive sector [3].

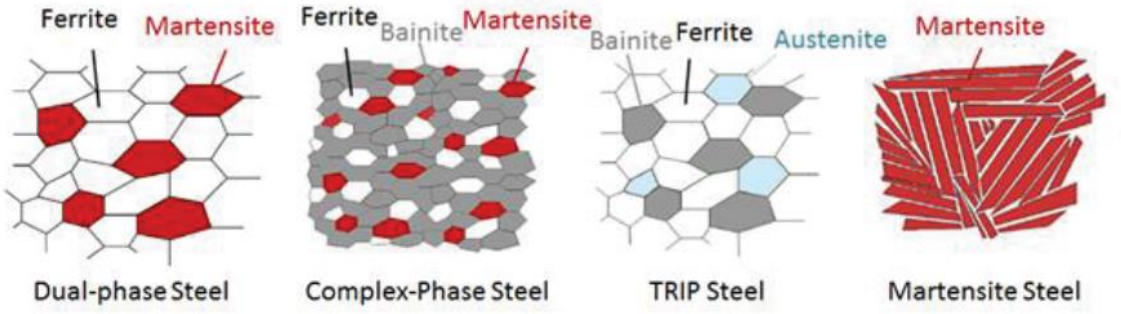

Figure 4 scheme of the microstructure of the different types of 1st generation AHSS [7].

The second generation of Advanced High Strength Steels are austenite-based steels that use high Manganese (Mn) content to stabilize this phase (Gamma stabilizer element) [13]. Strength is reached through deformation. These steels present higher formability, drawability and ductility than the steels of the first generation, however, due to their high content in alloy elements such as Nickel and Chromium they are costly [5]. Lightweight steel with induced plasticity (L-IP) steels and Twinning Induced Plasticity (TWIP) steels are part of this category [5]. The third generation is a combination of the benefits of the first and second generation. It exhibits a better combination of elongation and strength than the first generation and lower

cost compared with the second generation of AHSS [5]. It only presents a medium content approximately volume fraction of a 10% of Mn, Si and Cr [7]. They are still under research [5]. An Ashby diagram is displayed in Figure 5.

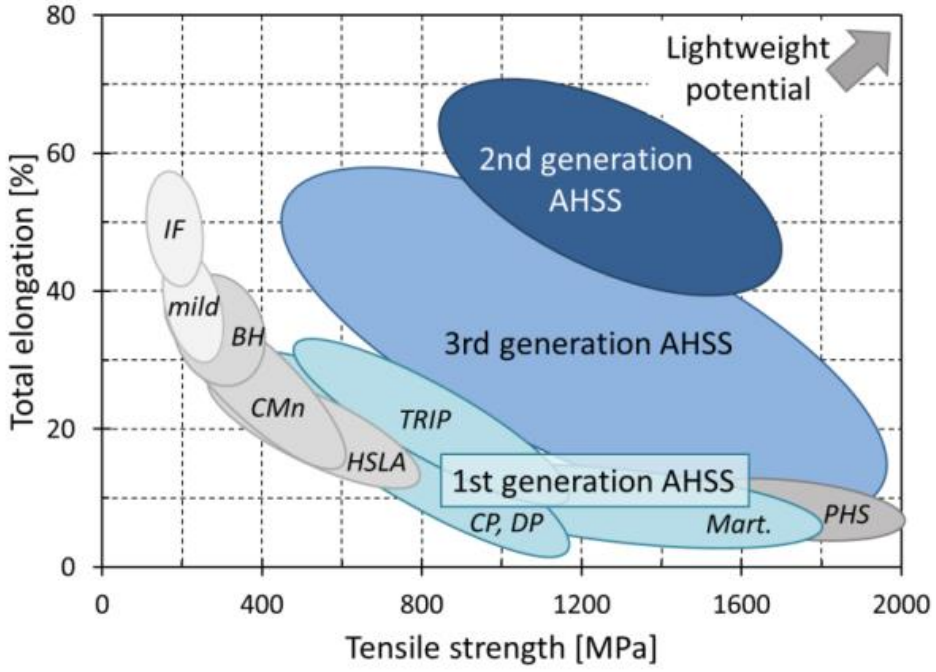

Figure 5 Classification of AHSS generations depending on their elongation and tensile strength [7].

In this study first generation of steels, Dual Phase steels, are chosen to study hydrogen embrittlement since they are actively used in the automotive sector and hydrogen behavior hasn't been fully explored [5] [9]. Dual phases are characterized as well as the rest of AHSS with a good compromise between ductility and strength. The ferrite phase is responsible of the ductility, allowing the material to absorb strain around the martensitic islands while the strength highly depends on the martensite content present in the microstructure. However, a critical value in which tensile strength increases with martensite percentage exists between 50-63% [5]. Also, the martensite island distribution can become non homogeneous when its content surpasses the 50% volume fraction. DP steels are mainly composed by Iron, Carbon, Silicon and Manganese. Carbon ranging between 0.06-0.15 wt% (weight percentage) and Manganese between 1.2 and 2.5 wt%. Silicon is used to promote austenite transformation into ferrite. Chromium, Vanadium, Niobium and Molybdenum are used as gamma stabilizer elements to stabilize austenite. In addition, Chromium and Molybdenum are used to delay the bainite and pearlite apparition, not surpassing 0.4 wt%. Vanadium and Niobium can be used as grain refiners and precipitation strengtheners not exceeding 0.06 wt% and 0.04 wt %respectively. Niobium can tune the martensitic formation temperature.

For a given specific composition, the resulting microstructure (Figure 6), which the mechanical properties depend on, is closely related to processing parameters such as strain rate, deformation method, temperature and cooling process [5]. In the case of dual phase steels, the desired microstructure is produced through a controlled ferrite phase transformation from

austenite before a rapid cooling to transform the remaining austenite into martensite. This microstructure leads to macroscopic properties such as continuous yielding. This phenomenon occurs when there are no interstitial atoms during deformation allowing the dislocations to be mobile during deformation.

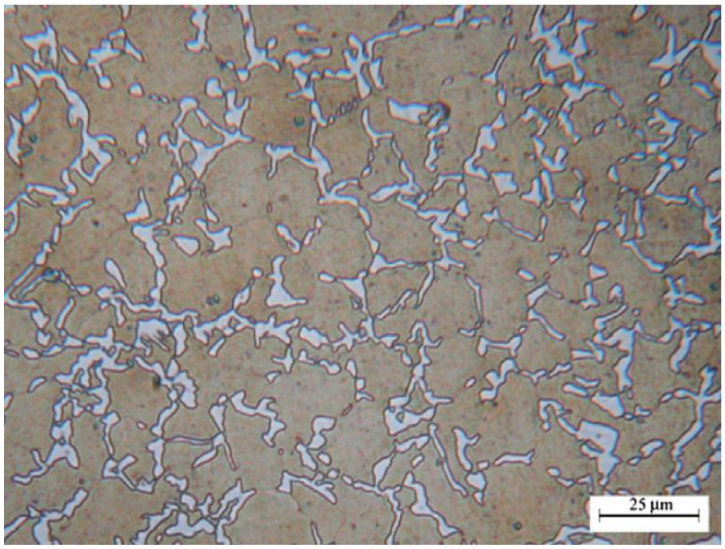

Figure 6 Dual phase microstructure by Optical microscope. Martensite is represented in white and ferrite in ochre [5].

2.2 HYDROGEN EMBRITTLEMENT

Hydrogen embrittlement is a "*phenomenon in which a metal is weakened by the incorporation of hydrogen in or below its surface*" [10]. This phenomenon was first noticed in 1875 by Johnson when he observed the change in properties during iron immersion in sulphuric and hydrochloric acids.

It is not only a problem in the automobile sector, but it also affects the chemical, gas processing, aerospace, power or fuel sectors, where it can produce catastrophic unpredictable failure [11] [12]. Therefore, different products such as hydrogen storage tanks, steel fasteners and weldments can be damaged. Hydrogen embrittlement compromises safety and reduces toughness and ductility.

Hydrogen can be incorporated into steel during manufacturing processes such as galvanic coupling, electrical processes, welding, and body-in-white-painting [11] [12]. External conditions, such as rich hydrogen environment, are also a source of absorption of this element [11] [13].

In conclusion, hydrogen embrittlement is a root issue for the applicability of AHHS for the automotive sector for the reduction of weight in vehicles since the susceptibility of the steels can be of less than 1ppm [14]. Therefore, the study of the interaction of hydrogen with Advance High Strength Steels, to prevent, predict and avoid failure is vital.

2.2.1 Hydrogen uptake

Hydrogen can be incorporated into the material in two steps: adsorption and absorption. Adsorption can be denominated as the process in which particles are attached to the metal to decrease the free energy of the surface [13]. Absorption process is the partial incorporation of the previously adsorbed hydrogen into the metal lattice. Hydrogen charging can be done also on purpose as a research technique. Hydrogen uptake can occur from hydrogen gas or from an electrolytic solution. The electrolytic solution hydrogen uptake can be divided into hydrogen charging by corrosion or cathodic hydrogen charging. In all scenarios, hydrogen needs to be in its atomic form to be absorbed [15].

A**) First scenario: Hydrogen absorbed from a gas phase**

Hydrogen can be chemically adsorbed or physically adsorbed [13]. Physisorption is based on Van der-Waals forces which presents a weaker interaction when compared with strong chemical bonds. At room temperature physical adsorption is more favorable since this mechanism has a low adsorption energy. On the contrary, at high temperature, chemical adsorption which present higher adsorption energy, prevails. A common process first step is to present physical adsorption followed by chemical adsorption, in which the hydrogen molecule dissociates at surface defects that are energetically more favorable [15]. Onwards, the atomic hydrogen can be absorbed.

Obtaining atomic hydrogen can be done at high pressure or high temperature to enhance its dissociation [15]. This is referred to as pressurized hydrogen charging. However, absorption is also possible at low partial pressures and temperatures after hydrogen chemical adsorption.

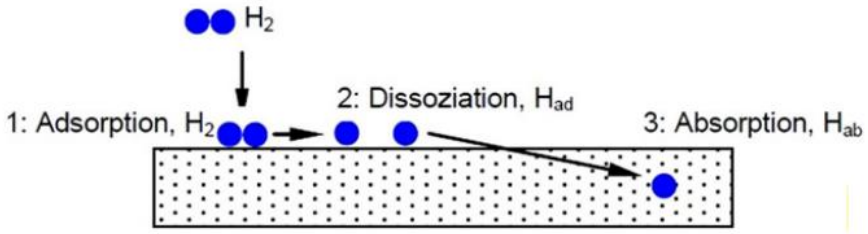

Figure 7 Intermediate steps of gas hydrogen adsorption and absorption [15]

B) Second Scenario: Hydrogen entry from aqueous environments

B1) Electrolytic hydrogen charging

This type of hydrogen uptake is based on corrosion reactions. Due to the low pH of electrolytic charging, hydrogen is forced to be reduced [13] [15]. Adsorption is produced by the conversion of hydrogen molecules to protons that recombine into H and interact with the metal [8]. The adsorption reaction, Volmer reaction, competes with the Heyrovsky and Tafel desorption reactions in which hydrogen is liberated again in the gas form as a diatomic molecule [9]. Nevertheless, according to Tafel, it is dependent on the conditions whether for his reaction's

hydrogen atoms are adsorbed or desorbed [11]. Following absorption depends on the formation of a top layer and the corrosion attack, since the highest amount of hydrogen produced (due to higher amount of material being attacked) correlates with its probability of being absorbed [15].

Volmer $$H^+ + e^- \leftrightarrow H_{ad} \quad (1)$$

Tafel $$H_{ad} \leftrightarrow H_{ab} \quad (2)$$
$$2H_{ad} \leftrightarrow (H_2)_{ad}$$

Heyrovsky $$H_{ad} + H^+ + e^- \leftrightarrow (H_2)_{ad} \quad (3)$$

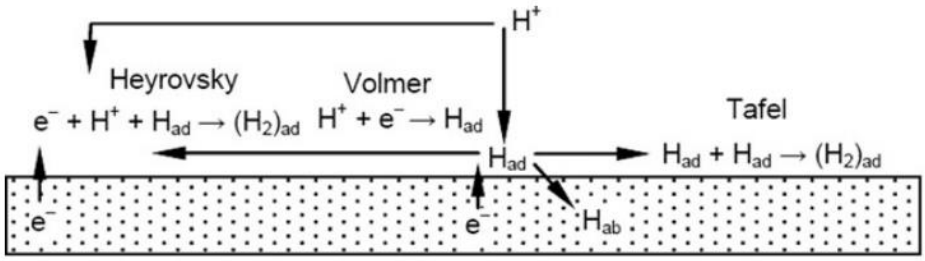

Figure 8 Heyrovsky, Volmer and Tafel reactions for hydrogen adsorption in acidic solutions [15]

B2) Cathodic hydrogen charging

The main difference with the previous scenario is the possibility of hydrogen entry from neutral instead of acidic mediums [15]. Hydrogen is formed in the cathodic polarized electrode, in which the reduction of water occurs due to the neutral pH (possible with high PH mediums as well) (Equation (4)). Hydrogen can be then adsorbed.

$$H_2O + e^- \leftrightarrow H_{ad} + OH^- \quad (4)$$

Current density is the limiting factor for this process to occur [13]. Hydrogen solubility depends, according to Sieverts law on the square root of the current density when hydrogen comes from an aqueous environment. When it is absorbed in its gas phase hydrogen solubility depends on the square root of the hydrogen pressure.

For any of the scenarios there is a possibility that the adsorbed hydrogen is not absorbed [8]. Instead, hydrogen can recombine into a diatomic molecule and leave the metal surface in the gas phase. To ensure the total absorption of the hydrogen, for research purposes, recombination positions can be used to avoid the recombination such as thiourea (CH4N2S), ammonium thiocyanate (NH4SCN), arsenic oxide, hydrogen sulfide, etc. [8] [15] [13].

2.2.2 Hydrogen diffusion and trapping

After absorption, diffusion of hydrogen is the next step. The concentration gradient is the driving force, enhancing hydrogen atoms to diffuse through interstitial sites [7]. The diffusivity also depends on each material and is expressed through the diffusion coefficient [13] [7]. This can be model through Fick's first law (Equation(5)).

$$J = -D\frac{\partial C}{\partial x} \tag{5}$$

D ($m^2\ s^{-1}$) is the diffusion coefficient and ∂C/∂x is the concentration gradient [13] [7].

The diffusion coefficient can also be expressed through an Arrhenius equation since it depends on the temperature (Equation(6)) [13] [7]:

$$D = D_o \exp\left(-\frac{Q}{RT}\right) \tag{6}$$

D_0 ($m^2\ s^{-1}$) is the temperature-independent pre-exponential factor, Q ($J\ mol_{-1}$) is the activation energy, R (8.314 $J\ mol^{-1}\ K^{-1}$) is the gas constant and T (K) is absolute temperature [13] [7].

The diffusivity and diffusion coefficient itself depend on the microstructure and therefore the lattice structure [16]. For a BCC lattice, hydrogen tends to occupy tetrahedral interstitial sites since the radius is double the radius of the octahedral sites for temperatures below 100 ºC. For an FCC lattice, octahedral sites have a higher rate of occupancy. In addition, in a BCC lattice, the distance between nearest interstitial sites is smaller (0.11nm) than for FCC lattice (0.18 nm). This results, as well, in a faster diffusivity for BCC lattices since the activation energy to reach the nearest neighbor interstitial site is smaller. Therefore, ferrite (BCC) presents a higher diffusion coefficient than phases like austenite. Nevertheless, temperature, hydrogen solubility, trapping sites and stress play a role in the incorporation of hydrogen to the material [13] [16].

Hydrogen trapping is a phenomenon in which hydrogen atoms are immobilized in the material structure [13]. Trapping sites can be classified in two categories: reversible and irreversible. Reversible traps are characterized by having low activation energy compared with the bonding energy of the site, trapping hydrogen only temporarily. In irreversible traps, high bonding energy

impedes hydrogen movement. In Figure 9, it can be seen the bonding energy of the trap represented as Eb, Ea the interstitial activation energy and Et the total trapping site energy required to release the hydrogen atom.

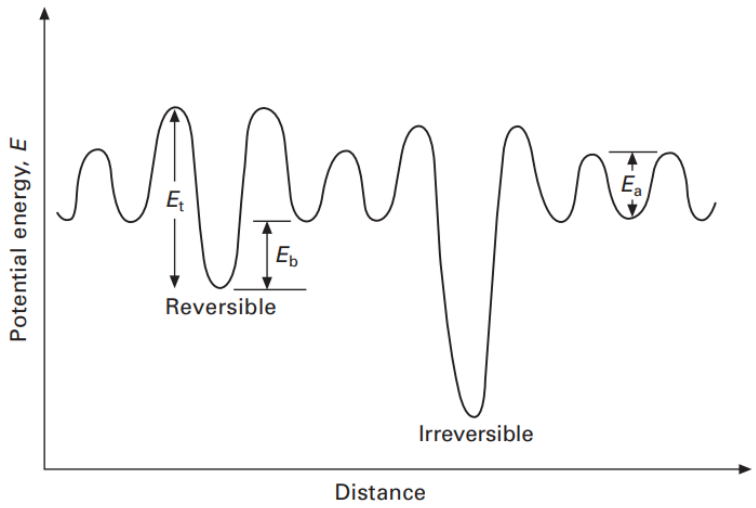

Figure 9 Schematic representation of activation the different activation energies for reversible and irreversible trapping sites compared with the total energy required to liberate a hydrogen atom [16].

Reversible trapping enhances hydrogen enrichment in the material [7]. Irreversible traps, on the contrary, act as sinks for hydrogen atoms though they can increase local stress concentration and decohesion. Nevertheless, rising temperatures can act as an energy source and liberate atoms from irreversible traps as well as decreasing residence time in reversible traps. Reversible or weak trapping and irreversible or deep trapping can also be quantitatively (approximately) classified according to the bonding energy of the trap. Nevertheless, some discrepancies arise. Gi Gao classified point defects as weak traps for bonding energies lower than 15 kJ·mol^{-1} and moderate tapping sites point defects over 20 kJ·mol^{-1}. Dislocations are considered deep traps ranging from 20-60 kJ·mol^{-1}. Interface surfaces and grain boundaries are considered deep traps ranging from 50-100 kJ·mol^{-1}. Padhy et al. refer to reversible traps as the ones that present a binding energy of less than or equal 30 kJ·mol^{-1} and irreversible traps to the ones that present a binding energy superior or equal 50 kJ·mol^{-1} [17].The exact energies are relative depending on the type and chemical composition of the defects.

2.2.3 Hydrogen embrittlement mechanisms

Hydrogen embrittlement in many cases results in catastrophic failure. Nevertheless, the fracture mechanisms behind this phenomenon remain unclear [7] [8] [9] [13]. Many theories have been proposed: Hydrogen Enhanced/Induced DEcohesion (HEDE/HID), Hydrogen Enhanced Local Plasticity (HELP), Adsorption Induced Dislocation Emission (AIDE), Hydrogen Enhanced Strain Induced Vacancy formation (HESIV), Hydrogen Enhanced Macroscopic Ductility (HEMP),

Hydrogen assisted micro-fracture mode (HAM), etc. Furthermore, combination of some of these mechanisms is possible. A definitive answer hasn't been reached since obtaining experimental evidence of hydrogen behavior is a difficult and complex endeavor due to its time dependence. Here three of the main mechanisms are explained: HEDE, HELP and AIDE.

HEDE

It was first postulated by Pfeil in 1926 [18].However, it was Troiano in 1959 who developed and Oriani who contributed to the theory quantitatively [9] [13] [18].This theory proposed that it is the loss of strength or cohesion among the metal atoms which leads to a brittle fracture through cleavage [9] [13] [18].The reason behind this fact, it is that the hydrogen electron, placed at the 1s shell, transfers to the 3d iron shell [13] [19] [18]. This generates a repulsive force in the iron atoms, since there is an increase of the band electronic concentration and therefore the interatomic forces become weaker [19]. From a macroscopic perspective, decohesion starts when a critical crack tip opening displacement (CTOP) is reached. Maximum stresses applied are higher than the interatomic cohesive force, propagating the crack. This mechanism tends to occur near the crack tip since hydrogen tends to diffuse and accumulate in areas where high stresses are located: particle matrix interfaces, grain boundaries near the crack tip or maximum hydrostatic stresses sites [7] [9]. However, traces of partially ductile fracture have been observed in hydrogen embrittlement surfaces such as slip traces, that HEDE can't explain (Figure 10) [13] [20].

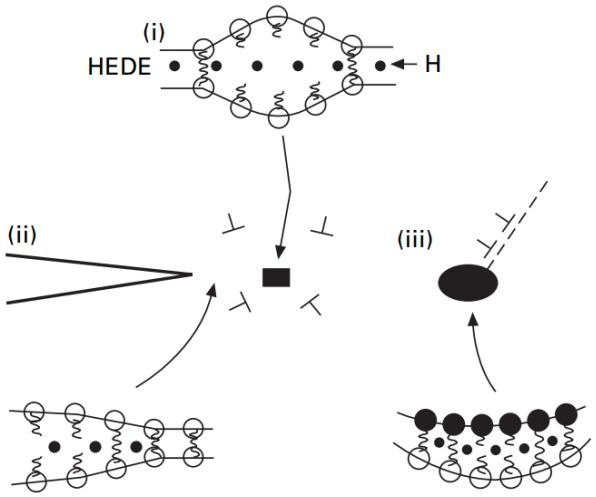

Figure 10 Schematic representation of HEDE mechanism. i) hydrogen position in the lattice ii) adsorbed hydrogen and iii) hydrogen allocated at particle- matrix interphase [9]

HELP

Hydrogen enhanced localized plasticity was first proposed in 1972 by Beachem [8] [9] [13] [17] [18] [21]. Birnbaum and Sofronis (1994), and Robertson (2001) contributed with evidence to this model with SEM fractography images showing the presence of small dimples [8] [13] [18]. This mechanism is based on the enhancement of dislocation movement due to the localized high concentration of hydrogen usually near the crack tip. Hydrogen is attracted to the elastic field, forming hydrogen atmospheres [7] [13] [20] [21]. This leads to a shielding effect, protecting dislocation from being stopped when encountering precipitates or other dislocations and accelerating them. In addition, hydrogen has an effect on other dislocations packing them closer or reducing cross-slip since it stabilizes edge components of dislocations [21].There is also a theory based on thermodynamic principles that links hydrogen to the reduction of dislocation formation energy by Kircheim. In addition, Hwang and Bernstein discovered the role of dislocation in hydrogen transportation since it is bound to dislocation cores [8].Nevertheless, fracture presents itself as brittle macroscopically, as modeled with HEDE (Figure 11).

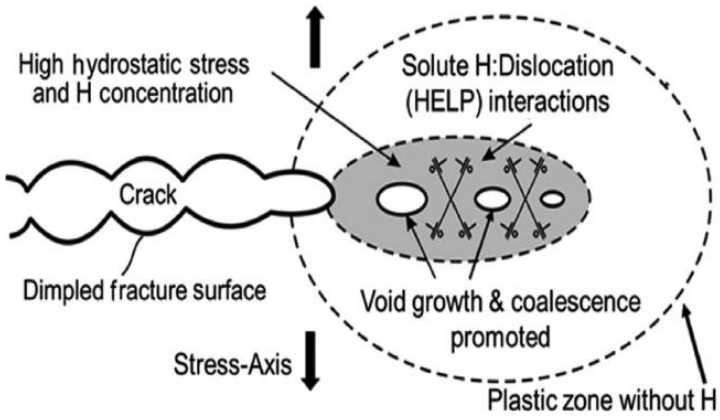

Figure 11 Schematic representation of HELP mechanism [9]

AIDE

This mechanism was proposed by Lynch in 1976 based on some initial hypotheses proposed by Clum in 1975 [18]. Adsorption-induced dislocation emission is a mechanism that lies halfway between the HEDE and HELP mechanisms [13] [9] [18]. Stress concentration at the crack tip makes hydrogen adsorption richer in this area. Hydrogen induces decohesion of the atoms, reducing its cohesive strength as in HEDE mechanism. This phenomenon promotes nucleation of dislocation at the surface and its movement causing plastic deformation by microvoid nucleation and localized slip as in the HELP mechanism. These dislocations are emitted ahead of the crack tip and cause microvoid coalescence at lower strains as well as crack opening (Figure 12).

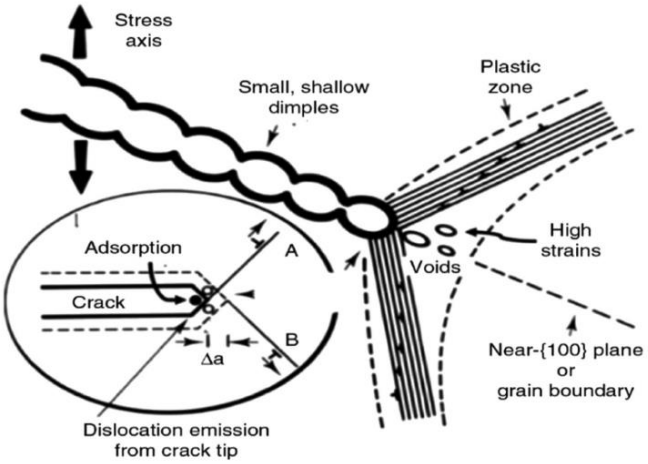

Figure 12 Schematic representation of AIDE mechanism [9].

HESIV

Hydrogen Enhanced Strain-Induced Vacancy formation was first studied by Nagumo on a nickel-based alloy in 2004 [8].This phenomenon is visible during a tensile test. Hydrogen increases vacancy formation since it reduces its formation energy [22]. Strain enhances dislocation interactions such as annihilation leading to a higher vacancy density. This can be a retroalimentary mechanism since hydrogen uptake will increase with higher vacancy concentration [8]. As a result, vacancies tend to coalesce and form microvoids and these one's themselves tend to coalesce into larger ones leading to a decrease in ductile crack resistance [20].

2.3 METHODS TO INVESTIGATE HYDROGEN SUSCEPTIBILITY

Hydrogen susceptibility, as a measurement of a material resistance to be impacted by the presence of hydrogen, can be evaluated in different manners. The first possibility is to employ techniques that allow for measuring hydrogen content in the material after being exposed to a hydrogen environment. This is the case for the Devanathan-Stachurski cell (DS cell) or Thermal Desorption Spectroscopy (TDS). However, measuring hydrogen susceptibility through mechanical testing is also possible. Measuring the deterioration of mechanical properties through tensile test is an indicator of hydrogen susceptibility. In this section only these three techniques are exposed since they are the most representative for the experimental work among the wide range available.

2.3.1 Hydrogen measurement techniques

The Devanathan-Stachurski cell (DS cell) is a hydrogen measurement technique (Figure 13). It can also provide information about hydrogen diffusivity, through hydrogen diffusion coefficient, and trap density energies [13] [23] [24]. The setup consist of two electrochemical cells connected by the metal object of investigation, that functions as membrane and working electrode for both cells. One of the cells is used to produce hydrogen by reduction from the solution. For this purpose, a potential is applied to cathodically polarize this cell [13] [23]. Hydrogen is absorbed by the material in this face (entry side) and diffuses through the bulk [13] [23] [24]. A certain amount (hydrogen that is not confined in irreversible traps) reaches the exit side of the material in the other cell. Here, hydrogen is oxidized applying an anodic potential. The anodic current between the sample and the counter electrode of that cell is measured, as it is the parameter that determines the amount hydrogen [13].Palladium coatings are commonly used to protect exit side from passivation [13] [23] [24].

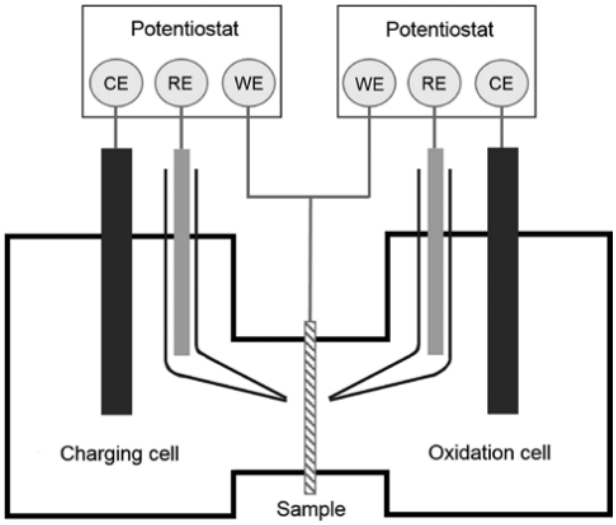

Figure 13 Schematic representation of a Devanathan-Stachurski cell [13].

Measuring hydrogen is also possible through Thermal Desorption Spectroscopy (TDS). It is a non-isothermal technique to measure hydrogen loss [8] [13] [25]. It can quantify desorption, determine the activation energy of the trapping sites and the diffusion coefficient.

Pre-charged samples are heated at different temperature increments [8] [25]. Due to different activation energies of the traps, lower temperatures are needed to liberate hydrogen from reversible traps than irreversible traps. Therefore, the type of traps can be identified and linked to hydrogen flux at that temperature. Activation energies can be calculated as well by repeating measurements at different heating rates. This can be expressed by Equation (6) (a simplification from the original equation done by Lee et al.) [25].

$$\frac{dln(\Phi/T_{\max}^2)}{d(1/T_{max})} = -\frac{E_A}{R} \quad (7)$$

Where ϕ is the temperature heating rate, T_{max} is the temperature in which maximum desorption speed is reached or the 'peak temperature', E_A is the activation energy of the traps and R is the gas constant [8] [25]. As it can be seen from Equation(6) that the activation energy can be obtain from the slope ($-E_A/R$), when n (ϕ/T_{max}^2) is plotted vs $1/T_{max}$ [8]. Regarding the number of trap sites or trap density, information can be obtained by the number of desorption peaks obtained [13].

The TDS set up is composed of a heating device and a thermocouple that attaches to the sample to control the temperature [24]. A quadrupole mass spectrometer is required to measure the desorbed hydrogen. The current of the ionized hydrogen atoms is proportional to the desorption rate which is recorded as a function of the sample temperature or time. A vacuum chamber is also part of the set up as well as coolant. Data is acquired by the computer (Figure 14) [26].

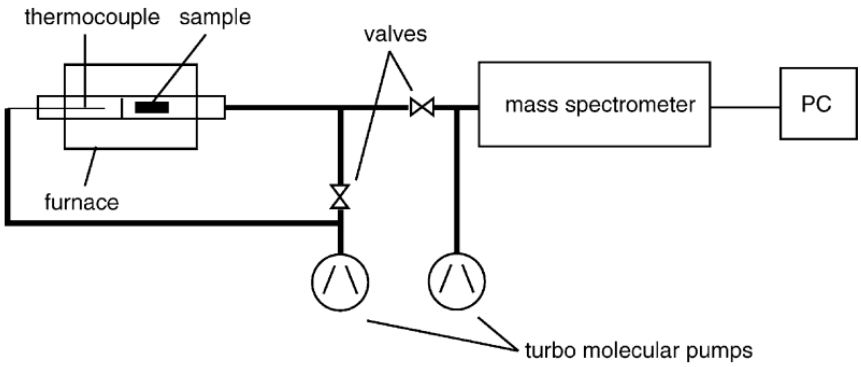

Figure 14 Thermal Desorption Spectroscopy set up main elements [27].

Nevertheless, TDS presents some disadvantages. Microvoids, dislocations and grain boundaries can become difficult to distinguish since temperatures can overlap for hydrogen desorption. This technique doesn't take geometry influence into account [8] [25]. This only becomes relevant when lattice diffusion energy is similar to trap energy. The temperature of the experiment can impact the annihilation of some defects. In addition, the time required to create vacuum in the chamber can lead to reversible trap desorption before measurement recording starts.

Both techniques, DS cell and TDS, are similar in spatial resolution. The detection limit is below 0.1 ppm for DS cell and Below 0.1 wppm or 1019 at/cm^3 for TDS [13] . These are generalized data that can vary per specific instrument. The DS cell's main advantages are the relatively simple set up. However, it requires long times if the specimens are thick to perform electrochemical permeation tests. Corrosion in the specimen exit can occur as well, so palladium coatings are required. Corrosion in the cathodic cell can alter measurements. On the

other hand, TDS can measure hydrogen from reversible and irreversible traps separately. Nevertheless, it also presents shortcomings.

2.3.2 Mechanical Testing

Investigating and measuring deterioration of mechanical properties that lead to failure is a good approach to measure the hydrogen susceptibility. Changes in ductility, tensile strength, and yield point can be done with the help of tensile test [13].

This method provides information of the conditions of the material after being subjected to hydrogen charging. This information is presented in the form of stress- strain curves. Modalities of this experiment can vary from stress control to strain control, static or dynamic loading. The most common tests are: Slow Strain Rate Test (SRRT), Constant Load Test (CLT) and Conventional Strain Rate Test. Linearly Increasing Stress Test (LIST) (referred as Stepwise Load Test as well) is also possible.

Slow Strain Rate Test

This is the most widespread type of tensile test performed for determining hydrogen embrittlement susceptibility. It's a strain controlled test that is performed until failure [13]. The strain rate applied is four orders of magnitude smaller than the one employed in conventional tensile tests. According to ASTM G129 (Standard Practice for Slow Strain Rate Testing to Evaluate the Susceptibility of Metallic Materials to Environmentally Assisted Cracking), valid values range between 2.54×10^{-3} and 2.54×10^{-6} mm/s [28]. Slow Strain rate enhances the hydrogen diffusion distance due to stress concentration [13] [29]. Therefore, the strain rate is one of the external parameters that influences hydrogen embrittlement [13] [29] [30].

A Slow Strain Rate Test can be performed in a short time compared with Constant Load Testing, Stepwise Load Test and obviously Conventional Strain Rate Test [13] [30]. In addition, no specification of the time is required since samples are tested until failure. This technique presents less dispersed results than the Constant Load Test (CLT) method [13]. It is an advantage that the setup is not complex and flexible to modifications.

Nevertheless, SSRT present some disadvantages. It has been regarded as a qualitative method to identify the susceptibility of materials to hydrogen Embrittlement [30]. Comparison with in-service measurement results is inadequate or not representative since results are excessively or insufficiently conservative, as it is phrased in ASTM G129. In addition, sub-critical growth appears while SSRT testing. This can be translated in lower applied stress than the one that will be actually required to produce fracture without the presence of cracks that don't directly lead to failure. Slow Strain rate testing is also highly influenced by dimensions and surface finish of the samples.

Although, Slow Strain Rate testing is usually employed between certain ranges, no strain rate threshold has been stablished for DP1000. Further investigation is needed to delimit the strain value for when its effect is negligible.

Constant load test

This method is a static loading test that measures the critical hydrogen concentration that the material can hold before it undergoes failure [29]. SSRT and CLT themselves, are comparable in the amount of diffusible hydrogen and correlated nominal fracture stress [13]. However, times to perform this experiment method are significant. Nevertheless, procedures are simple to implement. Scharf et al. also demonstrated the influence of the materials surface finish in the results, such as the pre damage caused by punching, laser cutting and milling [31].They also mentioned the influence of the homogeneity of the microstructure and the importance of the stress intensity factor for hydrogen embrittlement. Their study was conducted on DP 1000 [31]. However, no investigation was carried on surface finish conditions nonrelated to the piece cutting process.

Conventional strain rate test

As its name suggests, the specimens are tested according to the common parameters of widespread conventional tensile test [13] [29]. Specifications of this test are compiled in ASTM G142– 98 [32] This static strain control method implies high speed strain rate when compared to Slow Strain Rate Test methodology. Therefore, hydrogen allowed to diffuse into the material during the test is practically negligible. Hydrogen concentration at a stress concentration point is equivalent to the average contained in the piece tested. In addition, CSRT samples need to be previously charged as uniformly as possible [29]. Short test times, however, are beneficial from a practical point of view [13].

Linearly Increasing Stress Test

In Linearly Increasing Stress Test or Stepwise Load Test, increments of stress are applied alternating with sustained load periods until failure is reached [13]. Specifications of this test are compiled in ASTM F1624 – 12 [33]. During holding periods, hydrogen content almost reaches equilibrium, which makes it possible to approximately calculate hydrogen distribution. This is feasible since sustained load phases allow hydrogen distribution not to depend on strain rate and hydrogen has time to accommodate to new stress distributions. This raises the complexity of the experiment and process due to hold time selection [34]. A schematic representation of a Stepwise Load Test example can be seen in Figure 15.

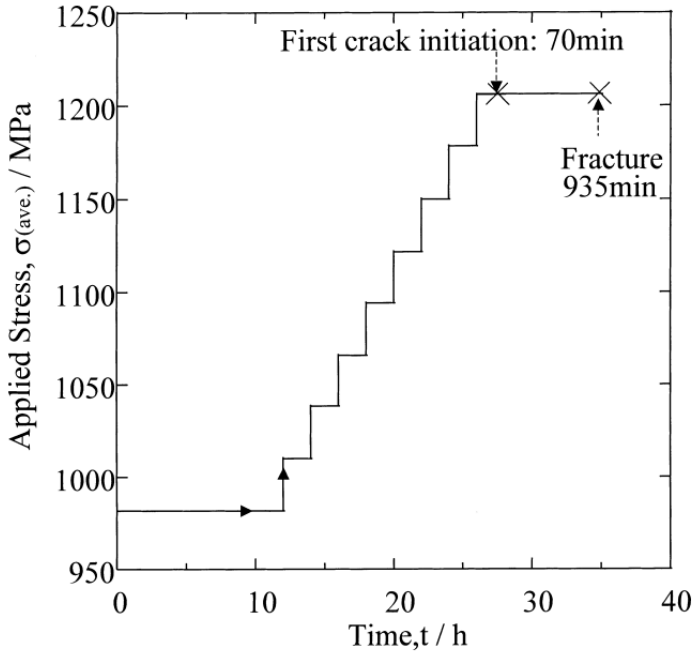

Figure 15 Schematic representation of a Stepwise Load Test example [32].

A summary of the advantages and disadvantages different tensile testing techniques is displayed in Table 1.

Table 1 Advantages and disadvantages of the different tensile testing techniques [9].

Technique	Advantages	Disadvantages
Constant Load Test Slow Strain Rate Test	Simple loading procedure Short test time No problem with specifying of test time	Longer test time
Conventional Strain Rate	Very short test time	Very uniform pre-charging required
Stepwise Load Test	Independence from specimen dimensions Independence from stress conditions	More complicated loading procedure

2.3.3 Fractography

Hydrogen can impact the fracture mode of the specimens, though it's not always necessarily the case [35]. Hydrogen tends to modify ductile fracture into brittle fracture. Ductile characteristic micro void coalescence can turn into intergranular failure, cleavage, quasi-cleavage or even shallower microvoids. Intergranular fracture can be defined as a brittle mode that implies crack formation and propagation alongside grain boundaries. Cleavage can be characterized by fracture along clearly defined planes. There is not a unique description to define quasi-cleavage

[36]. This type of fracture has been described as a mixture of ductile and cleavage fracture or a fracture similar to cleavage without well-defined crystallographic orientation of the fracture path or failure along non-cleavage planes. This fracture morphology can appear in dual phase steels, ferritic, austenitic and martensitic steels. Quasi cleavage usually exhibits river marks (fine lines) that parallel to the crack propagation direction [35].

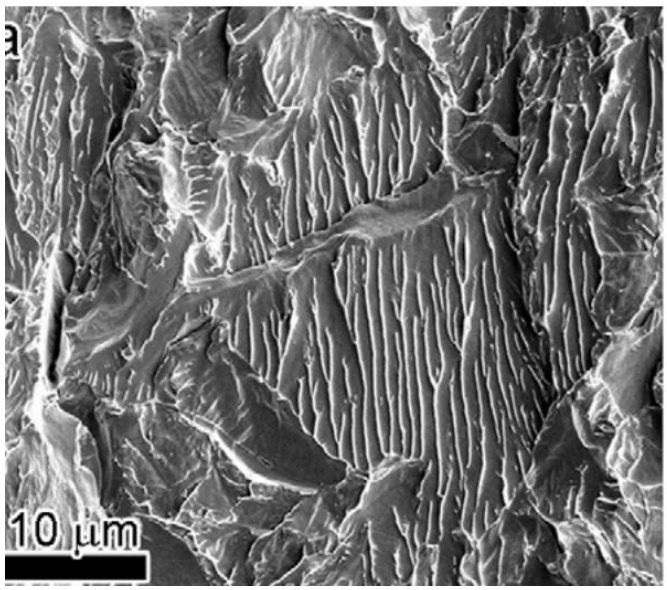

Figure 16 SEM image of quasi-cleavage fracture [35].

2.4 FACTORS INFLUENCING HYDROGEN EMBRITTLEMENT

Hydrogen embrittlement can be influenced and controlled by different factors. These parameters can be internal to the material such as the microstructure and defects or external related with testing parameters such as temperature, strain rate, testing environment or stress concentration conditions.

2.4.1 INTERNAL FACTORS

Microstructural features

As it was previously mentioned, different microstructures are a key parameter for hydrogen diffusion, solubility and as a final result hydrogen embrittlement susceptibility [13]. In addition, the volume fraction of each phase plays an important role in hydrogen embrittlement as well as the distribution of each phase in the steel. Interphases between different microstructures are relevant for hydrogen concentration and crack propagation. These factors become of great interest for dual phase steels.

Hydrogen diffusion can enhance hydrogen embrittlement. It depends on the microstructural phases present in the material. Diffusion and diffusion coefficient are directly related to the lattice atomic density or packing of each of the steel phases [13]. Austenite due to its close pack lattice, face centered cubic lattice, presents a high hydrogen solubility but a low diffusivity coefficient. Martensite's atomic packing is lower compared with austenite but higher than ferrite, exhibits values in between these two types of lattices. Ferrite, a body centered cubic lattice, presents a low hydrogen solubility but a higher diffusion coefficient due to a lower packing density of the lattice.

This is applicable to dual phase steels that present ferrite and martensite as their microstructure [37]. However, the critical parameter for hydrogen embrittlement is the martensite volume fraction, since martensite exhibit lower diffusion coefficient and contains irreversible trapping sites. Nevertheless, Wang et al. set a martensite threshold at 68.3% for hydrogen diffusivity. Beyond this value martensite hydrogen diffusion coefficient reaches plateau. However, hydrogen embrittlement keeps increasing with increasing martensite content. Distribution of the phases can be regarded as a determining factor as well, linked to martensite proportion.

Hydrogen behavior is different for the martensite content. It can be separate according to low martensite (below 30%), intermediate content (between 30% and 68.3%) and high content or above the diffusivity threshold (68.3%) [37].

Hydrogen atoms' preferential path, for low martensite content (distributed as islands inside the material), is ferrite, leading to a higher diffusivity [37]. Lower trapping leads to smaller stress concentration (less distortion of the lattice is produced by hydrogen accumulation) and it allows the material to deform in a ductile way, due to the capability of ferrite to prevent expansion of the crack, absorbing plastic deformation energy.

On the contrary, for intermediate martensite percentages, the ferrite-martensite interface expands, acting as a trap and reducing diffusion. This leads to a stress concentration increase in the interphase between the two phases, that present strain incompatibility though it tends to level off with martensite increment. However, with deformation, ferrite grains decrease in size hindering the ferrite crack propagation prevention and hydrogen trapping, promoting crack nucleation. Therefore, the loss of ductility that bigger ferrite grain leads to shallower dimples than the ones present in a fully ductile fracture.

Over the threshold, martensite is the preferential pathway for atoms to diffuse since martensite will form a continuous network [37]. However, two opposite effects take place. Since martensite is increased, carbon content in the martensite is reduced, eliminating a possible trap site. On the other hand, martensite lath boundaries, dislocations, ferrite-martensite interface as well as the lower diffusivity of this phase, enhance trapping. Therefore, martensite is more prone to crack propagation. Above 68.3%, ferrite size decreases, decreasing interface length leading to lower critical stress fracture values. Cleavage appears as a sign of the brittle fracture.

In summary, hydrogen trapping inside the martensite network and the martensite-ferrite interphase increases hydrogen susceptibility (Figure 17) [37]. It can be analytically probed for dual phase steels by Equation (8). As the hydrogen embrittlement index increases parallel to martensite content since it presents lower diffusion coefficient. Coefficients of this equation are only representative for experiments carried out by Wang et.al.

$$\log(I_{HE}) = 3.13 - 3.54 \times \log(D_{eff}) \quad (8)$$

However, a general calculation of this parameter can be done according to the equation (9).

$$EI = \frac{Elongation\ in\ Air - Elongation\ when\ Charged}{Elongation\ in\ Air} \quad (9)$$

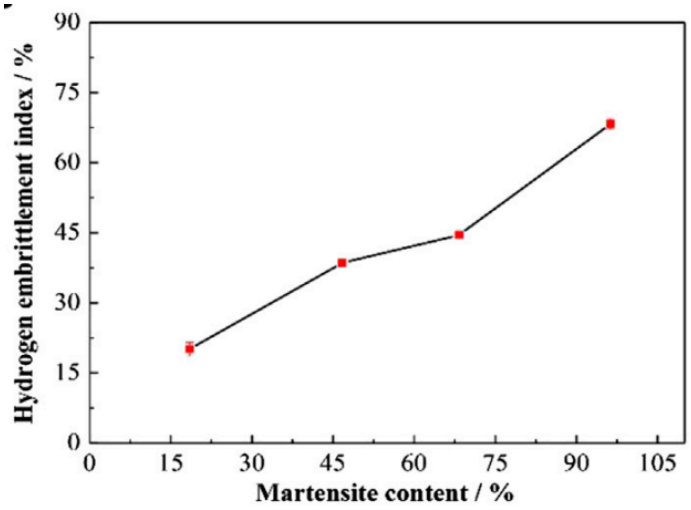

Figure 17 Correlation between hydrogen embrittlement and martensite content in DP steels [37].

2.4.2 EXTERNAL FACTORS

Strain rate and hydrogen pre-charging

Strain rate is one of the parameters that is easily modifiable during the experimental process. Strain rate is closely linked to hydrogen diffusion [38]. Lower strain rates lead to higher hydrogen embrittlement susceptibility. This is related to the distance that a hydrogen atom can diffuse which is related to time. It can be calculated by taking the square root of the product of the diffusion coefficient D (cm^2/s) and the test time t (s) as it can be seen in equation(10).

$$x = (Dxt)^{1/2} \quad (10)$$

Strain rate has some influence on mechanical properties. This was observed for dual phase steels as well [39]. At slow strain rates this parameter causes a reduction in fracture elongation. Nevertheless, tensile strength and yield strength remain unaffected. This is only true for

uncharged samples. Hydrogen charging reduces the yield strength in advanced high strength steels, as well as having a bigger impact in elongation reduction fracture strength when tested at low strain rates [39]. On the other hand, at higher strain rates mechanical properties do not differ for charged or uncharged samples. This can be observed in Figure 18 for different types of Advanced High Strength Steels tested at 10^{-5} s^{-1} and at 20 s^{-1} strain rates. Table 2 collects the data with the specific results for mechanical properties of these steels and their variation, at the different strain rates, charged and uncharged. Charging was performed during 30 min at 10 mA/cm^2 in an electrolyte of 1 N H_2SO_4 + 10 mg/l CH_4N_2S.

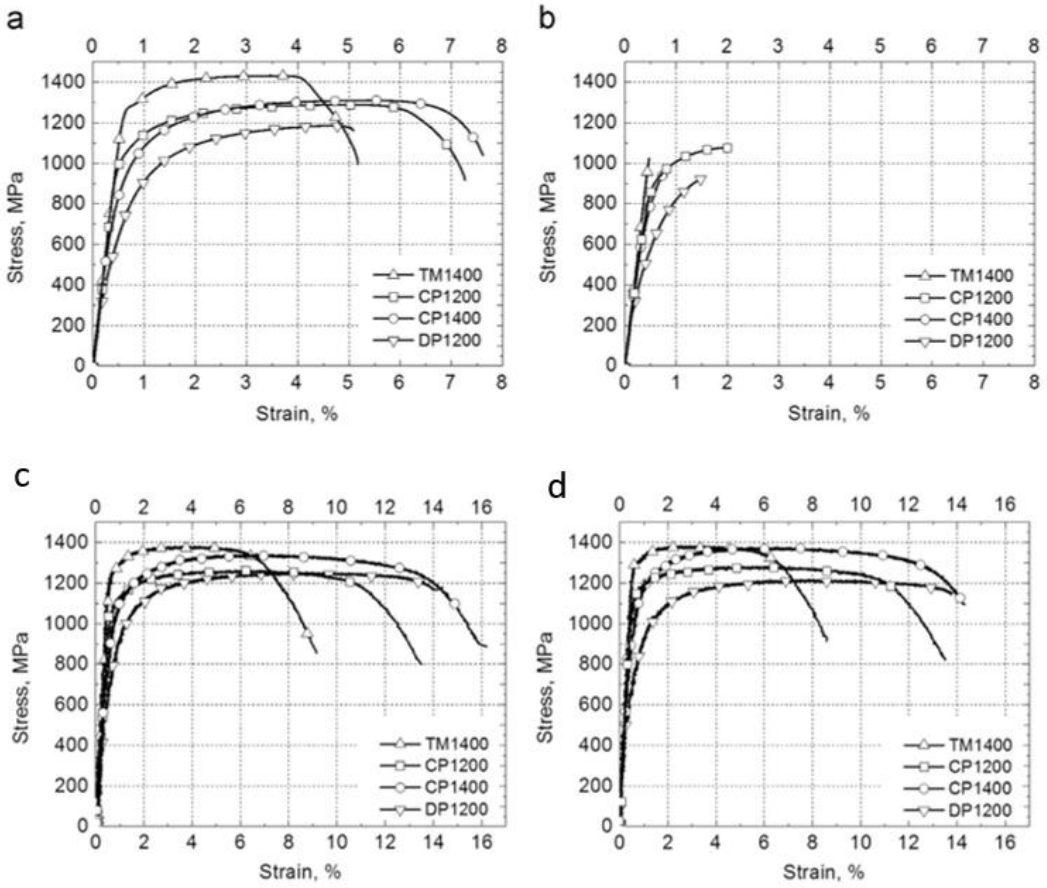

Figure 18 Stress-Strain curves for the different AHSS a) uncharged specimens at 10^{-5} s^{-1} and b) hydrogen charged specimens at 10^{-5} s^{-1} c) uncharged specimens at 20 s^{-1} and d) hydrogen charged specimens at 20 s^{-1} [39].

Table 2 Mechanical properties of the different AHSS at the different strain rates charged and uncharged [39].

	Uncharged specimens						Charged specimens					
Grade	Low strain rate tests, $d\varepsilon/dt = 10^{-5}$ s^{-1}			High strain rate tests, $d\varepsilon/dt = 20$ s^{-1}			Low strain rate tests, $d\varepsilon/dt = 10^{-5}$ s^{-1}			High strain rate tests, $d\varepsilon/dt = 20$ s^{-1}		
	R_m MPa	$Rp_{0.2}$ MPa	A_{50} %	R_m MPa	$Rp_{0.2}$ MPa	A_{20} %	ΔR_m %	$\Delta Rp_{0.2}$ %	ΔA_{50} %	ΔR_m %	$\Delta Rp_{0.2}$ %	ΔA_{20} %
DP1200	1237	673	4.5	1253	624	14.2	-25	-9	-78	-3	-7	-4
CP1200	1289	1056	6.9	1263	1064	13.3	-16	-11	-78	2	5	0
CP1400	1310	902	7.2	1343	975	16.1	-27	-2	-95	3	-10	-12
TM1400	1431	1287	4.7	1381	1256	9.0	-29	n.d	-100	0	3	-7

Where Rm is the tensile strength, $Rp_{0.2}$ is the yield strength and A_{50} refers to the elongation at fracture at 10^{-5} s^{-1} and A_{20} elongation at fracture at 20 s^{-1}. The properties on the right side of the table, for the charged experiments, are expressed as an increment in percentage over the uncharged samples.

T. Depover et al. also compared the influence of hydrogen pre-charging and strain rate. Pre-charging was performed for 2 hours using 1 g/L of thiourea in a 0.5 M H_2SO_4 solution at a current density of 0.8 mA/cm^2 [38]. Strain rate was measured by the crosshead deformation speed (mm/min). Test were performed at 5, 0.5 and 0.05 mm/min. Diffusion distance was calculating through the aforementioned equation (equation (10)), taking the diffusion coefficient value as 7.46 x 10^{-7} cm^2 /s for the DP600 steel. Stress – Strain curves are displayed in Figure 19. Precise results are shown in Table 3. Deterioration of ductility is measured as embrittlement index (EI)(Equation(9)).

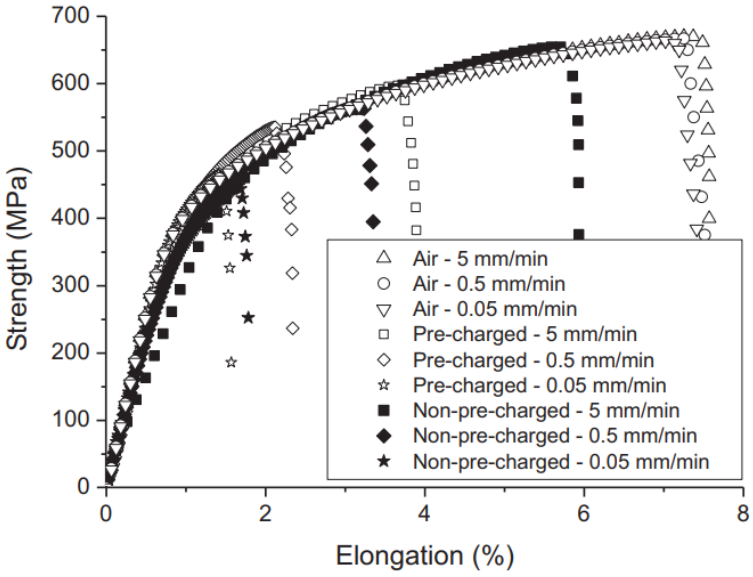

Figure 19 Stress- strain curves for different crosshead deformation speeds for charged and uncharged samples [38].

Table 3 Hydrogen diffusion distant and embrittlement index results for different crosshead deformation speeds for charged and uncharged samples [38].

Cross-head deformation speed (mm/min)	Diffusion distance x (µm)		Embrittlement index EI	
	Pre-charged	Non-pre-charged	Pre-charged	Non-pre-charged
5	53	65	49%	22%
0.5	145	168	69%	55%
0.05	390	410	79%	76%

T. Depover et al. in a different study compared the effect of different strain rates with different charging parameters [40]. Larger currents lead to a higher embrittlement index percentage. However, independently of the pre-charging, smaller strain rates lead to higher hydrogen

content and therefore higher embrittlement index percentages. Researches charged samples of DP600 steel at 0.8 mA/cm^2, 5 mA/cm^{2}and , 25 mA/cm^2. The strain rates chosen were 0.0167 s^{-1} and 1.67 s^{-1}. Engineering stress- strain curves can be observed in Figure 20.

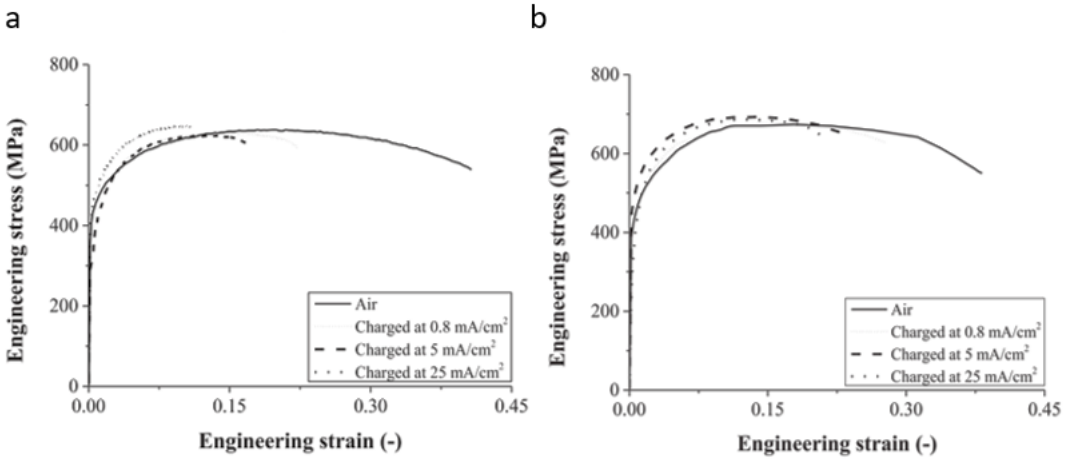

Figure 20 Stress- strain curves a) at 0.0167 s^{-1} for different charging currents and b) at 1.67 s^{-1} for different charging currents [40].

In addition, the fraction initiation spot is also a consequence of strain rate and hydrogen pre-charging [40]. Slow strain rate leads to hydrogen accumulation on the samples due to a higher diffusion and stress concentration time. This leads to localized necking and displaces the fracture initiation to the edge of the sample for the case of previously charged specimens. On the other hand, high strain rate as well as non-pre-charged samples show fracture initiation at the center of the specimen as well as presenting a ductile fracture with non-localized necking. All samples tested at 1.67 s^{-1} presented fracture initiation at the center independently on the charging current. Samples tested at 0.0167 s^{-1} showed fracture at the center for non-pre-charged condition and at the edge for all the samples with different charging currents. Results can be observed in Figure 21 and summarized in Table 4.

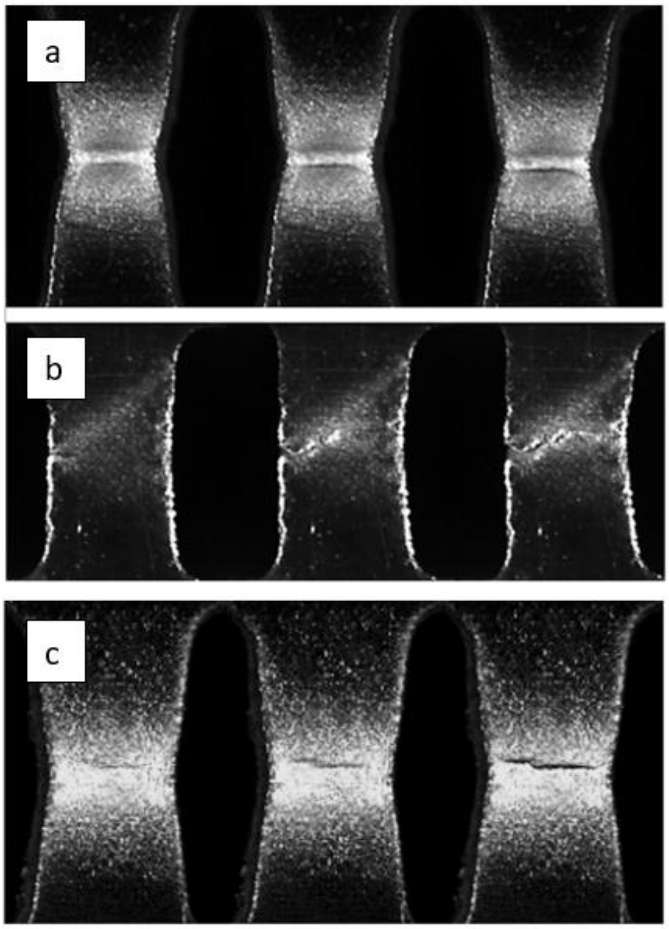

Figure 21 images of tensile test performed a) in air at strain rate of 1.67 s^{-1} b) after H charging (5 mA/cm^2) at strain rate of 0.0167 s^{-1} and c) after H charging (0.8 mA/cm^2) at strain rate of 1.67 s^{-1} [40].

Table 4 Summary of fracture initiation spot for different charging currents and strain rates [40].

Fracture initiation point	Air	0.8 mA/cm^2	5 mA/cm^2	25 mA/cm^2
0.0167 s^{-1}	Center	Edge	Edge	Edge
1.67 s^{-1}	Center	Center	Center	Center

In the case of dual phase steels, damage evolution, nucleation and arrestability has been related to strain rate [41]. Damage initiation has been associated with different local plastic deformation between martensite and ferrite. T. Kumamoto et al. stated that increasing strain rate leads to a decrease in damage nucleation at martensite. This fact can be linked to hydrogen assisted vacancy formation since is a strain induced phenomenon. Higher times leads to higher vacancy diffusion when they act as preferential crack initiation sites. Voids coalescence becomes easier since distance between voids decreases. Low strain rate contributes as well to shortening damage arrest regime. This might be due to a reduction of crack propagation resistance due to localize plasticity in ferrite grains.

In-situ, ex -situ testing: hydrogen desorption

One of the main issues for accurate hydrogen measuring during experimental procedure is hydrogen desorption. This can occur or in between the charging step and tensile testing and later TDS measurement or even during TDS vacuum forming.

Hydrogen desorption still occurs in different moments during tensile testing ex-situ [42]. Though it still depends on the method selected and microstructure of the material. During constant strain rate testing, Y. Matsumoto et al. observed desorption during elastic deformation due to hydrogen transportation by dislocation for martensitic steels. Tough this effect diminished with increasing time. When yield point is reached, desorption is mitigated due to hydrogen being trap by new defects that act as trapping sites.

This is partially overcome by in-situ hydrogen charging. In-situ testing reproduce with accuracy in service conditions. Measurements of hydrogen concentration and diffusivity become more reliable and precise [43].

Stress concentration: notches

Stress concentration through the presence of notches can influence hydrogen behavior and accelerate fracture [44] [45]. Without being in the presence of hydrogen the effect produced depends on the type of material and the specimen notch concentration factor [45]. For ductile materials, a triaxial state of stress results in an increase of the material strength by delaying the yielding point appearance and increasing the stress required for fracture to occur. However, ductility is strongly decreased due to void nucleation and growth, generated by the triaxial state of stresses and localized plastic deformation at the notch. When these effects are combined with the presence of hydrogen, it enhances hydrogen embrittlement [44] [45]. As aforementioned, triaxial and hydrostatic stresses lead to hydrogen diffusion and concentration, in this case at the notch. In addition, strain at the notch differs from the bulk strain since deformation is localized, increasing faster than in the rest of the material. This attracts hydrogen from the surface and flanks to tip of the notch [45].

Notch severity is linked to the stress concentration factor Kt. According to M. Wang et al. a higher stress concentration implies he biggest reduction in notch strength for hydrogen charged samples [46]. The loss in notch strength can be described as a power law with respect hydrogen content. They exemplified this affirmation in experimental results obtained from AISI 4135. Samples were charged with 0.5 wppm. Notches with stress concentration of Kt= 2.1, 3.3 and 4.9 were tested. Notch strength decreased from 1500MPa, to 1000MPa and 700 MPa respectively (Figure 22). Furthermore, stress concentration can modify fracture surface around the notch. This parameter is of higher relevance than notch shape (sharp or blunt) itself [47]. The greater difference between sharp notches and blunt ones is the bigger stress affected area by the blunt notch and therefore by hydrogen embrittlement being more detrimental under certain circumstances.

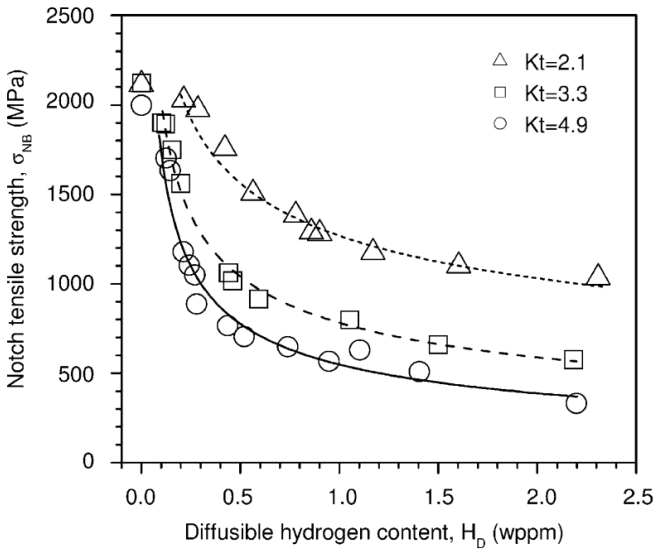

Figure 22 Notch tensile strength for different stress concentration as a function of diffusible hydrogen content [46].

This is verified for dual phase steel as well [48].T. Depover et al. observed a loss in ductility which was higher for deeper notches since stress concentration is higher as well. That corresponds with results obtained for DP600, without notch, a notch of 0.1R and 0.5R with and without being preloaded at a constant net section of 280 MPa, with and without simultaneously being hydrogen charged for 2h (Figure 23).

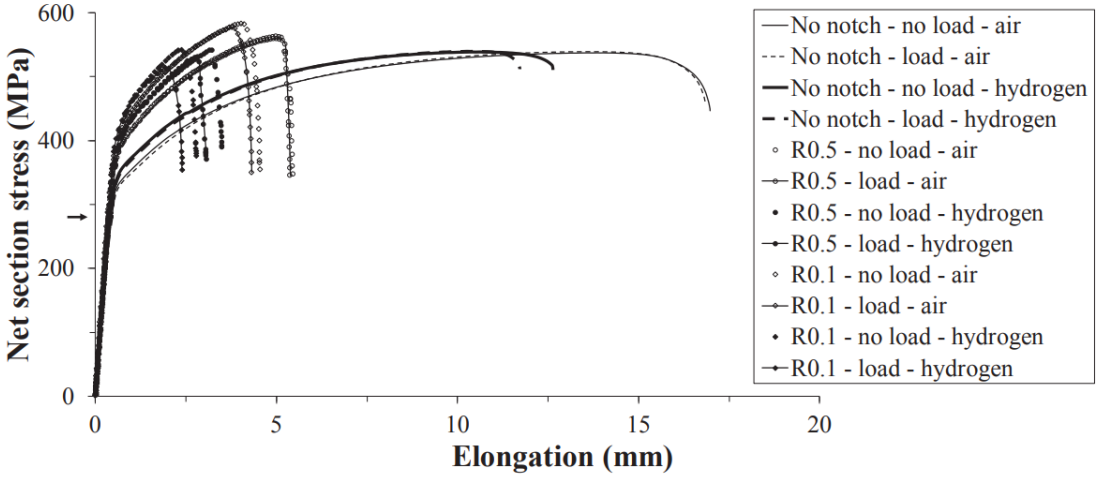

Figure 23 Net section stress- elongation curves for different notch geometries, with and without hydrogen charging and with and without a constant net section stress of 280 MPa [40].

Stress concentration and localized plasticity can affect hydrogen distribution during slow Strain Rate testing [48]. Trapping at the notch root is increased with hydrostatic stresses and plastic deformation since it creates lattice defects.

Further investigation is needed for dual phase steels in particular since not enough data is available in the literature.

Pre-strain

Pre straining and deformation is one of the remaining parameters for farther investigation in DP steels as well [49]. However, A. Drexler et al. tested several dual phases at 2 %, 5 %, 10 %, 15 % and 20 % with respect to the yield point. This reflected the strain effect in hydrogen susceptibility. Increasing plastic strain increases hydrogen absorption. This could be linked to increase of trapping sites with plastic deformation. The relationship, though, depends on the DP microstructure, hydrogen content during straining and strain percentage. Tensile test experiments were conducting ex-situ.

K.S. Reddy investigated the role of pre-strain for DP 980 in situ and ex-situ conditions [43]. The material was pre-strained up to 3 % and 6 % engineering strain and in-situ tensile tested (50 %, 110 %, and 125 % of the yield stress (YS)). Results show that increasing pre-strain percentage leads to higher hydrogen reversible trapping and concentration and lower diffusivity due to higher dislocation density. Pre-strain leads as well to higher misorientation for ferrite and martensite grains.

From these studies the importance of situ and ex-situ charging can be derived and its necessary deeper investigation to understand the effect of elastic stress on hydrogen behavior and its repercussion in the posterior plastic deformation [43].This can be understood as the needed comprehension of the impact that pre-straining, in-situ, in the elastic regime might have on the elongation at fracture.

2.5 SUMMARY

Advanced High Strength Steels are great candidates to allow weight reduction in the automotive industry. Their implementation will lead to a decrease in material and energy consumption as well as green gas emissions. Advance High Strength Steels will contribute to reach zero emission in 2050. However, their implementation is not possible without addressing their main disadvantage: they suffer from hydrogen embrittlement. A lot of effort has been put into understanding and controlling hydrogen embrittlement in this type of steels. However, a lot of unknowns still remain to be solved, especially for dual phase steels.

In this study, endeavor has been put into gather, cover and present the essential topics necessary for the future in investigation and as result to discover research gaps. Therefore, the following conclusions were extracted:

1. Hydrogen embrittlement has a big impact in a wide range of sectors. Hydrogen uptake can occur from manufacturing processes to rich hydrogen environment, gaseous or liquid. However, for research purposes hydrogen can be charged. Hydrogen is first adsorbed on the surface to later being absorbed in the atomic form. After this step hydrogen diffuses through the material. Diffusivity depends on the lattice structure of the material as well as the temperature. In this process hydrogen can be trapped in reversible and irreversible sites. Hydrogen embrittlement proposed mechanisms are diverse and none of them has been proved as the main one. The most well-known are HEDE, HELP, AIDE and HESIV.

2. Advanced High Strength Steel have been present in the automotive sector since 1980. Dual phase steels were the first ones to be implemented of the family. DP steels are mainly composed by Carbon, Silicon, Manganese and Iron. Martensite and Ferrite are the phases that compose their microstructure. DP1000 will be the material selected to conduct the investigation.

3. Hydrogen susceptibility can be measured. This can be performed through hydrogen concentration measurements such as Devanathan-Stachurski cell (DS cell) or Thermal Desorption Spectroscopy (TDS). TDS and DS cell present similar detection limits. However, TDS has the capability of detecting separately reversible and irreversible traps. Measuring hydrogen susceptibility through mechanical testing is also possible with tensile test. There is a wide range of tensile test modes that can be performed: SSRT, CLT, CSRT and SLT. SSRT stands out due to shorter test times as well as the interesting effect that it has in hydrogen diffusion. These are the reasons why this type of test will be selected for the experimental work.

   On the other hand, there is no defined threshold that marks the beginning of SSRT effect for dual phase steels. In addition, there is no unification criteria for data obtained from the different tensile tests.

4. External and internal factors influence hydrogen embrittlement. Microstructure is the main internal parameter. Hydrogen embrittlement is directly correlated with the percentage of martensite present in the material and therefore its distribution. Literature states that a higher content of martensite enhances hydrogen susceptibility. Other parameters such as grain size, grain boundaries are disregarded to focus on the phases. Regarding external factors, slow strain rate in combination with pre-charging has been proven to have an effect in hydrogen diffusivity, loss in ductility and variation in the fracture initiation point and damage evolution. It also has been proven that in-situ testing prevents hydrogen desorption during tensile tests. This technique will be selected for the experimental work. In addition, deeper notches are more detrimental to ductility as well as a higher stress concentration implies a loss in notch strength in hydrogen charged samples. Nevertheless, research still needs to be done for dual phase steels. One of the main unexplored factors is the effect of pre-strain in dual phase steels. Studies have been conducted for ex-situ pre-straining. Literature suggests an increasing hydrogen susceptibility with higher pre-straining percentages for this condition.

2.6 RESEARCH QUESTIONS

After presenting the literature review and portraying an overview of the main topics that are the core for this project, some research gaps were identified. Understanding of hydrogen embrittlement in dual phase steels, and in specific for DP1000, is still to be developed.

The following research gap can be extracted from the literature review:

1. The effect of hydrogen on the mechanical properties such as ductility, tensile strength and hardness when pre-straining in situ for a DP1000:
   a) Comparing ex-situ pre-strain under hydrogen pre-charging conditions with in-situ pre-straining results. Evaluate and compare mechanical properties and hydrogen uptake between both testing methods as well as among the different pre-strain values selected. Five samples will be tested per strain percentage.
   b) Finding a threshold value for pre-strain level to characterize when its effect becomes negligible for increasing hydrogen susceptibility.

   Future recommendations for research objectives:

2. The effect of notch geometry and stress concentration for dual phase steels. Compare the threshold value of pre-strain found with the effect of a notch present in the sample.
3. Finding the threshold for strain rate influence to characterize Slow Strain Rate technique for DP1000. In this experimental work, strain rate will be maintained constant since the focused is on the pre-strain effect.
4. Defining a unifying criterion for different tensile test methods to precisely correlate obtained results. During the investigation all tests will be performed under Slow Strain Rate method.
5. Investigation of the influence surface finish in hydrogen embrittlement for dual phase steels. In this experimental work, all samples will be prepared in the same manner. All samples will be fully polished.

3. MATERIALS AND METHODS

This chapter compiles the information regarding data and procedures needed to perform experiments for this thesis. Section 3.1 develops the characterization methods for DP1000. Section 3.2 details the set-up used and the diverse approaches of sample preparation and test procedures.

3.1 Material Characterization

Material was provided in the form of hot rolled metal sheets of 1 m x 1.20 m. Composition, microstructure and mechanical properties of the base material need to be studied to ensure experiments results are valid. Samples were cut and embedded with a Struers CitoPress-5, sanded from P80 up to P1200 with SiC grit and polished up until 1 µm with a Struers LaboPol-5. Afterwards, samples were etched with 5% Nital to study the microstructure through Scanning Electron Microscope (SEM).

3.1.1 Composition

The composition of DP1000 obtained by X-Ray fluorescence (XRF) combined with carbon/sulfur melt analysis is shown in Table 5.Fe, C, Mn and Cr are the main elements present in the studied material.

Table 5 DP1000 composition results using XRF analysis combined with combustion analysis

Fe	C	Mn	Cr	Si	Al	Nb	Ti	P	S
96.98	0.144	2.148	0.538	0.127	0.024	0.015	0.014	0.010	0.003

3.1.2 Microstructure

SEM image of the microstructure of DP 1000 is presented below (Figure 24). Ferrite and martensite are the phases present in this steel. Martensite can be identified in the image as the more angular feature. The material does not display deformation of the grains in any direction. Since the plate were hot rolled, recrystallization might be the reason for the similar shape of the grains. However, texture might persist. Other techniques such as X-Ray Diffraction (XRD), Electron Backscatter Diffraction (EBDS) might be able to portray it.

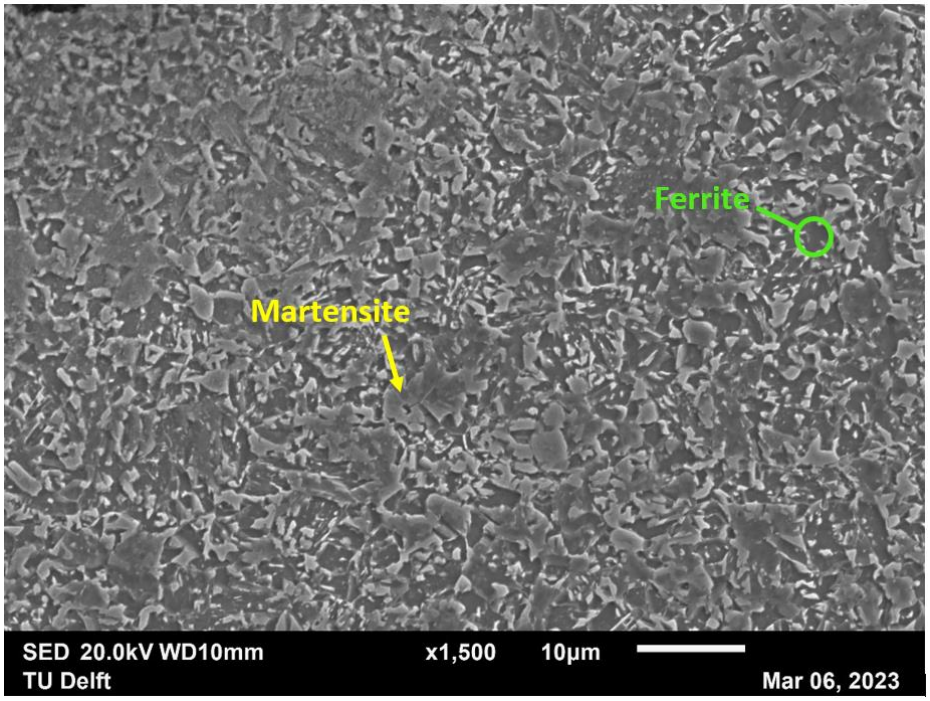

Figure 24 SEM image of DP1000 microstructure.

3.1.3 Mechanical properties characterization

Mechanical properties of the DP 1000 were characterized through tensile testing using a Zwick Z100 universal tensile tester. Tensile test samples were cut using EDM (Electrical Discharge Machining). This technique is one of the methods with the smallest impact on the surface finish and therefore the least impact in hydrogen embrittlement results. Tests were conducted in air with the objective to characterize Ultimate Tensile Strength (UTS), and elongation to fracture (ε_f). In addition, these results will function as a baseline for the results obtained later under the hydrogen environment. Results can be found in Table 6.

Table 6 Mechanical properties DP1000 base material

Tensile Strength (MPa)	Elongation to fracture (%)	Hardness (HV1)
1013.1 ± 25.2	10.5 ± 0.8	328 ± 3

3.2 Experimental methods for hydrogen testing

This section is dedicated to presenting the different aspects required to perform the experiments. Therefore, this section deals with the set-up, the specimen geometry, test matrix and the procedure followed.

3.2.1 Set-up

The set-up was built in-house with the objective to test in-situ, combining tensile testing with hydrogen charging. Tensile testing was done with Zwick Z100 universal tensile tester.

The set- up consists of a tank of 7 liters made of PMMA and sealed with silicone to avoid leaks. A bucket was also installed at the bottom for safety reasons. For practicality, the tank could be raised and lowered, held by two different O-rings. To supply the current for hydrogen charging, a potentiostat Bio-Logic VSP300 with a maximum power of 650 W was employed. The working electrode was connected to the sample (cathode), and the counter electrode to a platinum mesh (anode). In addition, a submersible extensometer (Epsilon 4030) was necessary to record the deformation in the sample while being submerged in the bath. It was calibrated with Epsilon Digital Calibrator model 3590. An image of the setup can be found in Figure 25.

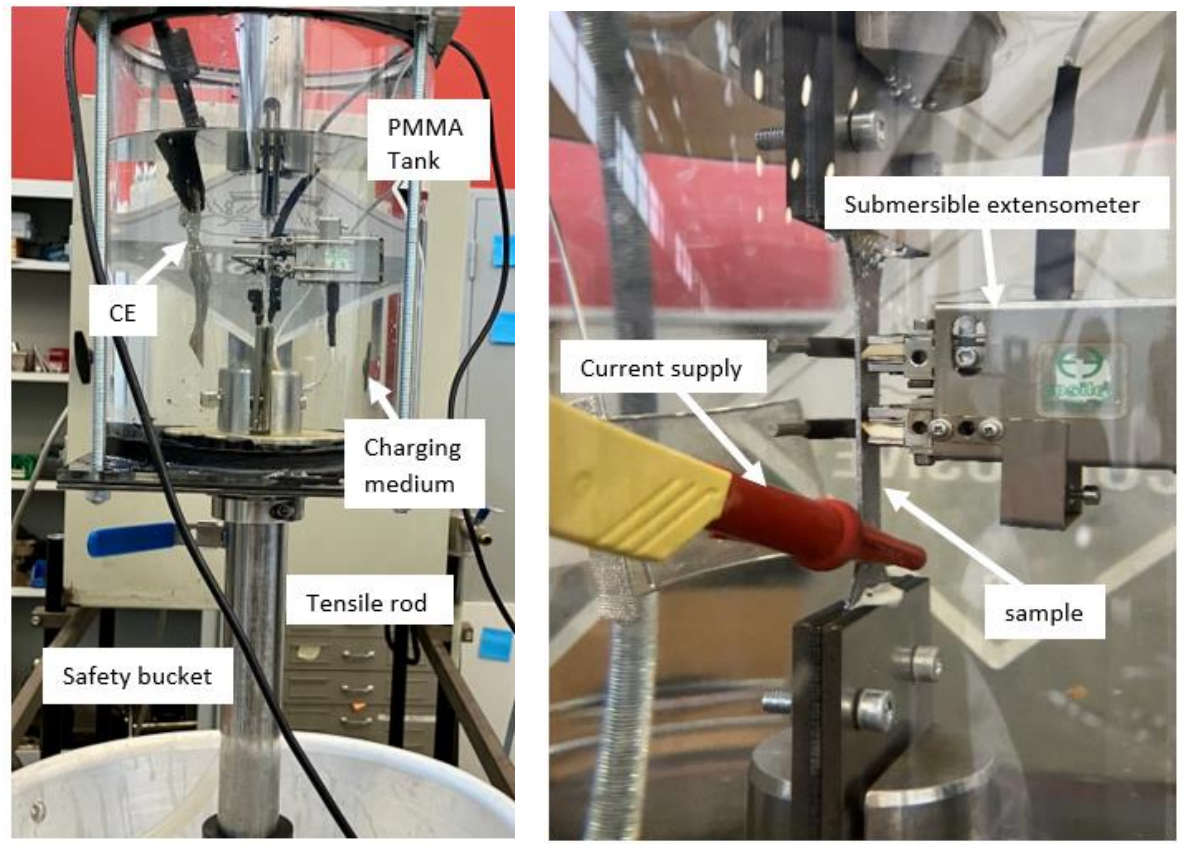

Figure 25 image of the setup: a) visualization of the complete setup b) close up of the inside of the tank.

As an additional equipment, a freezer (Stirling Ultracold: ULT25NEU) was used to store the tested specimens at -86ºC, to avoid hydrogen desorption and accommodate testing time.

3.2.2 Specimen Design and Sample preparation

A schematic of the sample is presented in the below Figure 26. Metal plates of 130 mm x 20 mm x 1 mm were cut from the as-received sheet metal. Samples were sent to be cut in the dog bone shape through EDM as aforementioned.

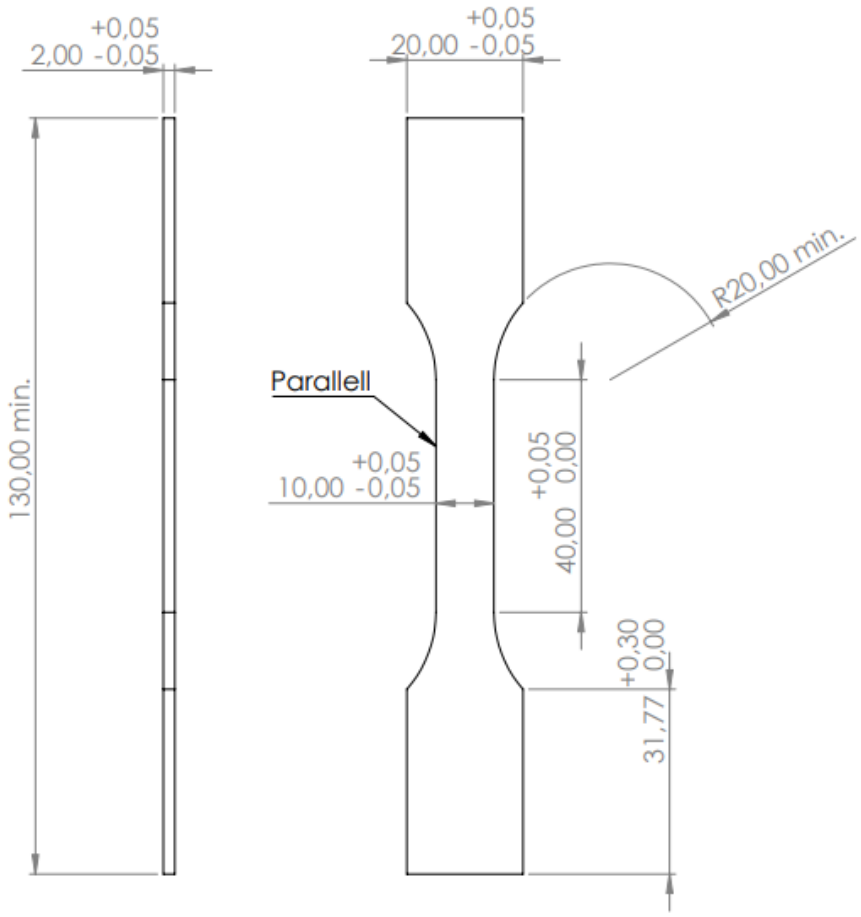

Figure 26 Schematic of final sample design. Dimensions are in mm.

Afterwards, samples were dezinced. Specimens were submerged in a solution of 100 ml of 37% HCl mixed with 100 ml of demi-water. Then samples were sunken in 200 ml of demi-water mixed with NaOH (4g/L). Samples were rinsed with demi-water in between and at the end of the process.

As a requirement, samples needed to be insulated from the rest of the tensile test machine. This specification was demanded for two reasons. The first one, was to protect tensile test machine to conduct current and therefore to suffer from hydrogen embrittlement. The second one, was to ensure the amount of current applied only affected the area of interest (a constant section) The option selected to ensure these conditions were fulfilled was glue. Samples were glued to two metal slabs with respective hole for the tensile test pins.

The sample preparation method was modified several times until the final version was achieved. The final version corrected for the tolerance of the misfit of the slabs with brass aligners. This was done with the purpose of dividing the load equally between both slabs. The amount of glue

was controlled using tape on the edges of the samples. To avoid slipping, spacers of 1.5 mm were given the close shape of the sample and used bolts to be held. Samples were mounted and glued with ES 579 epoxy glue. Specimens were placed in the oven at 150 ºC for one hour for the glue to cure. This version was the one used in the experiments of this thesis (Figure 27). Nevertheless, samples were unable to hold while charging during 2 h as it will be explained in section 3.2.3

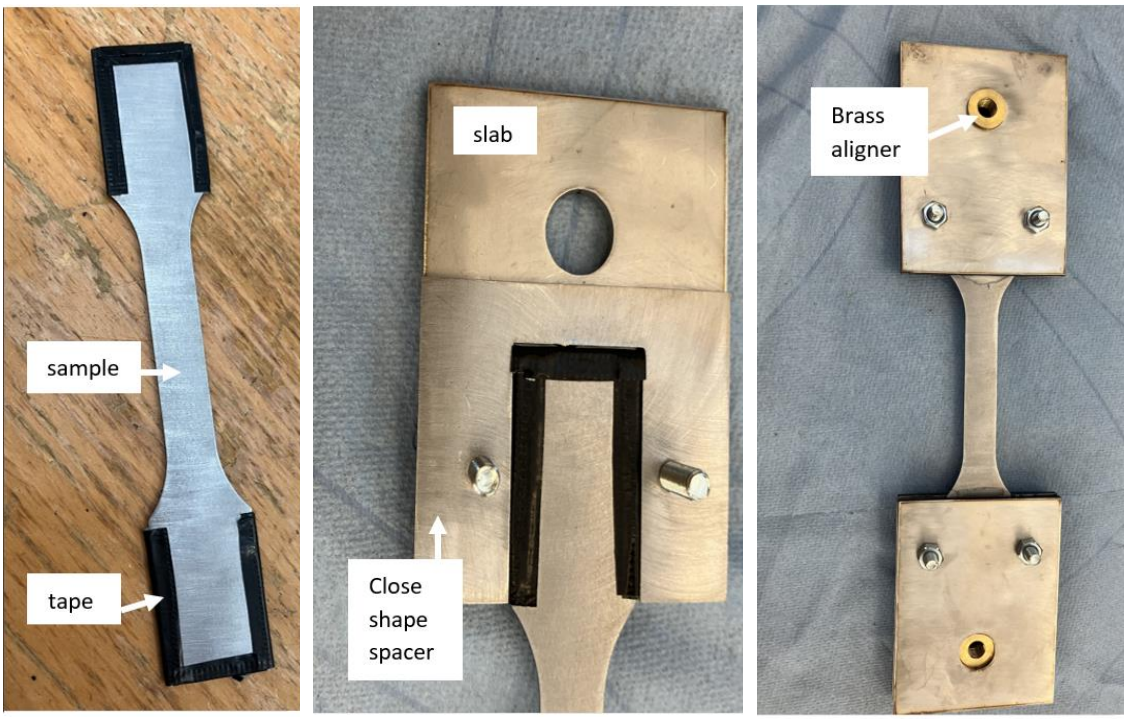

(a) (b) (c)

Figure 27 Successful sample preparation method (a) sample recovered to adjust glue amount b) sample placed inside the spacer c) sample fully mounted.

All samples were sanded with Proxxon Lu-6868 Wecker with Corundum sanding disc at 150 grit. After they were cleaned with isopropanol in the ultrasonic bath Branson 5510.

3.2.3 Process

The test procedure can be divided into the two main experiments performed: tensile test and TDS. This section details the steps followed to carry the test as well as the reason behind the decisions taken for the different approaches.

The tensile test procedure can be split into four subtypes of procedures depending on the pre-strain applied and its type of environment. In all cases an extensometer with a gauge length of 1 inch (25.4cm) was placed on the sample before the test started. The extensometer was not removed during the test since it was not possible within the tank. Extensometer calibration was done previous to the tests. All samples were placed in the tensile test machine and preloaded to 250 N.

Samples with 0% pre-strain in air were tested without being connected to the current. The DP1000 specimens were deformed at slow strain rate (SSR) 14.4 mm/h (10^{-4} s^{-1}). This was done to be consisted with the conditions of samples submerged in the bath.

The remaining sets were tested inside the solution. A solution of Na_2SO_4 0.5 M with Ammonium thiocyanate (3g/L) was used for to provide an electrolyte with neutral pH and a high conductivity. Samples were connected to the potentiostat. Afterwards, the bath was raised, and the counter electrode was connected to the platinum electrode. Current applied was 1mA/cm^2. Samples were tested at 14.4 mm/h. This value was selected through literature [49]. SSRT was selected since it allows to hydrogen to diffuse into the material. Samples were tested until failure.

For the test of the samples pre-strained to 0.5% and 2%, the tensile test can be divided into three phases (Figure 28):

1) **SSRT** of 14.4 mm/h until reaching the 0.5% and 2% plastic pre-strain. For in-situ pre-strain this phase was done while charging. Charging time (15 min or 60 min) starts counting for these samples. For ex-situ, the pre-strain value is reached without charging.

2) **Holding time**. For in-situ pre-strained samples the hold time lasted for the remain time until 15 min or 60 was completed. For ex-situ pre-strained samples, the holding time start counting from this phase onwards. The reason behind was to eliminate time factor between ex-situ and in-situ conditions since both sets will be charged during the same amount of time.

3) **Conventional strain rate**. All samples after reaching the desired time were tested in-situ until failure at 3min/mm strain rate. A faster strain rate was applied to ensure no further diffusion of hydrogen. This was done with purposed of being able to differentiate this case from the samples tested at 0% pre-strain inside the bath.

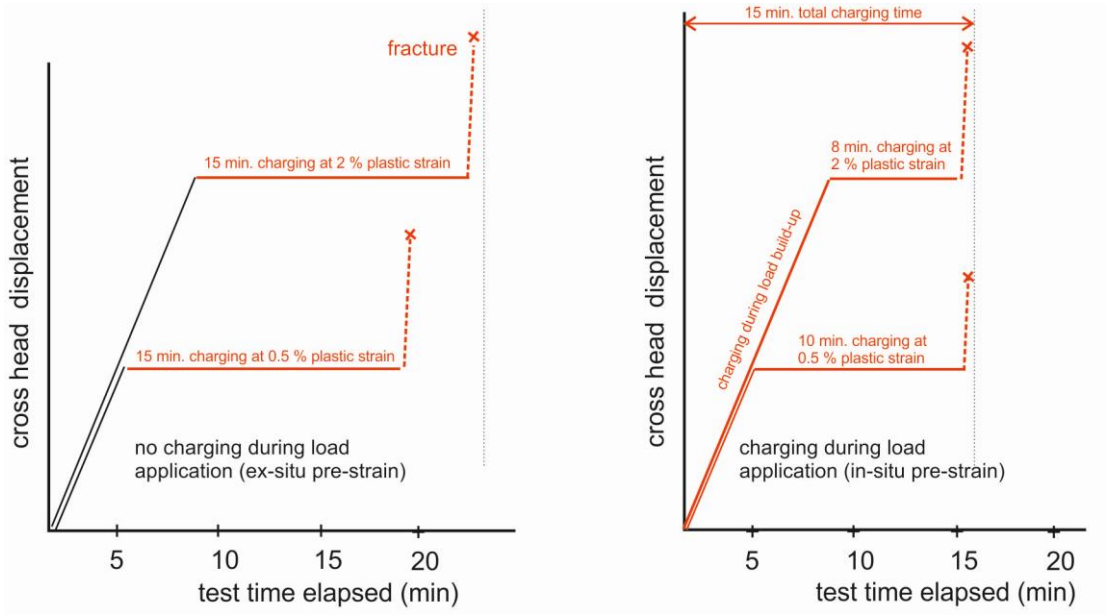

Figure 28 Schematic representation of the different phases of tensile test for 15 minutes charging divided into ex-situ and in-situ pre-straining.

Values of pre-strain were chosen firstly through literature [49] and afterwards adapted through experimental results. Literature focuses on plastic pre-strained values [43] [49] , therefore 0.5% and 2% are chosen as the plastic strain values. However, if we take into account the elastic deformation, the total amount of strain is 0.9% and 2.4%. These total strain values were required by the tensile test software to perform the measurements. However, an additional conversion from strain to volts was needed since the submersible extensometer records the strain signal in volts. 0.5% plastic strain corresponded with 0.201V and 2% plastic strain corresponds with 0.539V. Conversion was done through equation obtained from extensometer calibration.

After the tensile test samples were rinsed with distilled water and dried with pressurized air. Immediately afterwards they were stored in the freezer at -86 °C to avoid hydrogen loss. Samples were separated from the slabs for TDS test.

All samples charged with hydrogen were tested in the TDS to measure diffusible hydrogen content. They were tested during 10 minutes at an isothermal program at 300ºC.This temperature was selected since desorption of diffusible hydrogen present in reversible traps such as dislocations, occurs before reaching 300ºC [8] [50]. No ramping was done to avoid early on hydrogen desorption. Samples were inserted while the test is running make sure all hydrogen is measured. The TDS instrument was calibrated, and filters changed before running experiments. Samples are weighted at the end of the test.

3.2.4 Matrix

The effect of pre-strain as well as the environment in which this condition occurs might influence hydrogen embrittlement. Therefore, different values of pre-strain and ex-situ and in-situ pre-strain conditions were investigated. Pre-strain is defined as the deformation previous to the

test measured over a constant initial area. The test matrix is presented in Table 7. It contains the tests performed, the number of tests performed per condition, the environment in which pre-strain was performed and the goal of each of the tests.

The matrix is divided into four sets of samples. The sets of samples are subdivided according to the amount of pre-strain and the pre-strain environment applied to them. It is also mentioned if Thermal Desorption spectroscopy (TDS) test was performed to the set.

Table 7 Test matrix

SET	Tensile test Parameters	Environment of the pre-straining	TDS	Charging time	Goal
A	0% pre-strain	Air	Yes	Until failure	Obtain a baseline for mechanical properties
		Hydrogen (H) solution		Until failure (~11 min)	Characterize material behavior and H uptake under HE without pre-strain
B	0.5% pre-strain	H ex-situ H in-situ		15 min	Compare mechanical properties and H uptake between in-situ and ex-situ pre-strain and pre-strain itself
C1	2% pre-strain	H ex-situ H in-situ		15 min	Compare mechanical properties and H uptake between in-situ and ex-situ pre-strain and pre-strain itself.
C2		H ex-situ H in-situ		60 min	Observe the effect of longer charging times.

** A minimum of 3 samples per test condition were tested*

Set A consisted of samples that were tested until failure, in air and inside the bath without being pre-strained. For the specimens tested inside the solution, hydrogen charging time duration equaled test duration. This parameter depended on each experiment though the average duration was 11 minutes. Both subsets of samples were tested at a strain rate 14.4 mm/h (as literature suggested [49]) and analyzed in the TDS. The objective of this set was to characterize the DP1000 steel properties without the effect of pre-strain with and without hydrogen

influence. In this way a baseline is obtained, making possible to benchmark results obtained with hydrogen charging.

Set B tests were performed with 0.5% of plastic pre-strain inside the bath. This set is divided into two groups of samples. In the first one, samples are charged while pre-strained, which is called in-situ pre-straining. In the second one (ex-situ), plastic pre-strain value 0.5% was achieved without charging. It was followed by a holding time in which sample is charged. In both scenarios, samples are hydrogen charged for 15 minutes. All samples were tested for hydrogen content. The objective of this set was to observe if pre-strain has an effect on mechanical properties and hydrogen uptake. Moreover, differences between in-situ and ex-situ pre-strain conditions were investigated.

Set C tests were performed with 2% of plastic pre-strain inside the bath. This set is divided into four groups of samples depending on the pre-strain environment and the charging time. The same definitions for ex-situ and in-situ apply for this set as for set B. The difference withing the subsets for this case, relies on whether the samples were charged with hydrogen for 60 min or 15 min. The goal of this set was to observe the influence of pre-strain in hydrogen embrittlement while comparing conditions of pre-charging ex-situ and in-situ on the mechanical properties and H uptake. In addition, in this set has the goal was to observe the effect of charging duration.

Furthermore, the final objective was to be able to benchmark and compare the results among the sets. This will allow to extract conclusions by comparing different levels of pre-strain in different environments.

4. RESULTS AND DISCUSSION

This section provides an overview of the results obtained while critically analyzing them. This chapter is divided in three sections according to the factors studied. The first one is dedicated to presenting and discussing the effect of pre-strain. The following section is devoted to analyzing the difference in the outcome between in-situ and ex-situ testing. These two sections will be followed by a last one that analyzes the effect of the charging time in the experiments. The final section is dedicated to fractography analysis.

4.1 Effect of pre-strain level

One of the main goals of this work is to determine the possible effect of pre-strain in hydrogen embrittlement. Therefore, results of the average strain at failure (crosshead and extensometer results) and hydrogen uptake are displayed in Table 8 . The engineering Stress -Strain curves for all the set are shown in Appendix A. Nevertheless, to facilitate the visualization of the results bar plots are displayed to accompany the overview table (Figure 29 and Figure 30).

Table 8 Overview of strain to failure and H content.

SET	Tensile test Parameters	Environment of the pre-straining	Charging time	Average strain at failure, % (crosshead)	Average strain at failure, % (extensometer)	H content, (ppm)
A	0% pre-strain	Air	Until failure	13.2 ± 0.9	10.5 ± 0.8	0.01 ± 0.01
		H solution	Until failure (~11 min)	6.5 ± 0.5	4.6 ± 1.9	0.42 ± 0.02
B	0.5% pre-strain	H ex-situ	15 min	9.3 ± 0.6	5.5 ± 0.6	0.46 ± 0.04
		H in-situ		9.4 ± 0.7	5.9 ± 1.1	0.50 ± 0.10
C1	2% pre-strain	H ex-situ		9.7 ± 0.6	5.4 ± 0.5	0.62 ± 0.13
		H in-situ		8.4 ± 0.2	6.3 ± 1.8	0.55 ± 0.03

Results of the 0.5% pre-strained and 2% pre-strained samples are compared, with each other as well as with respect to the baseline (0% pre-strain). With that purpose the variable of environment of the pre-straining (ex-situ and in-situ) will be fixed. Results derived from samples tested for 60 minutes will be analyzed in a separate section.

Hydrogen embrittlement is translated in a 56% reduction of strain at failure (equation 11) when comparing both A subsets. Taking this data as a reference it can be stated that low levels of pre-strain have a high impact in elongation at fracture for DP1000. 0.5 % plastic pre-strain implies a 48% reduction in elongation at failure ex-situ and 44% in-situ. 2% plastic pre-strain implies a 40% reduction in elongation at failure ex-situ and 51% in-situ in average.

$$\text{Reduction of strain at failure } = \left(1 - \left(\frac{\varepsilon_f B}{\varepsilon_f A}\right)\right) * 100 \quad (11)$$

For samples pre-strained ex-situ, average strain at failure is 5.5 ± 0.6 (extensometer) for set B. For set C1, average strain at failure is 6.3 ± 1.8 (extensometer). Hydrogen content is 0.46 ± 0.04 ppm and 0.62 ± 0.13 ppm respectively. Contrary to what was expected, elongation to fracture does not diminish as a result of the 26% increase in hydrogen uptake. This could be due to the conventional strain rate applied at the end of the test which prevents hydrogen diffusion [29]. In other words, hydrogen diffusion due to the stress at conventional strain rate, can be neglected.

For samples pre-strained in-situ, average strain at failure is 8.4 ± 0.2% (extensometer) for set B. For set C1, average strain at failure is 5.4 ± 0.9 (extensometer). Hydrogen contents are 0.50 ± 0.10 ppm and 0.55 ± 0.03 ppm respectively. Contrary to the previous case, it shows a 9% average reduction in elongation at fracture for a 9% increment of hydrogen uptake. To further investigate the difference between ex-situ and in-situ and to extract conclusions, 60 min hydrogen testing was performed only for 2% pre-straining. It might be expected that the effect of pre-straining will become more noticeable for longer charging time.

Drexler et. al. showed as well as decreased of a 93 % in strain at fracture for DP1000 at 0% pre-strain [49]. Though strain rate and current applied was the same as the one used in this work, there are some differences in their method. Samples were pre-charged for 2h instead and the medium utilized was H2SO4 electrolyte containing 1 g/L Thiourea. This can be the cause of a higher hydrogen uptake and diffusion through the sample compared to the approximately 50% reduction obtained in this work.

According to literature, pre-strain increases trap density [43] [49] [50] [51]. In specific reversible hydrogen traps such as dislocations. Consequently, researchers observed an increase in hydrogen uptake and sub-surface hydrogen concentration. This supports results obtained. It can be seen that there is an increasing trend in hydrogen content when increasing pre-strain level. Nevertheless, researchers also point out a decrease in diffusivity coefficient [43] [50]. On the other hand, Zafra et. al. remarked the effect of reversable trapping and therefore diffusible

hydrogen as the main cause of hydrogen embrittlement [52]. Weiguo et. al. supported this statement [51]. Higher pre-strain should enhance hydrogen embrittlement effect due to the increase in reversible trapping. Indeed, with the results acquired it is visible that pre-stain enhances hydrogen embrittlement. Nevertheless, strain at failure is barely modified between 0.5% and 2% pre-strain. This could be due to the decreasing diffusivity as pre-strain increases. As well, it could be due to the short charging time and therefore diffusion time (15 min) of these tests.

In summary, it can be said that both pre-strain levels considerably affect elongation at fracture. However, the effect of incrementing pre-strain level from 0.5 % to 2 % has a minimal effect on DP100 for 15 minutes of charging.

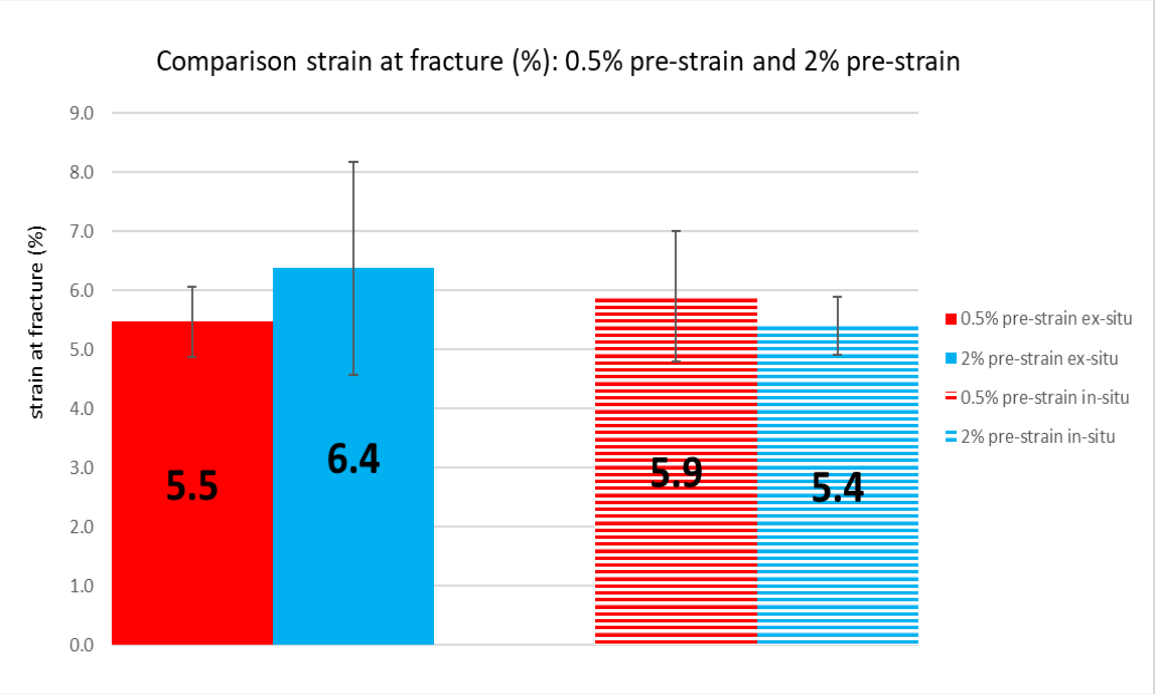

Figure 29 Bar plot comparing strain at fracture results between 0.5% and 2% plastic pre-strained samples.

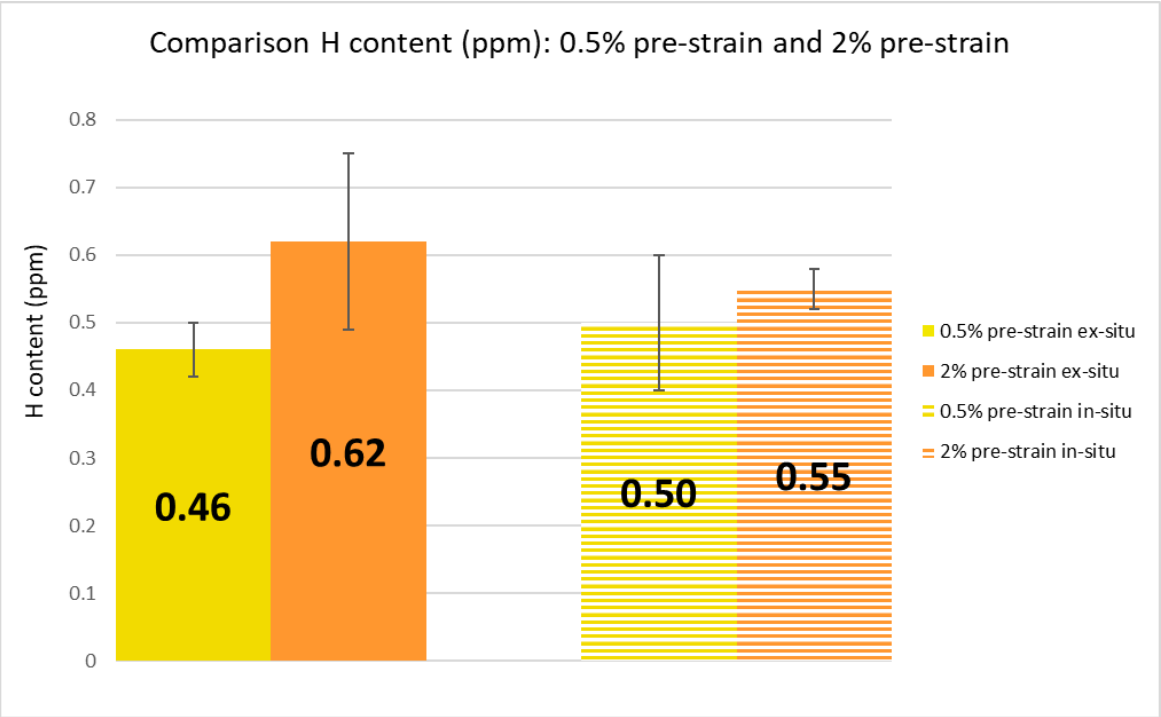

Figure 30 Bar plot comparing hydrogen content results between 0.5% and 2% plastic pre-strained samples.

4.2 Effect of pre-straining environment

The second goal of this work was to explore the research gap of in-situ pre-straining. In this section the ex-situ and in-situ testing are compared for the different pre-strain percentages and charging times. Therefore, results of the average strain at failure (crosshead and extensometer results) and hydrogen uptake are displayed in Figure 31 and Figure 32.

Table 9 Overview of strain to failure and H content.

SET	Tensile test Parameters	Environment of the pre-straining	Average strain at failure % (crosshead)	Average strain at failure % (extensometer)	Charging time	H content (ppm)
B	0.5% pre-strain	H ex-situ	9.3 ± 0.6	5.5 ± 0.6	15 min	0.46 ±0.04
		H in-situ	9.4 ± 0.7	5.9 ± 1.1		0.50 ±0.10
C1	2% pre-strain	H ex-situ	9.7 ± 0.6	6.4 ± 1.8	15 min	0.62 ±0.13
		H in-situ	8.4 ± 0.2	5.4 ± 0.5		0.55 ±0.03
C2		H ex-situ	9.3 ± 1.1	6.7 ± 1.0	60 min	1.06 ±0.19
		H in-situ	8.3 ± 1.1	5.1 ± 1.2		1.28 ±0.18

For samples of set B, average elongation at failure for ex-situ pre-strain is 5.5 ± 0.6% (extensometer). For in-situ, plastic pre-strain average strain at failure is 5.9 ± 1.1% (extensometer). Hydrogen contents are 0.46 ± 0.04 ppm and 0.50 ± 0.10 ppm respectively. In this scenario, there is almost no difference between both environments especially if results are taken from the crosshead. Difference in hydrogen uptake is also minimal: an 8% average.

For samples of set C1 (charged for 15 minutes), average elongation at failure for ex-situ pre-strain is 6.3 ± 1.8 % (extensometer). For in-situ plastic pre-strained samples, average strain at failure is 5.4 ± 0.5% (extensometer). Hydrogen content is 0.62 ± 0.13 ppm and 0.55 ± 0.03 ppm respectively. For this case, a reduction of an average of 14% in elongation at failure can be observed. Hydrogen uptake presents a high scatter for ex-situ value. Therefore, no conclusions can be stated. The difference becomes pronounced when the charging time is increased from 15 to 60 minutes for the 2% plastic pre-strained samples.

For samples of set C2 (charged for 60 minutes), average elongation at failure for ex-situ pre-strain is 6.7 ± 1.0% (extensometer). For in-situ plastic pre-strain, average strain at failure is 5.1 ± 1.2% (extensometer). Hydrogen content is 1.06 ± 0.1 ppm and 1.28 ± 0.18 ppm respectively. Incrementing charging time indeed accentuated differences between both charging methods. It implies a reduction of 24% average (measured from extensometer results) in strain at failure for in-situ samples compared to ex-situ samples. An increase of 17% in hydrogen is also observed for these samples.

Therefore, it can be alleged that a difference among in-situ and ex-situ charging is only visible for higher pre-strain levels and longer charging time.

As stated in the previous section, hydrogen embrittlement is enhanced by reversable traps that allow hydrogen uptake and diffusion through the material. Dislocations and vacancies can be allocated in this category. These defects arise as a consequence of pre-strain. Nevertheless, this is a feedback mechanism. As it is described by the HESIV model, hydrogen promotes the formation of these defect itself [22]. This model suggests that hydrogen reduces vacancy formation energy. Vacancies tend to form microvoids leading to a decrease in ductile crack resistance. Therefore, straining in-situ in a hydrogen environment is expected to increase the number of defects relative to ex-situ charged samples as well as lower strain at fracture values. This is exemplified for samples pre-strain at 2% for 60 minutes. This set exhibits an increase in hydrogen uptake and hydrogen embrittlement for the in-situ tested samples compared to the ex-situ ones. Simultaneously charging while deforming the material seem to lead to a feedback production of defects due to the introduction of hydrogen in the early stage of plastic strain. As a consequence, it seems that though hydrogen content increases, damage its already aggravated by defects, enhancing hydrogen embrittlement as well. This reinforces the idea that high contents of hydrogen are not necessary to cause hydrogen embrittlement fracture. This can be supported by samples from the SSRT (0% pre-strain H) test, that though they had the lowest hydrogen content they were the most embrittled. In addition, set C2 also is representative of this phenomenon.

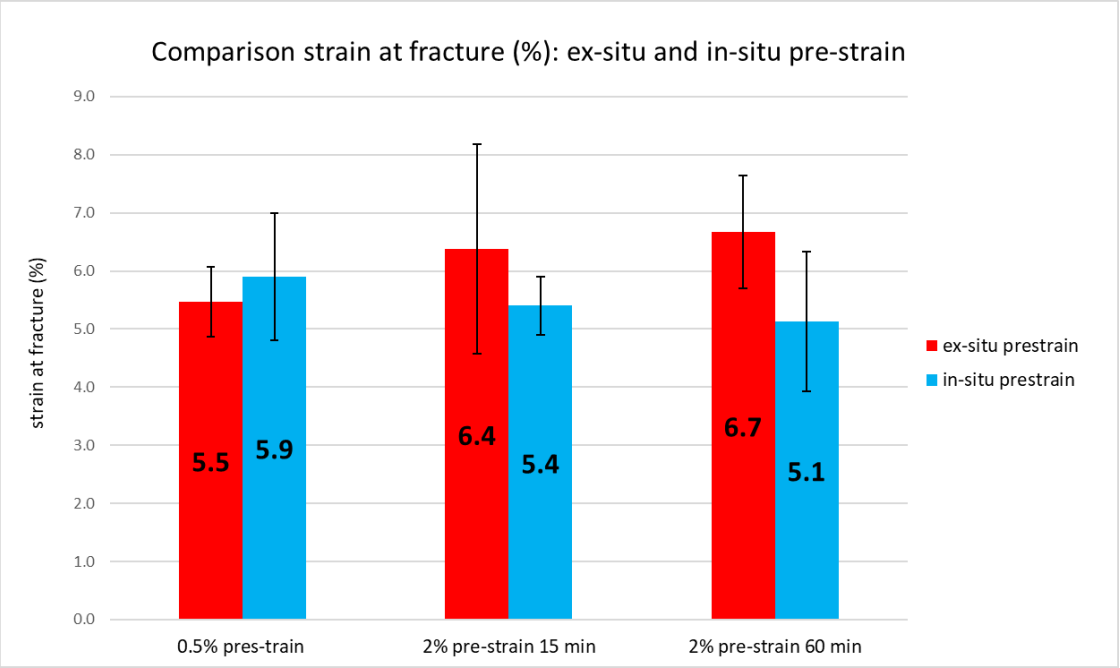

Figure 31 Bar plot comparing strain at fracture results for ex-situ and in-situ pre-strain conditions.

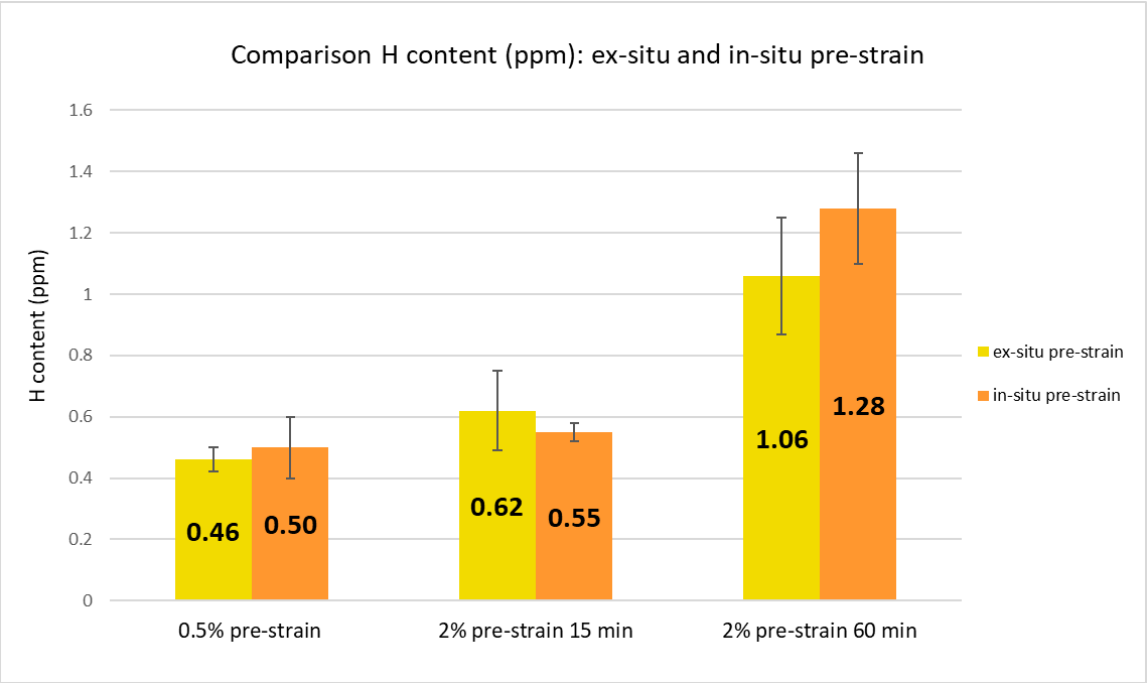

Figure 32 Bar plot comparing hydrogen content results for ex-situ and in-situ pre-strain conditions.

4.3 Effect of charging time

Time was introduced as an extra variable with the objective to enhance the difference in results between ex-situ and in-situ pre-straining. Increasing charging time is expected to increase hydrogen uptake and hydrogen embrittlement. In this thesis 60 minutes charging were only performed at 2% pre-strain. Performing thesis 60 minutes charging at 0.5% plastic pre-strain is desirable to clarify the effect of time for lower pre-strain levels. The results are compiled in Table 10 and portrait in Figure 33 and Figure 34.

Table 10 Overview of strain to failure and H content

SET	Tensile test Parameters	Environment of the pre-straining	Average strain at failure % (crosshead)	Average strain at failure % (extensometer)	Charging time	H content (ppm)
A	0% pre-strain	Air	13.2 ± 0.9	10.5 ± 0.8	Until failure	0.01 ± 0.01
		H solution	6.5 ± 0.5	4.6 ± 1.9	Until failure (~11 min)	0.42 ± 0.02
C1	2% pre-strain	H ex-situ	9.7 ± 0.6	6.4 ± 1.8	15 min	0.62 ±0.13
		H in-situ	8.4 ± 0.2	5.4 ± 0.5		0.55 ±0.03
C2		H ex-situ	9.3 ± 1.1	6.7 ± 1.0	60 min	1.06 ±0.19
		H in-situ	8.3 ± 1.1	5.1 ± 1.2		1.28 ±0.18

For set C1 (15 min), average elongation at failure for ex-situ pre-strain is 6.4± 1.8 % (extensometer). For set C2 (60 min), average elongation at failure for ex-situ pre-strain is 6.7 ± 1.0 % (extensometer). Hydrogen content is 0.62 ± 0.13 ppm and 1.06 ± 0.19 ppm respectively. There is barely any variation between both strain at fracture results. However, hydrogen content incremented an average of 42% when DP1000 is charged during 60 minutes.

For set C1 (15 min), average elongation at failure for in-situ pre-strain is 5.4 ± 0.5 (extensometer). For set C2 (60 min), average strain at failure is 5.1 ± 1.2 % (extensometer). Hydrogen content is 0.55 ± 0.03 ppm and 1.28 ± 0.18 ppm respectively. In this case, elongation at fracture its reduced 6% when samples are charged for 60 min. Hydrogen content is increased by 58% in average.

Moreover, as aforementioned in the difference between pre-strain environments, the difference in strain at fracture for C1 in-situ is 14% while 24% for C2 in-situ. Hydrogen content variation among both methods for C1 is minimum, while it is 17% for C2 in-situ.

In addition, hydrogen diffusivity might be a possible a reasoning for why the difference in results can only be detected at higher times. Since pre-strain seems to decrease diffusion coefficient, longer times might be needed to accentuate the effect of hydrogen presence [43] [50]. Longer times allow higher hydrogen uptake as proven, and combined with the effect of pre-strain, higher defect density. Although a slight increase is observed from 0.5 to 2 % plastic pre-strain after 15 minutes of charging, the absorbed H content is doubled after 1 h of charging. However, this doesn't seem to have the expected impact on hydrogen embrittlement. Reduction in strain at fracture is small compared to the increase in hydrogen content (42% and 58%). This supports

the idea that hydrogen embrittlement is not necessarily enhanced by high contents of hydrogen. 0% pre-strain samples tested inside the bath can be taken as an additional example of this affirmation. It presents one of the smallest elongations at fracture for only 0.42 ± 0.02 ppm hydrogen content.In addition, this underlines the strong role of plastic deformation and or its ¡ combination with longer charging times.

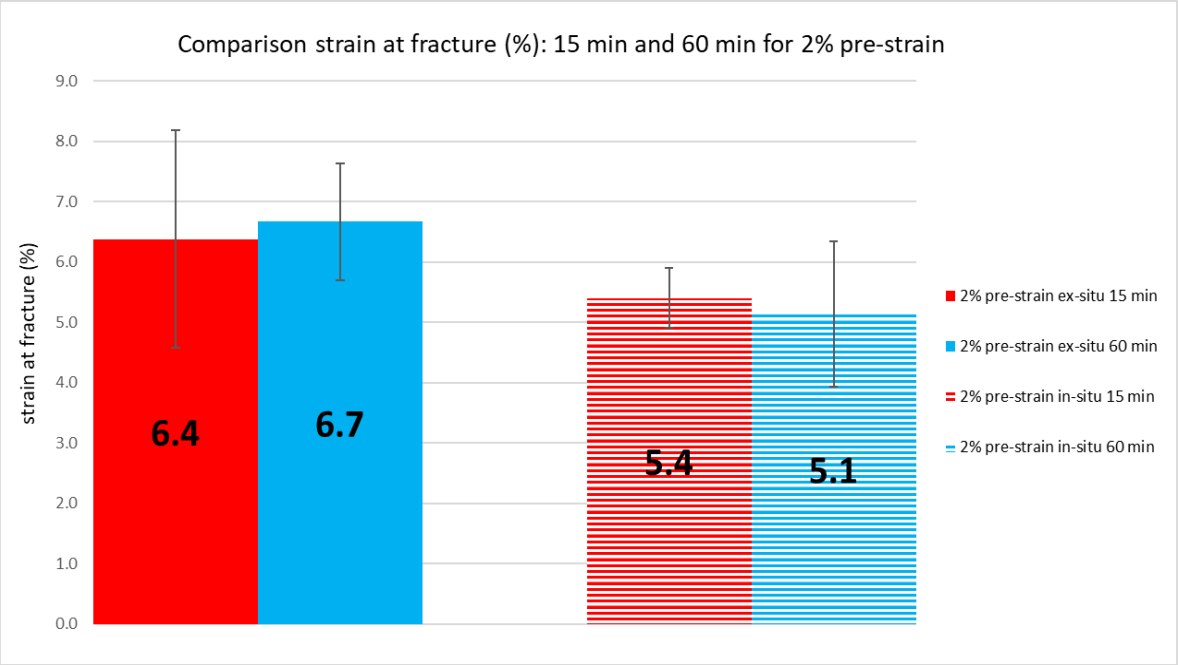

Figure 33 Bar plot comparing strain at fracture results for 15 min and 60 min hydrogen charging at 2% plastically pre-strain.

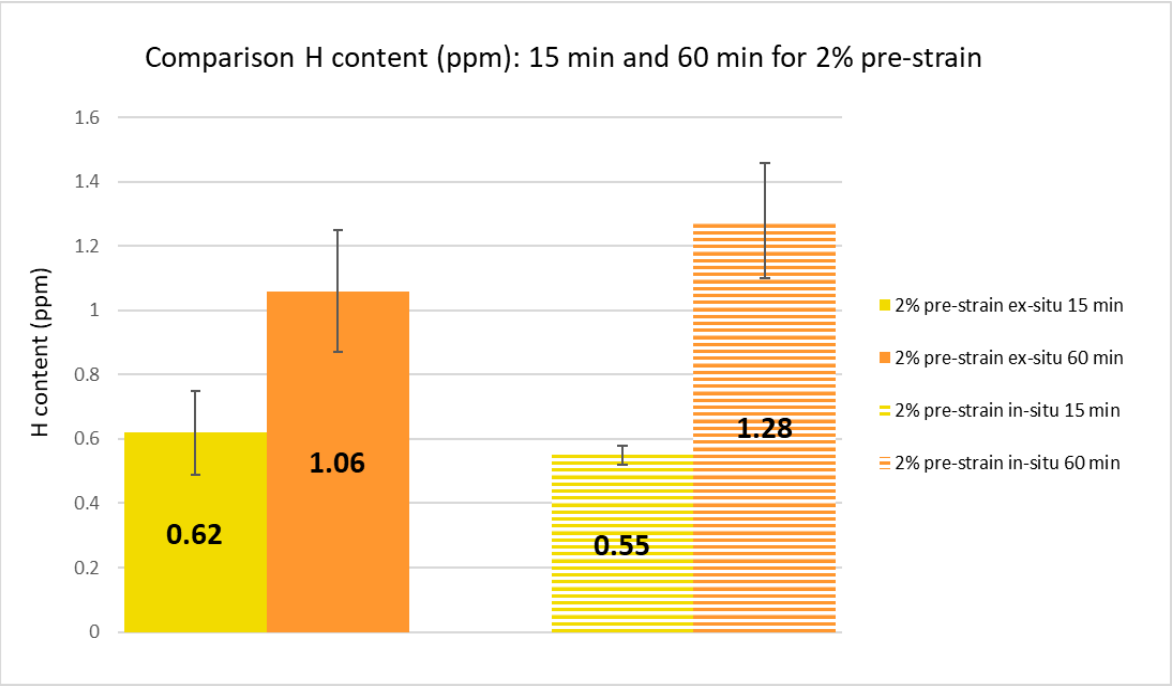

Figure 34 Bar plot comparing hydrogen content results for 15 min and 60 min hydrogen charging at 2% plastically pre-strain.

4.4 Fractography

Fractography analysis was performed in the SEM. Samples were observed after being tested for hydrogen content by TDS. As a consequence, oxidation particles are present in the surface. In some cases, this hinders the fractography observations. No conclusions could be extracted of the hydrogen embrittlement fracture mechanisms. All sets will be discussed focusing on the type of fracture produced due to the different pre-strain, environment and charging time.

Effect of pre-strain

In Figure 35 and Figure 36 images obtained with SEM at different magnifications from samples tested in air are presented. Figure 37 and Figure 38 show images of different areas from samples tested inside the bath (0% pre-strain H). Figure 39 and Figure 40 display images of 0.5 and 2% plastic pre-strain ex-situ samples with the objective to compare the different fracture surfaces.Figure 41 and Figure 42 compare fractography of 0.5 and 2% plastic pre-strain in-situ.

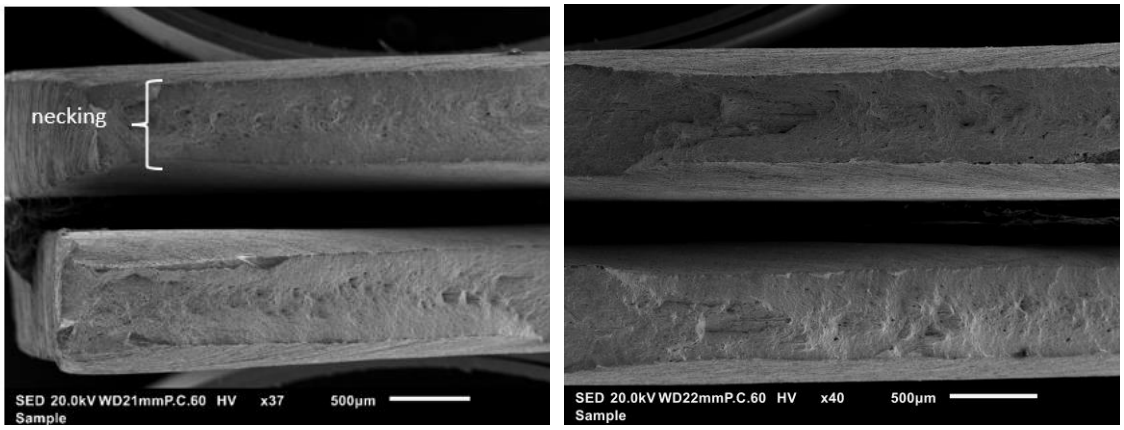

(a) (b)

Figure 35 SEM image of fracture surface of sample of 0% pre-strain H a) a low magnification image of the left width edge b) a low magnification of an area of the middle section.

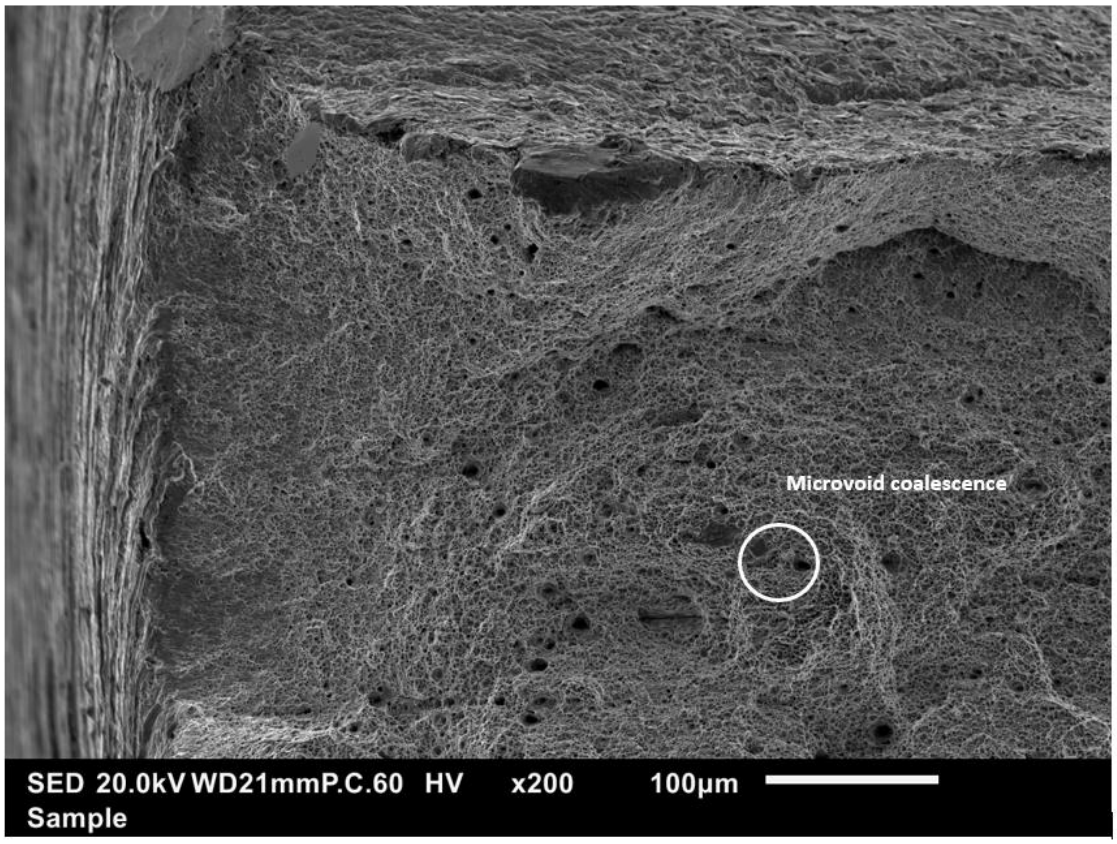

Figure 36 SEM image of fracture surface of sample of 0% pre-strain air.

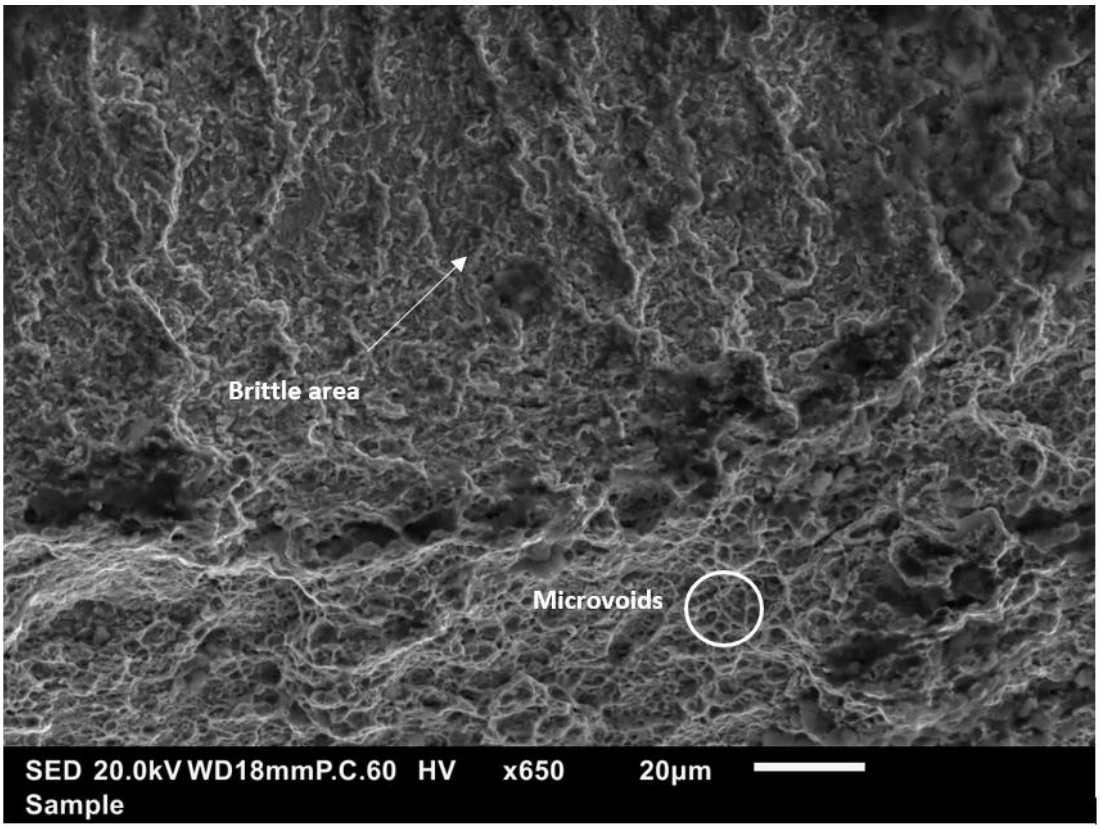

Figure 37 SEM image of fracture surface of right width side of sample of 0% pre-strain H.

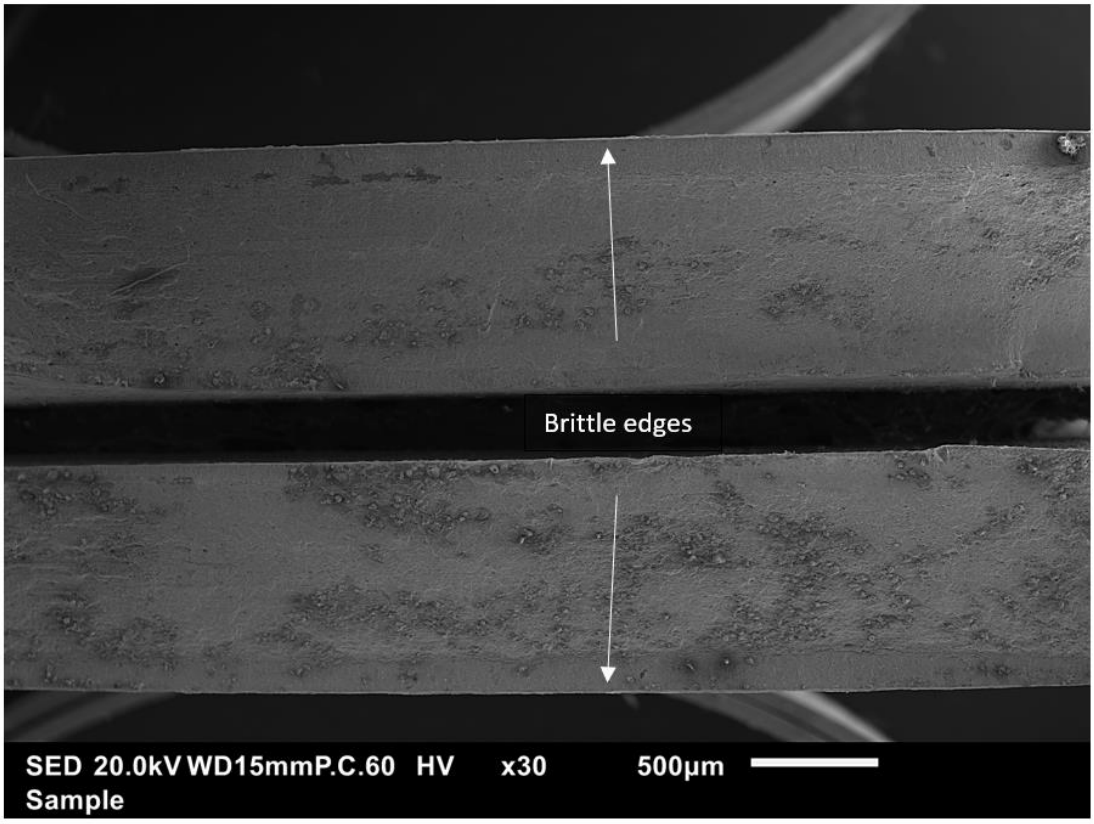

Figure 38 SEM image of fracture surface of the middle section of the sample of 0% pre-strain H.

Figure 35and Figure 36 serve as a reference to compare the effect of hydrogen embrittlement in DP1000. As it can be observed, without the presence of hydrogen this steel behaves as a fully ductile material. It shows necking that can be identified by the reduction in section of the samples (Figure 35). In addition in Figure 36, voids and evidence of microvoid coalescence can be observed. This is characteristic of ductile fracture. This matches results obtained for strain a fracture (10.5 ± 0.8%). The presence of inclusions is not clear since it could be mistaken for oxide particles. Reddy et. al also observed necking and microvoid coalescence for the DP 980 uncharged samples [43]. Ping et.al also observed this feature for uncharged 2205 duplex stainless steel [53].

In Figure 37 one of the edges of the samples can be observed. The intention of this image is to portrait the brittle edge around the corner. It can be perceived that while the center of the sample seems to be ductile, the corners present characteristic of a brittle fracture. This feature was not present for the sample tested in air that was fully ductile. Figure 38 presents the middle section of the sample. It can be observed that the brittle fracture persists along one of the edges of the specimen. However, the central area seems to be fractured in a ductile manner. This matches fractography images obtained by Ping et.al [53]. Samples at 0% pre-strain charged with hydrogen showed dimples in the center while displaying quasi-cleavage on the edges. This supports the reduction in strain at fracture a (56%) at failure observed in the mechanical properties and the influence of hydrogen in the fracture mode.

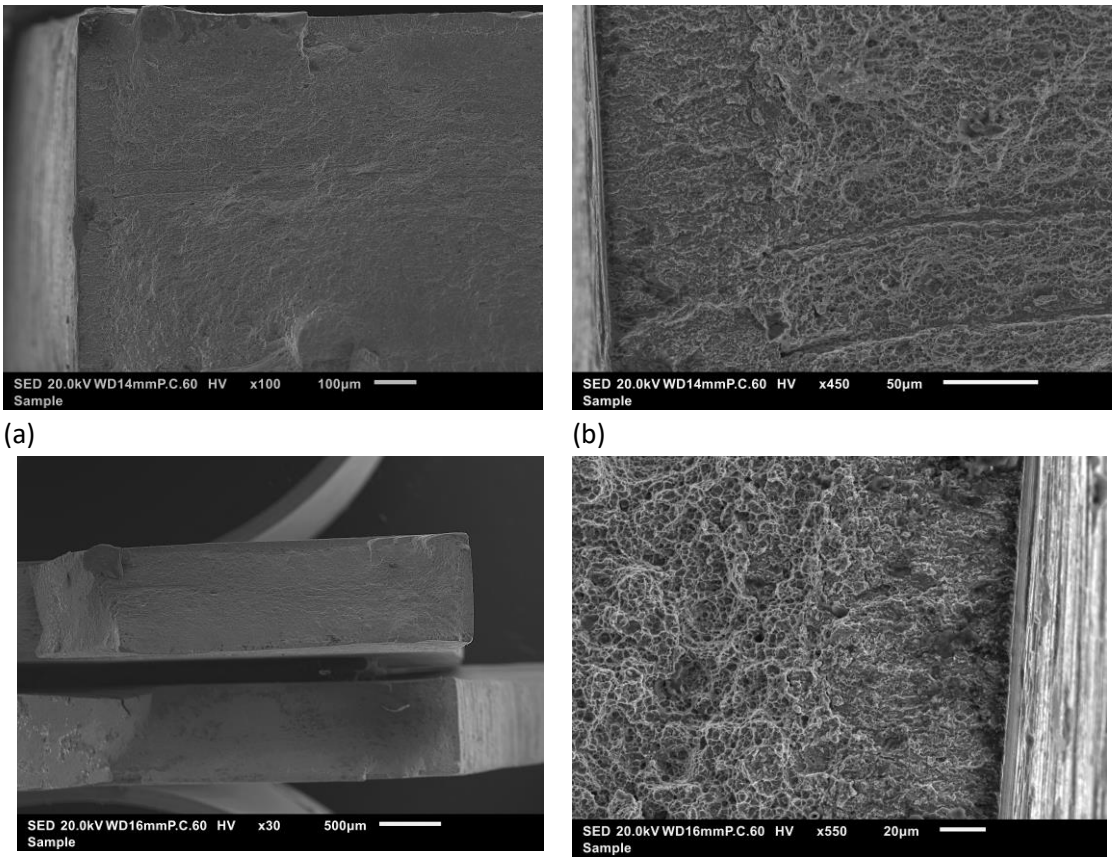

Figure 39 SEM image of fracture surface of a) sample 0.5% pre-strain ex -situ at low magnification of the left width edge of the sample b) a magnified view of previous image c) sample 2% pre-strain ex -situ at low magnification of the right width edge of the sample d) a magnified view of previous image.

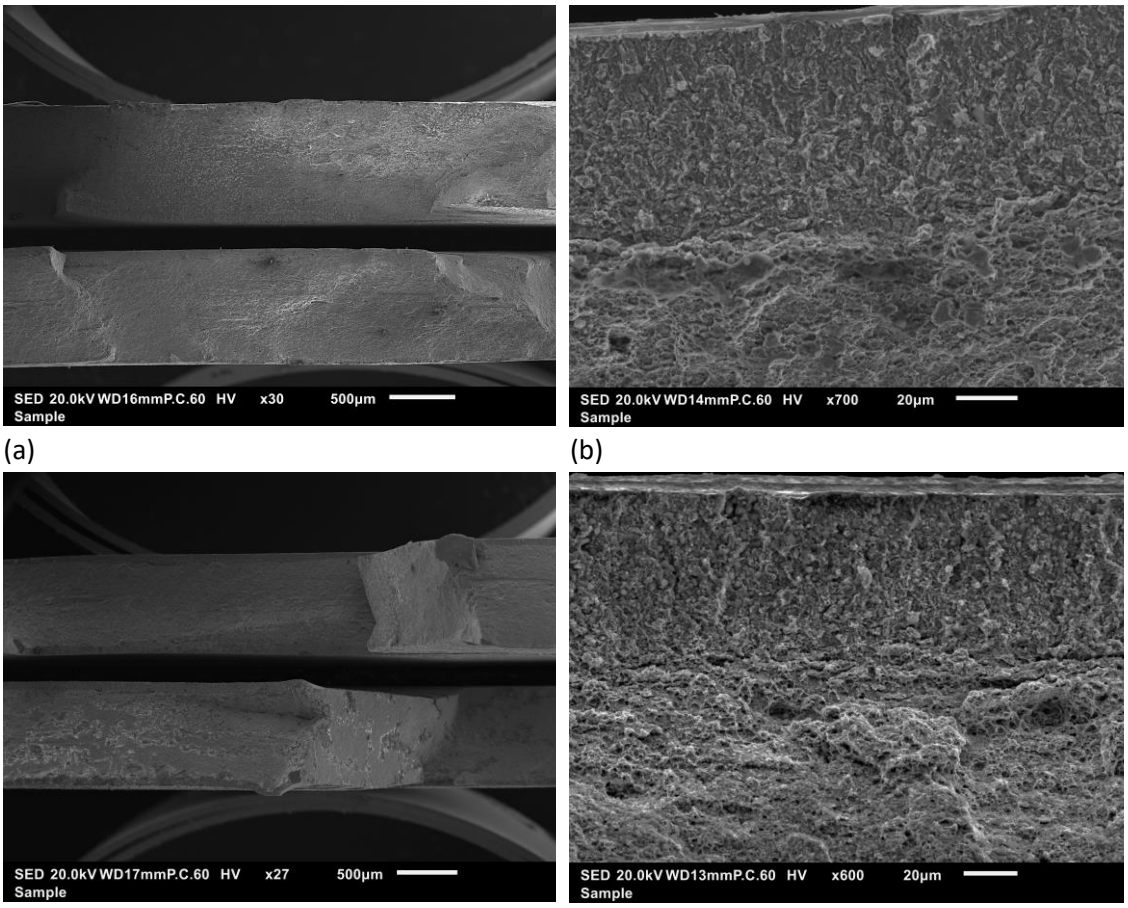

Figure 40 SEM image of fracture surface of a) sample 0.5% pre-strain ex -situ a low magnification of an area of the middle section b) a magnified view of previous image c) sample 2% pre-strain ex -situ a low magnification of an area of the middle section d) a magnified view of previous image

Figure 39 (a and b) show the corner of the sample. A brittle area while the inner side seems to remain presenting ductile characteristic such as voids and dimples can be observed. Similar features are displayed for samples of set A tested inside the bath. For only 0.5% ex-situ pre-strain, samples already exhibit brittle characteristic. In Figure 39 (c and d) for 2% ex-situ pre-strain, width edges present a brittle area surrounding them while the inner side seems to remain presenting ductile characteristic such as dimples. The reappearance of this marked brittles edges also matches the 26 % increase in hydrogen uptake and the small decrease in strain at fracture when contrasted with the 0.5% pre-strain.

Figure 40 is dedicated to illustrating the middle section of the samples. For 0.5% pre-strain ex-situ Figure 40 (a and b), a brittle area persists along the side of the specimen (as the sample with 0% pre-strained tested inside the bath). However, in the central area, brittle length edges seem to be less marked when compared with 2% plastic pre-strain ex-situ (Figure 40 (c and d)). It can be observed that in this case, both edges are embrittled and not only one. This supports results obtained for hydrogen content and mechanical properties. A higher hydrogen content (26%) due to a higher level of pre-strain seems to accentuate brittle characteristics of the fracture.

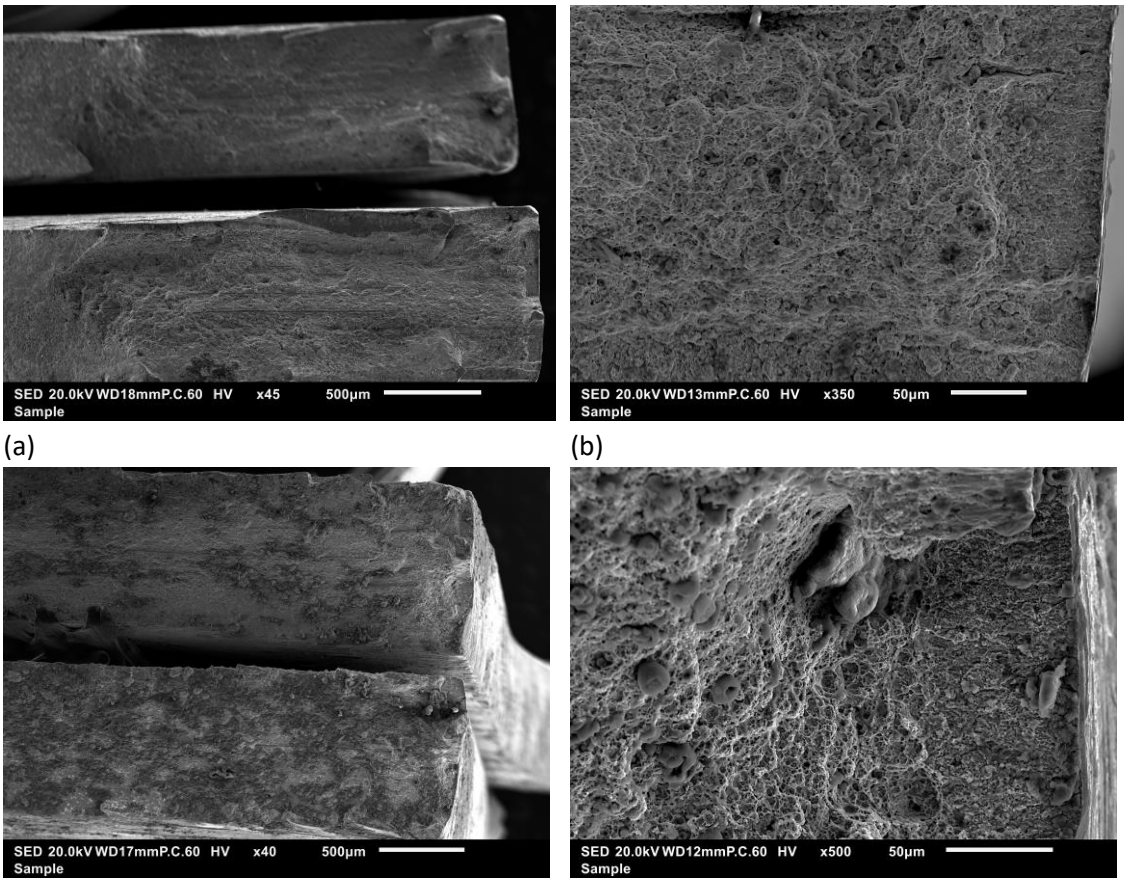

Figure 41 SEM image of fracture surface of a) sample 0.5% pre-strain in -situ at low magnification of the right width edge of the sample b) a magnified view of previous image c) sample 2% pre-strain in -situ at low magnification of the right width edge of the sample d) a magnified view of previous image

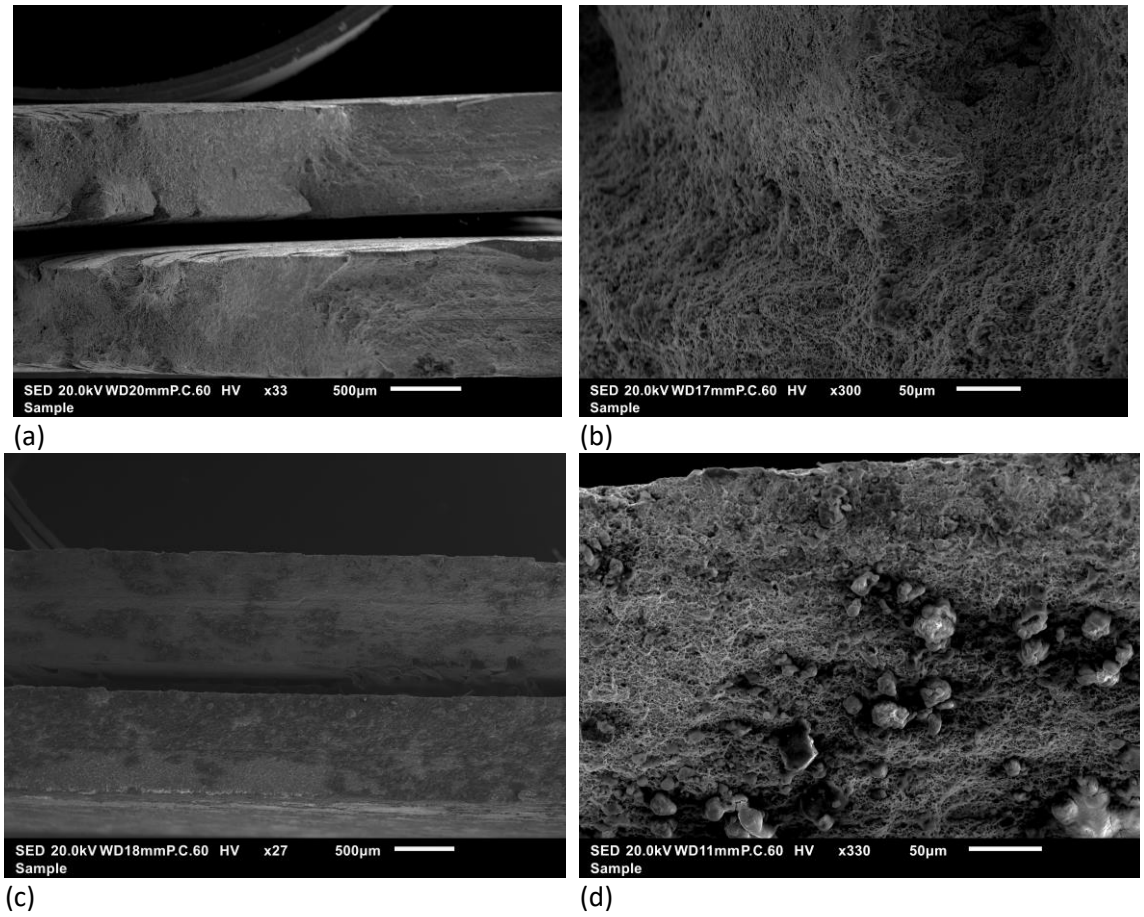

Figure 42 SEM image of fracture surface of a) sample 0.5% pre-strain in -situ a low magnification of an area of the middle section b) a magnified view of previous image c) sample 2% pre-strain in-situ a low magnification of an area of the middle section d) a magnified view of previous image

Fractography images of set B pre-strained in-situ are presented in Figure 41 (a and b). It can be observed that width edge of the sample presents a brittle area around the corner while the inner side seems to remain presenting ductile characteristics such as voids. 2% pre-strain in-situ replicates this pattern as well (Figure 41(c and d)). In Figure 42(a and b) long edges for the plastic 0.5% pre-strain in-situ sample seem to disappear. The middle area is fully ductile. Fractography images of set C1 pre-strained in-situ for the middle area are not clear (Figure 42 (c and d)). In this case, sample is in a worse condition that previous ones. This can be due to possible corrosion and a more severe effect of the TDS. Assumptions are difficult to make, though it seems to resemble previous cases as well.

Effect of pre-strain environment

Images obtained with SEM at different magnifications from samples tested at 2% pre-strain and charged during 60 minutes can be observed in Figure 43 and Figure 44.

Figure 39 (a and b) and Figure 41(a and b) display fractography images of the width edge of 0.5% plastic pre-strained ex-situ and in-situ respectively. As it can be noticed no variation can be seen. Both remain ductile in the center while brittle around the corners. In Figure 40 (a and b)

and Figure 42 (a and b) the middle sections of the samples are shown. Tough, ex-situ pre-strained sample seems to maintain some brittle feature in the long edges, they are not significantly marked. In-situ pre-strained sample lacks brittle characteristics in the middle area. Both methods seem to lead to a similar fracture surface. This confirms that for lower pre-strain and short charging times (15 min) the effect for the environment in mechanical behavior and hydrogen content is minimal.

Figure 39 (c and d) and Figure 41 (c and d) display fractography images of the width edge of 2% plastic pre-strained ex-situ and in-situ respectively. Both pre-train environments seem to lead to the same fracture pattern. Both specimens prevail ductile in the center while brittle around the corners. Regarding the middle area, conclusions are difficult to assess due to the degradation condition of 2% plastic pre-strain sample.

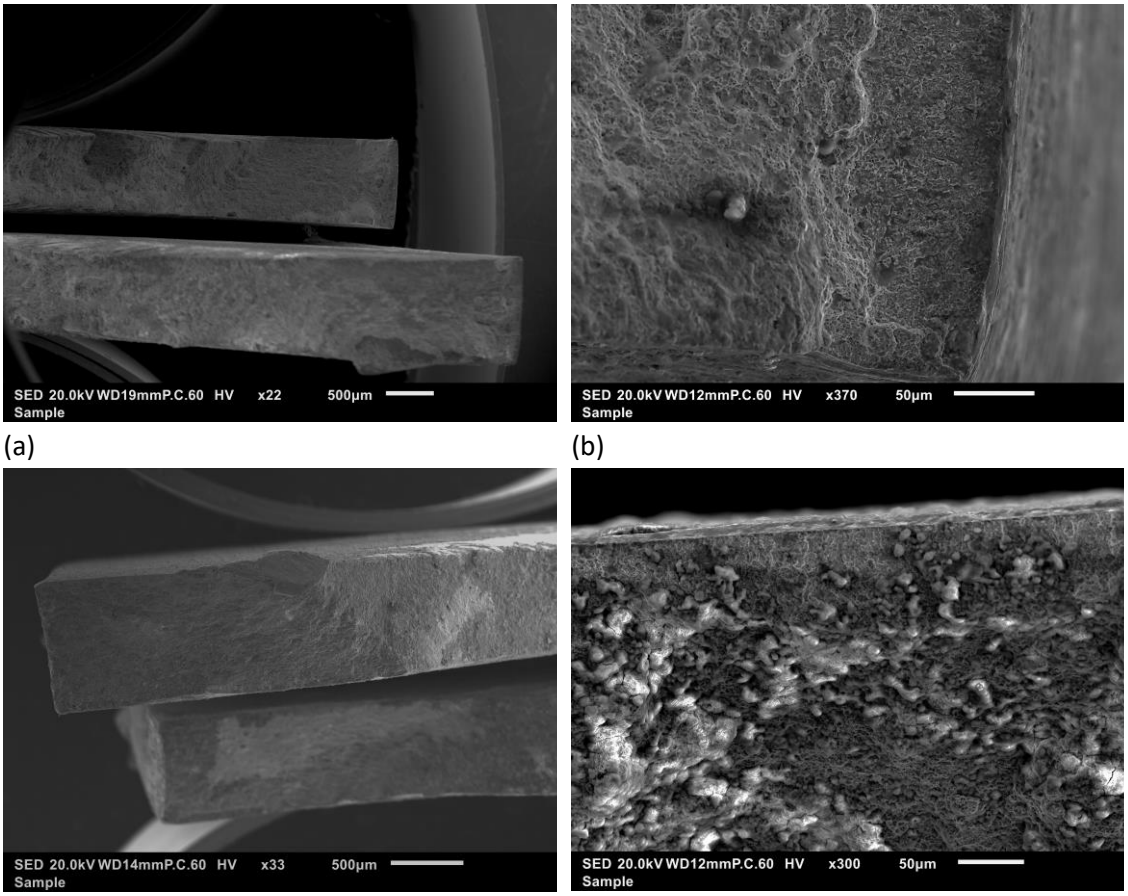

Figure 43 SEM image of fracture surface of a) sample 2% pre-strain ex-situ 60 min at low magnification of the right width edge of the sample b) a magnified view of previous image c) sample 2% pre-strain in-situ 60 min at low magnification of the left width edge of the sample d) a magnified view of previous image

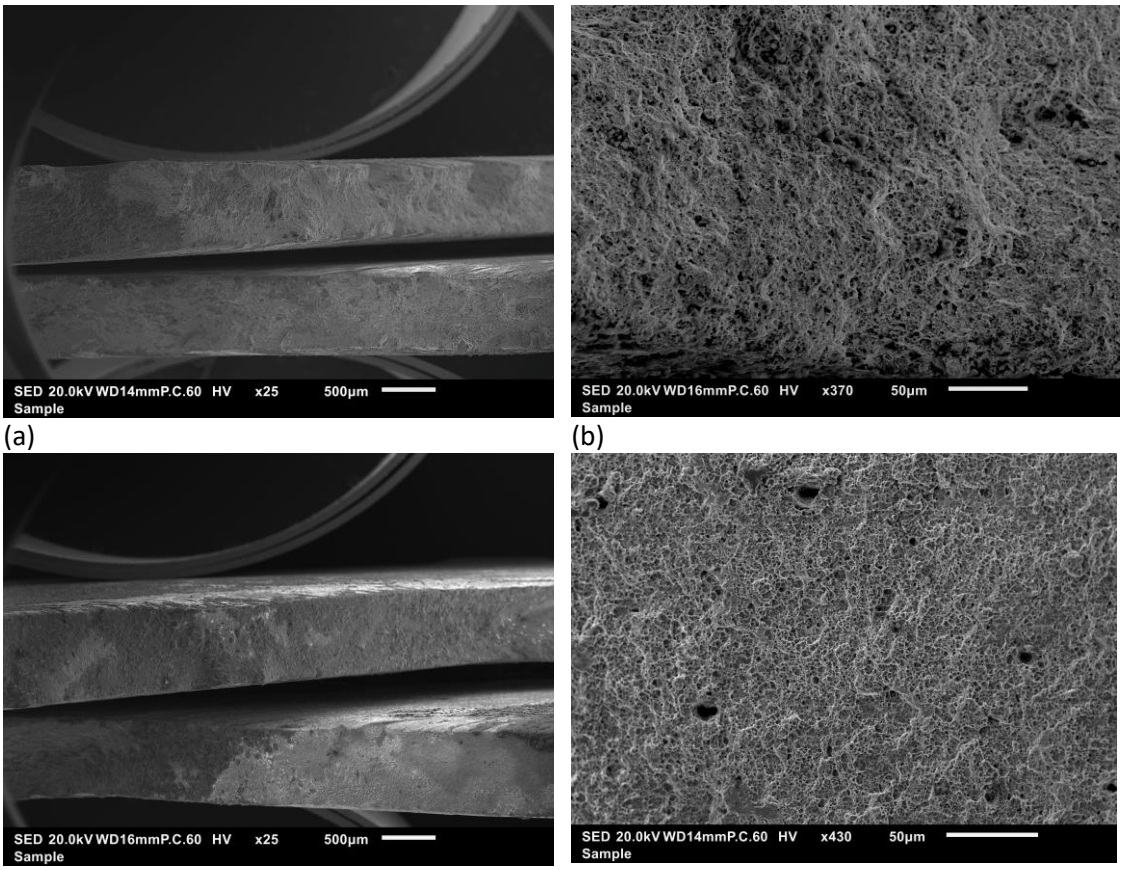

Figure 44 SEM image of fracture surface of a) sample 2% pre-strain ex-situ 60 min at low magnification of the middle section of the sample b) a magnified view of previous image c) sample 2% pre-strain in-situ 60 min at low magnification of the middle section of the sample d) a magnified view of previous image.

In both images (Figure 43 and Figure 44) no significant difference can be observed. Both corners of the samples present a brittle area surrounding them while the inner part displays ductile characteristics such as dimples. In Figure 44 it can be seen that microvoids are present for both pre-straining methods. No brittle length edges are observed. The lack of differences in fractography seem to contradict expectations from the mechanical properties results obtained. Strain to fracture a hydrogen uptake differs for ex-situ and in-situ method. For C2 in-situ a 24% reduction in strain at fracture and an increment of 17% hydrogen uptake was measured. However, the absence of significant difference might be due to the more homogenous hydrogen distribution.

Effect of charging time

Figure 39 (c and d) and Figure 40 (c and d) show set C1 ex-situ fractography. Figure 43 (a and b) and Figure 44 (a and b) display set C2 ex-situ fractography. Images show a clear difference between the samples. Samples of C1, charged for 15 minutes displayed marked long brittle edges while samples of C2 (charged for 60 minutes) don't present this feature. This could be due to the 60 minutes charging time increment compared with the previous 15 minutes charging. Hydrogen is allowed to diffuse through as well as uniformed distribute in the material. In this case, the difference in mechanical properties is translated into visible change in the fracture surface. No severe brittle features are presented.

Due to deteriorate condition of C1 in-situ sample comparison are difficult to stablish with set C2 in-situ sample. However, C2 present o brittle length edges. Fracture seems to be more uniformed due to longer charging time. In addition, voids seem to have reduce its size.

In summary, hydrogen embrittlement is confirmed with fractography as comparing both subsets of A. Moreover, samples present a common fractography with the exception of the sample pre-strained at 2% in situ for 60 minutes. In this regard, samples tend to present brittle features around the edges while remaining ductile in the middle. HE seems not to be more severe for higher amounts of hydrogen, confirming conclusions extracted form analyzing mechanical properties and hydrogen content. Reduction in strain at fracture is small compared to the increase in hydrogen content. Also, the sample pre-strained at 2% in-situ for 60 minutes a seems to support statements from the previous section since higher time, in-situ testing and higher pre-strain seem to lead to a more uniform brittle fracture without the presence of marked brittle edges.

5. CONCLUSIONS

The focus of this work was to observe the effect of the pre-strain and its environment. In particular, to explore the effect pre-strain in-situ since it was one of the main gaps found in the literature research.

In general, results from slow strain rate tensile (SSRT) tests reveal a considerable decrease (>50%) in elongation and hydrogen uptake to 0.4 ppm subsequent to hydrogen charging. Conclusions of this work can be divided into three effects**:**

- **Effect of pre-straining**: plastic pre-strain has an important impact on strain at fracture for DP1000. This has been proven to be true when comparing results of 0% pre-strain in air to 0.5% and 2% plastic pre-strain. Pre-strain reduced the final strain to fracture of the steels by almost 50 % for both in-situ and ex-situ charging cases. This could be due to an increase of reversible hydrogen traps generated due to deformation. Nevertheless, hydrogen embrittlement was not greatly increased after pre-straining to 2% plastic strain instead (9% for in-situ pre-strain), even though the amount of absorbed hydrogen was approximately 0.1 wppm higher in this case. This can be associated with decreasing diffusivity as pre-strain increases, and the short charging times.

- **Effect of pre-straining environment:** The effect of the test environment was not pronounced in most tests. Differences in results among in-situ and ex-situ charging is only visible for higher pre-strain levels and longer charging time (2% pre-strain charged for 60 minutes). An average reduction of 24% in strain at fracture and a 17% ppm increased in hydrogen can be observed for in-situ pre-strain in this group. This could be described by HESIV fracture mechanism. This feedback mechanism enhances the formation of reversable traps due to hydrogen uptake and vice versa. However, no long charging was performed for the 0.5 % pre-strained samples. It becomes clear from the SSRT test (0% pre-strain H), that a high hydrogen content is not required to cause embrittlement.

- **Effect of time:** It becomes clear after then results obtained that the charging time is the main parameter for absorption of hydrogen. Hydrogen content is doubled for 1 h of charging. In contrast, only a small increase is observed from 0.5 to 2 % plastic pre-strain after 15 minutes of charging, However, high amounts of hydrogen do not have any additional effects on the embrittlement of the samples. This points out the importance of the plastic deformation factor.

In addition, some conclusions can be extracted from image obtained of the fracture surface that support previous statements.

- **Fractography**: Hydrogen embrittlement was confirmed through fractography. Samples charged with hydrogen present common fractography features apart from the sample pre-strained at 2% in-situ for 60 minutes. In this regard samples display brittle features around the edges while remaining ductile in the middle area. Hydrogen embrittlement doesn’t

seem to be more severe for high hydrogen content confirming conclusions extracted form analyzing mechanical properties and hydrogen content.

6. RECOMMENDATIONS

This thesis covered a few aspects of the effect of pre-strain and its environment. However, there still some extra experiments and paths for future investigations that should be expanded. Also, some suggestions are given on the procedure:

- Because of time limitations, 0.5% with 60 minutes charging was not possible to test. Therefore, to confirm the effect of charging time over this pre-strained level test should be conducted. In addition, it will be interesting to consider other pre-strain level in the elastic region to observe its effect. Also, extra charging time should be explored to investigate further in-situ and ex-situ effect.

- Further investigation in fractography analysis should be performed. Research regarding fracture embrittlement mechanisms should be conducted.

- Interrupted SSRT are recommended. This could enlighten hydrogen uptake and hydrogen embrittlement mechanisms at different stages and levels of pre-strain.

- Internal factors that play a role in hydrogen embrittlement should be understood. Tests of Dual Phase steels with different microstructures and different ferrite, martensite and retained austenite ratios should be performed. This will help to support statements make in this work and in literature regarding hydrogen diffusivity.

- Regarding procedure and sample preparation, some improvements can be achieved. Diverse difficulties were encountered when trying to insulate samples with glue. This method seems not be fully reliable. In addition, 2h testing was not possible due to glue failure. In case to continue with this method, silicon kit could be used to try to insulate samples glue from the bath. However, changing methodology might result easier. Using close shape grips made of a ceramic material or changing to round specimens as presented in literature might be useful.

- In addition, notches can also be present a new path to investigate together with different levels of pre-strain and environment.

BIBLIOGRAPHY

[1] [En línea]. Available: https://www.statista.com/statistics/276629/global-co2-emissions/.

[2] G. P. Chirinda y S. Matope, «The Lighter the Better: Weight Reduction in the Automotive Industry and its Impact on Fuel Consumption and Climate Change,» de *Proceedings of the 2nd African International Conference on Industrial Engineering and Operations Management* , Zimbabwe, 2020.

[3] J. Galán, L. Samek, P. Verleysen, K. Verbeken y Y. Houbaert, «Advanced high strength steels for automotive industry,» *Revista De Metalurgia,* vol. 48, nº 2, pp. 118-131, 2012.

[4] A. Cabrera Serrenho, J. B. Norman y J. M. Allwood, «The impact of reducing car weight on global emissions: the future fleet in Great Britain,» *Philosophical Transactions Royal Society,* vol. 375, 2017.

[5] J. Zhao y Z. Jiang, «Thermomechanical processing of advanced high strength steels,» *Progress in Materials Science,* vol. 94, pp. 174-242, 2018.

[6] W. Zhang y J. Xu, «Advanced lightweight materials for Automobiles: A review,» *Materials & Design,* vol. 221, 2022.

[7] Q. Gao, «Investigations on Hydrogen Embrittlement of Advanced High Strength Steels for Automotive Applications,» 2017.

[8] T. Boot, «Review and Discussion of the literature regarding Hydrogen Embrittlement and its mechanisms in ferritic AHSS,» 2021.

[9] S. K. Dwivedi y M. Vishwakarma, «Effect of hydrogen in advanced high strength steel materials,» *International Journal of Hydrogen Energy,* vol. 44, pp. 28007-28030, 2019.

[10] W. H. Johnson, «On some remarkable changes produced in iron and steel by the action,» *The Royal London Society,* 1875.

[11] A. Khare, M. Vishwakarma y V. Parashar, «A Review on Failures of Industrial Components due to Hydrogen Embrittlement & Techniques for Damage Prevention,» *International Journal of Applied Engineering Research,* vol. 12, nº 8, pp. 1784-1792, 2017.

[12] Q. S. Allen y T. W. Nelson, «Microstructural evaluation of hydrogen embrittlement and successive recovery in advanced high strength steel,» *Journal of Materials Processing Tech. ,* vol. 265, p. 12–19, 2019.

[13] D. Rudomilova, T. Prošek y G. Luckeneder, «Techniques for investigation of hydrogen embrittlement of advanced high strength steels,» *Corrosion Reviews,* vol. 36, nº 5, p. 413–434, 2018.

[14] G. Lovicu, M. Botazzi , F. D'Aiuto, M. De Sanctis, A. Dematteo, C. Santus y R. Valentini, «Hydrogen Embrittlement of Automotive Advanced High-Strength Steels,» *Metallurgial and Materials Transactions,* vol. 43A, 2012.

[15] M. Truschner, A. Trautmann y G. Mori, «The Basics of Hydrogen Uptake in Iron and Steel,» *Berg Huettenmaenn Monatsh,* vol. 116, nº 9, p. 443–449, 2021.

[16] A. Turnbull, «Hydrogen diffusion and trapping in metals,» de *Gaseous Hydrogen Embrittlement of Materials in Energy Technologies*, Woodhead Publishing, 2010, pp. 89-128.

[17] G. K. Padhy y Y.-i. Komizo, «Diffusible Hydrogen in Steel Weldments,» *Transactions of Joining and Welding Research Institute,* vol. 42, nº 1, pp. 39-62, 2013.

[18] S. Lynch, «Hydrogen embrittlement (HE) phenomena and mechanisms,» *Corrosion Reviews,* vol. 30, nº 3, 2012.

[19] I. Uribe Pérez, A. B. Velosa Pacheco y L. E. Zabala Capacho, «Fundamentos del daño por hidrógeno en los aceros,» *El Hombre y la Máquina,* nº 36, pp. 123-142, 2011.

[20] O. Barrera, D. Bombac, Y. Chen, T. D. Daff, G.-N. E., G. P., H. D., H. R., K. I., J. R. Kermode, L. C., S. M. y S. F., «Understanding and mitigating hydrogen embrittlement of steels: a review of experimental, modelling and design progress from atomistic to continuum,» *Journal of Materials Science,* 2018.

[21] M. L. Martin, M. Dadfarnia, A. Nagao, S. Wang y P. Sofronis, «Enumeration of the hydrogen-enhanced localized plasticity mechanism for hydrogen embrittlement in structural materials,» *Acta Materialia,* vol. 165, pp. 734-750, 2019.

[22] M. Nagumo y K. Takai, «The predominant role of strain-induced vacancies in hydrogen embrittlement of steels: Overview,» *Acta Materialia,* vol. 165, pp. 722-733, 2019.

[23] L. Vecchi, D. Pecko, N. Van den Steen, M. Haile Mamme, B. Ozdirik, D. Van Laethem, Y. Van Ingelgem, J. Deconinck y H. Terryn, «A modelling approach on the impact of an oxide layer on the hydrogen permeation through iron membranes in the Devanathan-Stachurski cell,» *Electrochimica Acta,* vol. 286, pp. 139-147, 2018.

[24] S. Evers, C. Senoz y M. Rohwerder, «Hydrogen detection in metals: a review and introduction of a Kelvin probe approach,» *Science and Technology of,* vol. 14, 2013.

[25] D. Mallick, «Hydrogen Behavior in First and Second Generation of Advanced High Strength Steels,» Université de Lyon; Indian institute of technology, 2020.

[26] S. Ogura y K. Fukutani, «Thermal Desorption Spectroscopy,» de *Compendium of Surface and Interface Analysis*, Springer, 2018.

[27] F. von Zeppelin, M. Haluška, y M. Hirscher, «Thermal desorption spectroscopy as a quantitative tool to determine the hydrogen content in solids,» *Thermochimica Acta,* vol. 404, p. 251–258, 2003.

[28] «ASTM G129: Standard Practice for Slow Strain Rate Testing to Evaluate the Susceptibility of Metallic Materials to Environmentally Assisted Cracking,» *American Society for Testing and Materials (ASTM),* 2000.

[29] T. Chida, Y. Hagihira, E. Akiyama, K. Iwanaga, S. Takagi, M. Hayakawa, H. Ohisi, D. Hirakami y T. Tarui, «Comparison of Constant Load, SSRT and CSRT Methods for Hydrogen Embrittlement

Evaluation Using Round Bar Specimens of High Strength Steels,» *ISIJ International,* vol. 56, nº 7, p. 1268–1275, 2016.

[30] E. Martínez-Pañeda, Z. D. Harris, S. Fuentes-Alonso, J. R. Scully y J. T. Burns, «On the suitability of slow strain rate tensile testing for assessing hydrogen embrittlement susceptibility,» *Corrosion Science,* vol. 163, 2020.

[31] R. Scharf, A. Muhr, G. Luckeneder, P. Larour, K. Mraczek, J. Rehrl, F. Leomann, K.-H. Stellnberger, J. Faderl y G. Mori, «Hydrogen embrittlement of DP-1000 flat steel sheet: Influence of mechanical properties, specimen geometry,pre-damaging and electrolytically zinc galvanizing,» *Materials and Corrosion,* nº 3, pp. 239-250, 2016.

[32] «G142 − 98: Standard Test Method for Determination of Susceptibility of Metals to Embrittlement in Hydrogen Containing Environments at High Pressure, High Temperature, or Both,» *American Society for Testing and Materials (ASTM),* 2016.

[33] «ASTM F1624 − 12: Standard Test Method for Measurement of Hydrogen Embrittlement Threshold in Steel by the Incremental Step Loading Technique,» *American Society for Testing and Materials ,* 2018.

[34] S. Takagi, S. Terasaki, K. Tsuzaki, T. Inoue y F. Minami, «A New Evaluation Method of Hydrogen Embrittlement Fracture for High Stregth Steel by Local Approach,» *ISIJ International,* vol. 45, nº 2, pp. 263-271, 2005.

[35] M. L. Martin, . J. A. Fenske, G. S. Liu, P. Sofronis y . I. M. Robertson, «On the formation and nature of quasi-cleavage fracture surfaces in hydrogen embrittled steels,» *Acta Materiali,* vol. 59, pp. 1601-1606, 2011.

[36] L. Cho, . P. Bradley, D. Lauria, M. Martin, M. Connolly, J. Benzing, E. Seo, K. Findley, J. Speer y A. Slifka, «Characteristics and mechanisms of hydrogen-induced quasi-cleavage fracture of lath martensitic steel,» *Acta Materialia,* vol. 203, 2021.

[37] Z. Wang, J. Liu, F. Huang, Y.-j. Bi y S.-q. Zhang, «Hydrogen Diffusion and Its Effect on Hydrogen Embrittlement in DP Steels With Different Martensite Content,» *Frontiers in Materials,* vol. 7, 2020.

[38] T. Depover, . E. Wallaert y . K. Verbeken, «Fractographic analysis of the role of hydrogen diffusion on the hydrogen embrittlement susceptibility of DP steel,» *Materials Science & Engineering A,* vol. 649, pp. 201-208, 2016.

[39] J. Rehrl, K. Mraczek, A. Pichler y E. Werner, «Mechanical properties and fracture behavior of hydrogen charged AHSS/UHSS grades at high- and low strain rate tests,» *Materials Science & Engineering A,* vol. 590, pp. 360-367, 2014.

[40] T. Depover, F. Vercruysse, A. Elmahdy, P. Verleysen y K. Verbeken, «Evaluation of the hydrogen embrittlement susceptibility in DP steel under static and dynamic tensile conditions,» *International Journal of Impact Engineering,* vol. 123, pp. 118-125, 2019.

[41] T. Kumamoto, M. Koyama, K. Sato y K. Tsuzaki, «Strain-rate sensitivity of hydrogen-assisted damage evolution and failure in dual-phase steel: From vacancy to micrometer-scale void growth,» *Engineering Fracture Mechanics,* vol. 215, 2019.

[42] Y. Matsumoto, T. Miyashita y K. Takai, «Hydrogen behavior in high strength steels during various stress applications corresponding to different hydrogen embrittlement testing methods,» *Materials Science & Engineering A,* vol. 735, pp. 61-72, 2018.

[43] K. S. Reddy, Y. Govindaraj y L. Neelakantan, «Hydrogen diffusion kinetics in dual-phase (DP 980) steel: The role of pre-strain and tensile stress,» *Electrochimica Acta,* vol. 439, 2023.

[44] A. Drexler, J. Domitner y C. Sommitsch, «Modeling of Hydrogen Diffusion in Slow Strain Rate (SSR) Testing of Notched Samples,» de *Advances in Hydrogen Embrittlement Study*, Springer, 2021, pp. 87-111.

[45] J. Venezuela, T. Hill, Q. Zhou, H. Li, Z. Shi, F. Dong, R. Knibbe, M. Zhang, M. S. Dargusch y A. Atrens, «Hydrogen-induced fast fracture in notched 1500 and 1700 MPa class automotive martensitic advanced high-strength steel,» *Corrosion Science,* vol. 188, 2021.

[46] M. Wang, E. Akiyama y K. Tsuzaki, «Effect of hydrogen and stress concentration on the notch tensile strength of AISI 4135 steel,» *Materials Science and Engineering,* vol. 398, 2005.

[47] D. Hardie y S. Liu, «The Effect of Strea Concentration on Hydrogen Embrittlement of a Low Alloy Steel,» *Corrosion Science,* vol. 38, nº 5, pp. 721-733,, 1996.

[48] T. Depover, S. Hertelé y K. Verbeken, «The effect of hydrostatic stress on the hydrogen induced mechanical degradation of dual phase steel: A combinedexperimental and numerical approach,» *Engineering Fracture Mechanics,* vol. 221, 2019.

[49] A. Drexler, B. Helic, Z. Silvayeh, C. Sommitsch, K. Mraczek y J. Domitner, «Influence of Plastic Deformation on the Hydrogen Embrittlement Susceptibility of Dual Phase Steels,» *Trans Tech Publications,* vol. 926, pp. 2077-2091, 2022.

[50] K. Hye-Jin y L. Myoung-Gyu, «Analysis of hydrogen trapping behaviour in plastically deformed quenching and partitioning steel in relation to microstructure evolution by phase transformation,» *Journal of Alloys and Compound,* vol. 904, 2022.

[51] . L. Weiguo, W. Weijie, Z. Qingjun, L. Wenyao y L. Jinxu, «Analysis of hydrogen-induced delayed cracking and hydrogen trapping behavior in plastically deformed quenching and partitioning steel,» *Corrosion Science,* vol. 223, 2023.

[52] A. Zafra, L. Peral, J. Belzunce y C. Rodríguez, «Effects of hydrogen on the fracture toughness of 42CrMo4 steel quenched and tempered at different temperatures,» *International Journal of Pressure Vessels and Piping,* vol. 171, pp. 34-50, 2019.

[53] T. Ping, Y. Fei, . C. Weiwei, J. Zhao, Y. Wang y J. Gong, «Analysis of enhanced hydrogen embrittlement fracture for pre-strain hardening 2205 duplex stainless steel,» *Results in Physics,* vol. 16, 2020.

APPENDIX A: sample preparation details

This section compiles a summary of the different attempts in sample preparation until reaching the final version.

The first version consisted of a 3D printed mold made of PEEK. The sample and shape were indented in the mold. Samples were mounted and glued with ES 579 epoxy glue. Specimens were placed in the oven at 150 ºC for one hour for the glue to cure. Teflon was sprayed over the mold to avoid samples sticking to it. Specimens were aligned through the pin holes with two cylindrical 3D printed pieces. This method resulted in non-consistent amounts of glue as well as presenting misalignment.

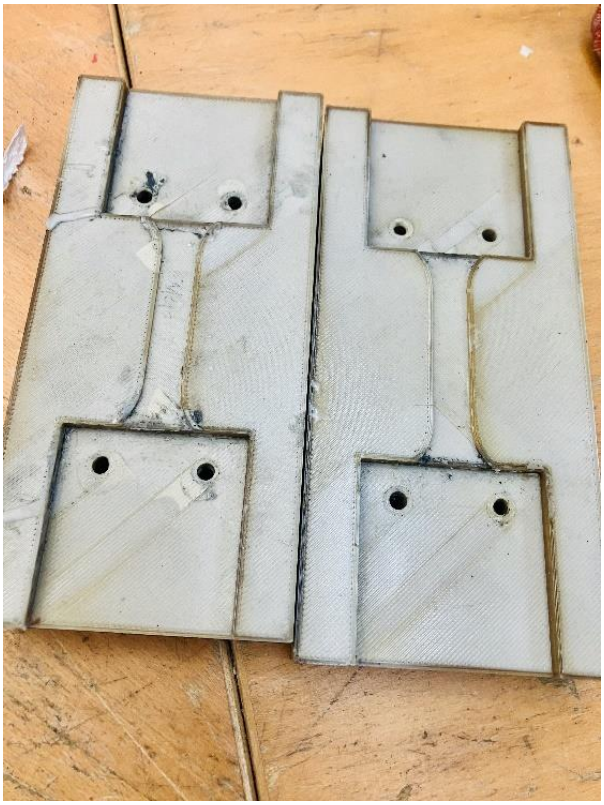

Figure A. 1 PEEK Mould.

A variation of this method, that used 3D printed spacers of 1.5mm to try to correct for the amount of glue used also resulted to be fruitless. The misalignment was still not corrected, and the inconsistent results persisted while destroying the mold and spacers. Another attempt was made using only half of the mold and adding two bolts to the metal plates to hold the samples. Misalignment endured.

The first successful version was a like the first method. This variation consisted of a mold made of Teflon supported with two steel parts in the outside. The specimen geometry was indented in the Teflon, this time both parts were fixed by bolts to ensure that no displacement occurred inside the oven. Spacers were used to ensure that the slaps remain parallel to each other. Nevertheless, this method was unable to hold the stress while submerged in the solution. A correction with clamps failed to solve the problem as well. Therefore, samples were modified to their final length to increase the area of glue application. It was also realized that a possible misfit between the slabs

might be translated into a non-correct distribution of the load while testing (only one of the slabs holding the load).

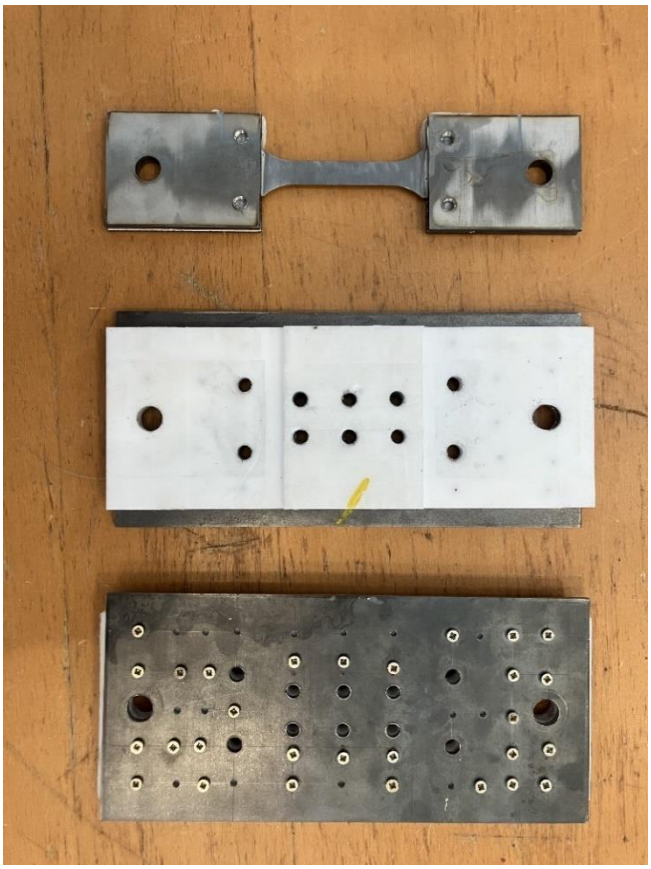

Figure A. 2 Teflon mould failed sample preparation method.

APPENDIX B: Tensile Test curves

Engineering Stress -Strain curves for the results obtained are displayed in this section.

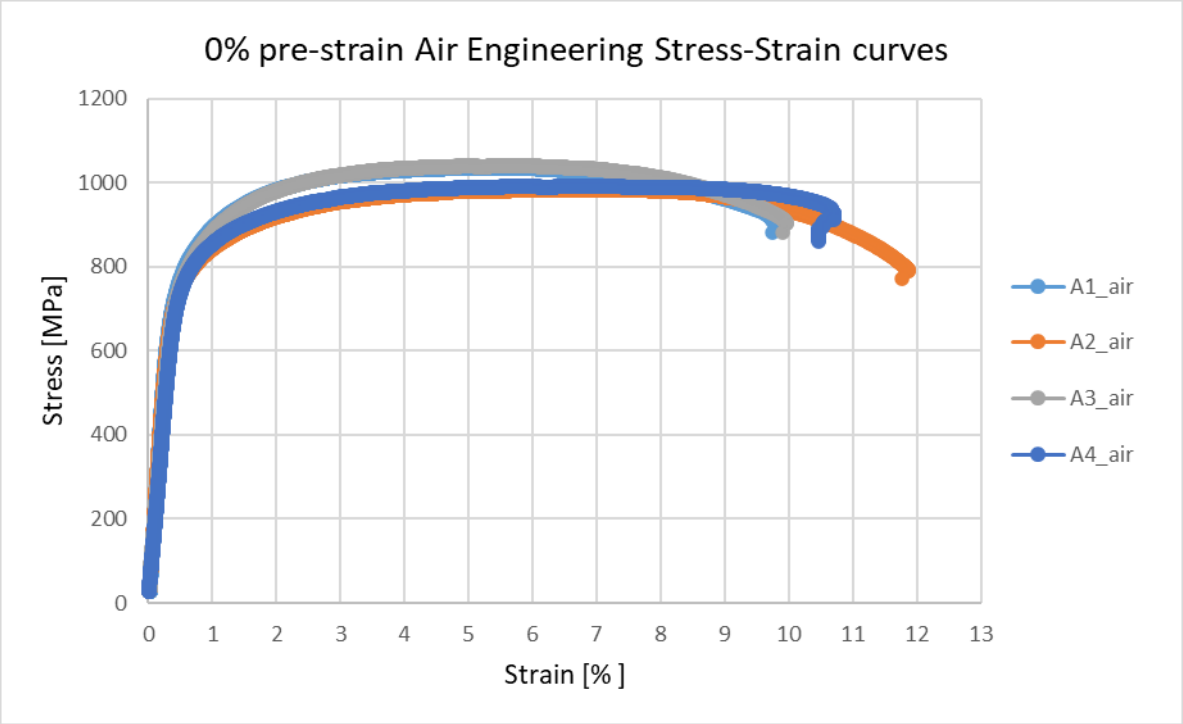

Figure B. 1 Engineering Stress- Strain curve for set A in air.

Table B. 1 Overview strain at failure for set A in air.

	A1_air	A2_air	A3_air	A4_air
% strain at failure	9.76	11.76	9.90	10.46
Average	10.5 ± 0.8			

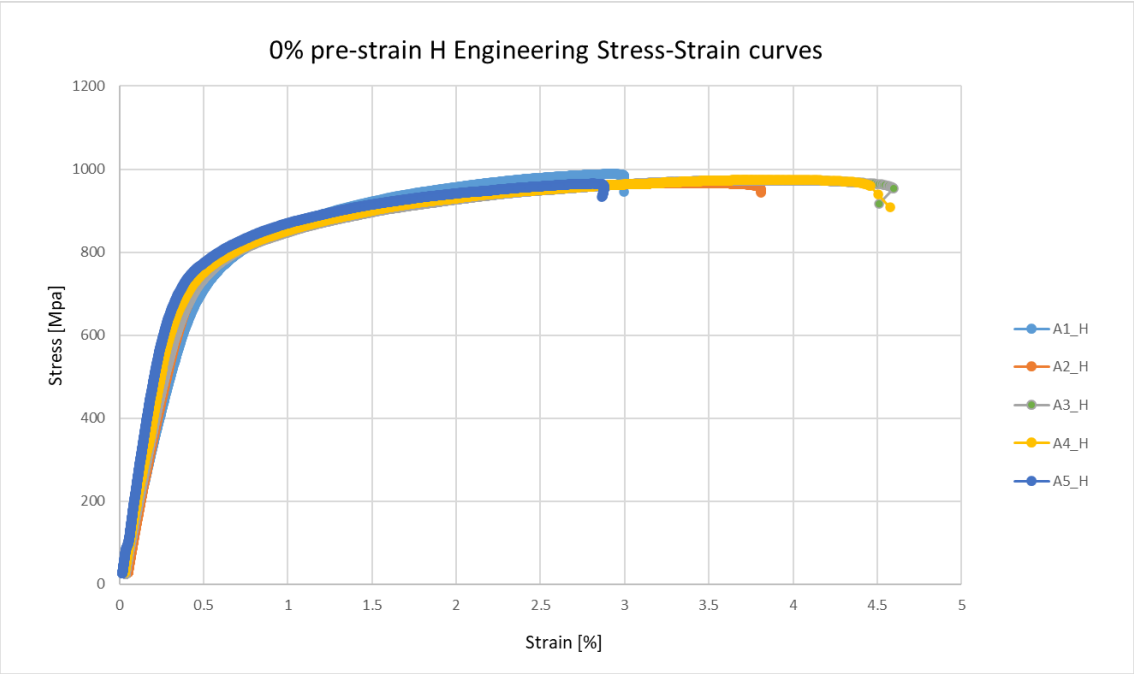

Figure B. 2 Engineering Stress- Strain curve for set A in H

Table B. 2 Overview strain at failure for set A in H

	A1_H	A2_H	A3_H	A4_H	A5_H
% strain at failure	3.0	3.4	4.5	7.3	2.9
Average	4.6 ± 1.9				

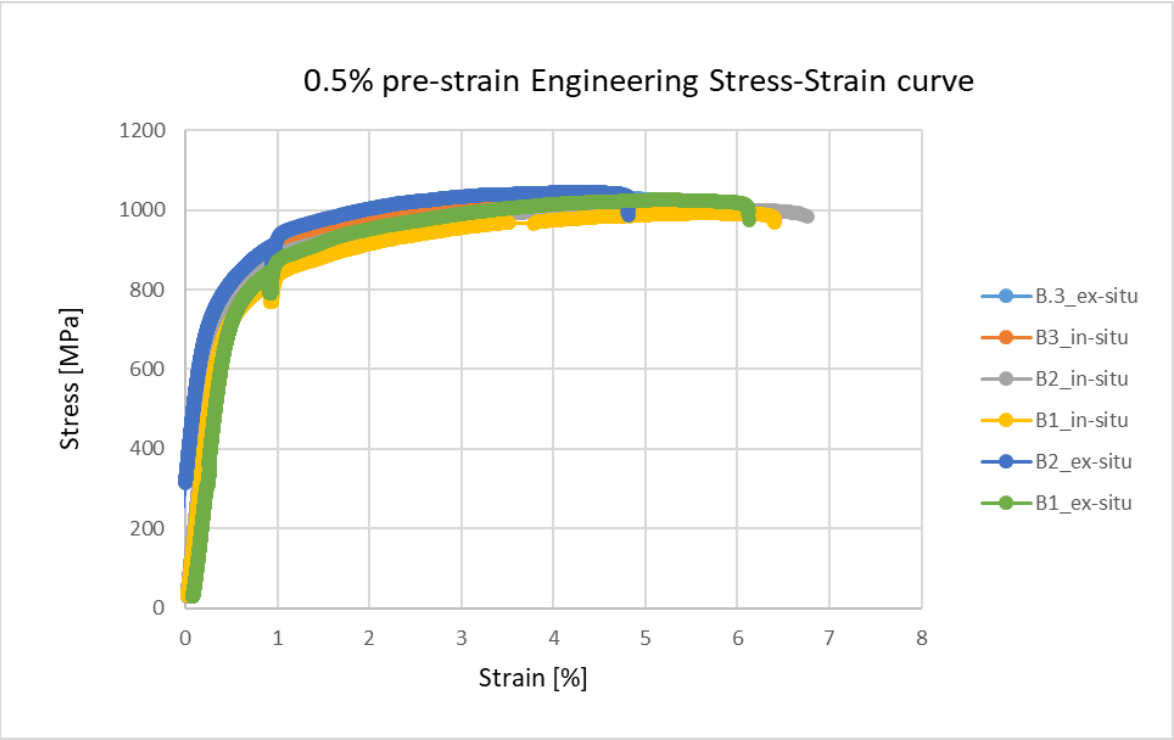

Figure B. 3 Engineering Stress- Strain curve for set B.

Table B. 3 Overview strain at failure for set B.

	In-situ			Ex-situ		
	B1_in-situ	B2_in-situ	B3_in-situ	B1_ex-situ	B2_ex-situ	B3_ex-situ
% strain at failure	6.4	6.7	4.6	6.1	4.8	5.5
Average	5.9 ± 1.1			5.5 ± 0.6		

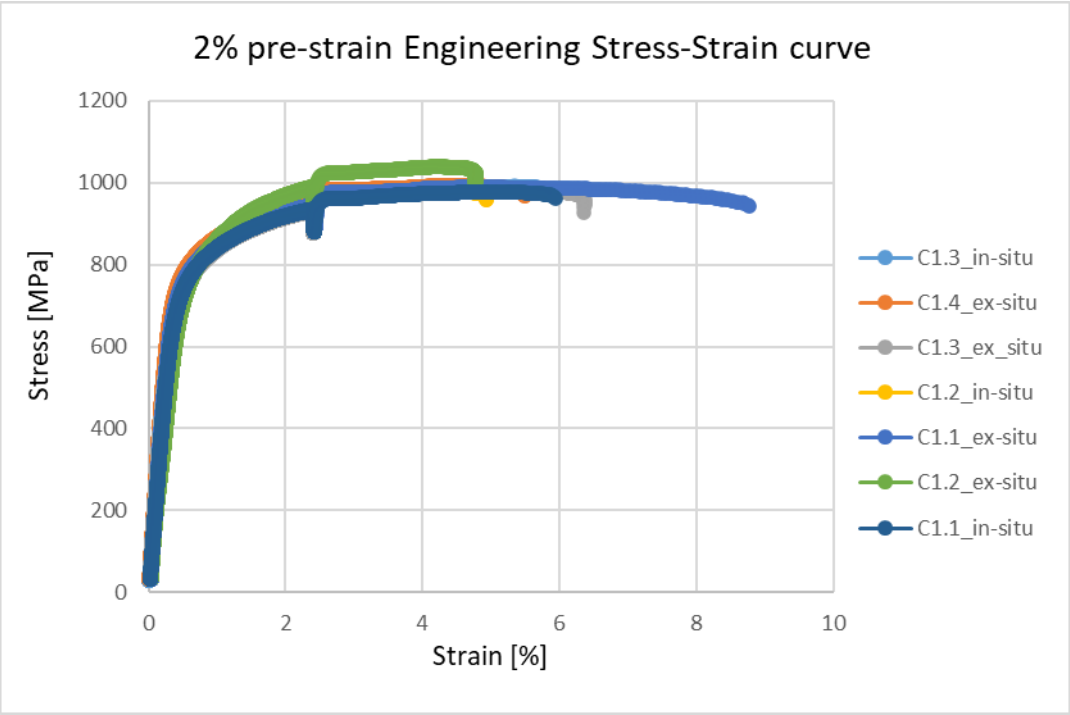

Figure B. 4 Engineering Stress- Strain curve for set C1.

Table B. 4 Overview strain at failure for set C1.

	In-situ			Ex-situ			
	C1.1_in-situ	C1.2_in-situ	C1.3_in-situ	C1.1_ex-situ	C1.2_ex-situ	C1.3_ex-situ	C1.4_ex-situ
% strain at failure	5.9	4.9	5.3	8.8	4.8	5.5	5.47
Average	5.4 ± 0.5			6.3 ± 1.8			

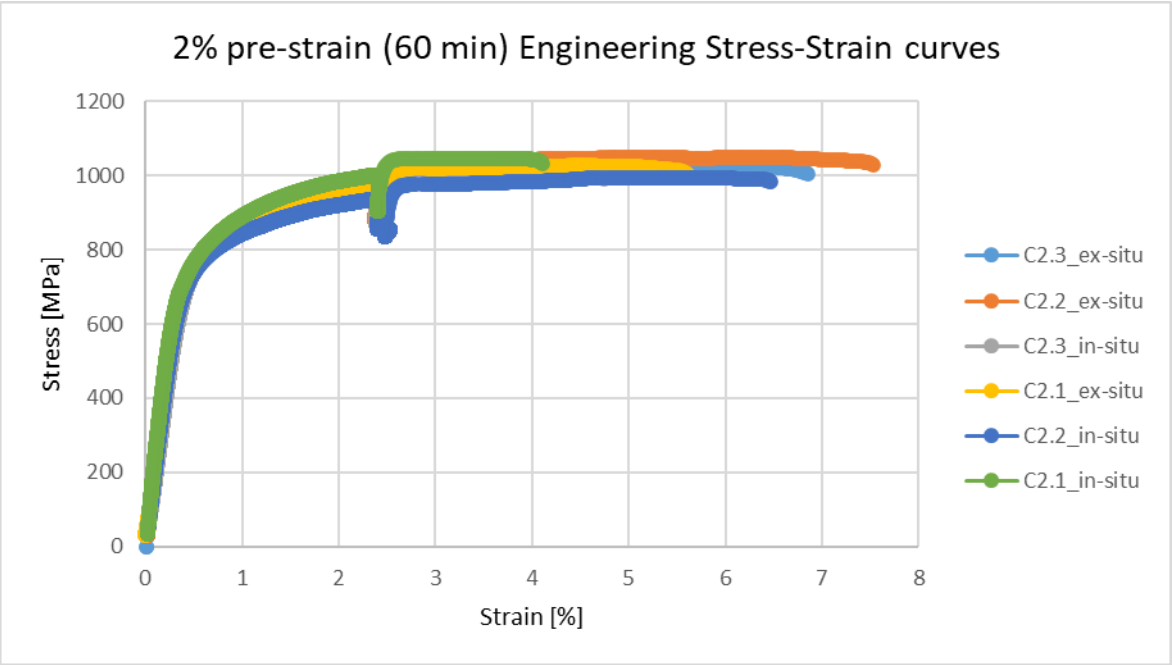

Figure B. 5 Engineering Stress- Strain curve for set C2.

Table B. 5 Overview strain at failure for set C2.

	In-situ			Ex-situ		
	C2.1_in-situ	C2.2_in-situ	C1.3_in-situ	C2.1_ex-situ	C2.2_ex-situ	C2.3_ex-situ
% strain at failure	4.1	6.5	4.8	5.6	7.5	6.9
Average	5.1 ± 1.2			6.7 ± 1.0		